Modelling of Antenna Responses

by

Ngoy Mutonkole

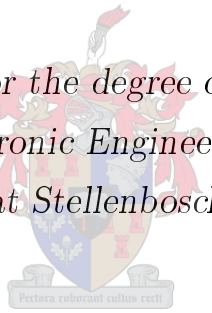

Dissertation presented for the degree of Doctor of Philosophy in Electrical and Electronic Engineering in the Faculty of Engineering at Stellenbosch University

Promoter: Prof. Dirk I.L. de Villiers

December 2016

Declaration

By submitting this dissertation electronically, I declare that the entirety of the work contained therein is my own, original work, that I am the sole author thereof (save to the extent explicitly otherwise stated), that reproduction and publication thereof by Stellenbosch University will not infringe any third party rights and that I have not previously in its entirety or in part submitted it for obtaining any qualification.

Date: December 2016 .....

Abstract

Modelling of Antenna Responses

N. Mutonkole

Dissertation: Ph.D. (EE)

December 2016

This dissertation presents surrogate modelling techniques for the radiation patterns and scattering parameters of antennas. The models are developed in the context of calibration of reflector antennas as well as antenna design activities such as design space exploration, optimisation and sensitivity analysis.

On the calibration front, a method is proposed to recover the radiation pattern, resulting from some physical deformation of an offset Gregorian reflector antenna, over a wide frequency bandwidth by taking a few directional measurements at a single frequency. The proposed technique combines characteristic basis function patterns (CBFPs) with the linear algebraic notion of subspace projection and is shown to achieve pattern recovery with better than -40 dB accuracy over a bandwidth of up to a decade.

Concerning surrogate models for antenna design, models based on the parametrisation of CBFPs are presented at three levels: (i) CBFPs are parametrised on a fixed grid of EM simulated samples to yield multivariate models of the full radiation pattern. The associated S-parameters are modelled through an indirect parametrisation of the poles and residues obtained by fitting S-parameter data with rational functions. (ii) A univariate adaptive sampling algorithm is devised to model the frequency dependence of the full radiation pattern by judiciously selecting the frequency samples at which the antenna is simulated. The proposed algorithm is guaranteed to converge to an accurate model in a modest number of iterations, thereby improving the efficiency of frequency domain antenna simulations. (iii) A multivariate adaptive sampling algorithm is devised to model the full radiation pattern as well as S-parameters as a function of multiple design variables (including frequency). The proposed adaptive sampling techniques have the additional feature of approximation error control.

The proposed surrogate modelling techniques can be used to improve the calibration efficiency of reflector antennas (since fewer measurements are required for wideband systems), as well as to improve the design work flow of antennas by reducing the computational cost of the associated design activities.

Opsomming

Modellering van Antenna Gedrag

N. Mutonkole

Proefskrif: Ph.D. (EE)

Desember 2016

Hierdie proefskrif stel surrogaat modelleringstegnieke voor vir die stralingspatrone en strooiparameters van antennas. Die modelle is ontwikkel binne die konteks van kalibrasie van weerkaatsantennas, sowel as antenna ontwerp aktiwiteite soos ontwerp-ruimte verkenning, optimering, en sensitiwiteitsanalise.

Vir die kalibrasie is 'n metode voorgestel wat die stralingspatroon verkry, as gevolg van 'n fisiese vervorming van 'n afset Gregoriaanse weerkaatsantenna, oor 'n wye frekwensie bandwydte deur slegs 'n paar direksionele metings te neem by 'n enkele frekwensie. Die voorgestelde tegniek kombineer karakteristieke basisfunksie-patrone (KBFP's) met die idee van subspasie projeksie uit lineêre algebra, en toon patroon herwinning van beter as -40 dB akkuraatheid oor tot 'n dekade bandwydte.

Met betrekking tot surrogaat modelle vir antenna ontwerp word daar modelle wat gebaseer is op die parameterisering van KBFP's voorgestel op drie vlakke: (i) KBFP's word geparameteriseer op 'n vaste rooster van EM-gesimuleerde monsters om multi-veranderlike modelle van die volledige stralingspatroon te kry. Die geassosieerde S-parameters word gemodelleer deur 'n indirekte parameterisering van die pole en residue wat deur die passing van rasionale funksies op S-parameters verkry is. (ii) 'n Enkel-veranderlike aanpasbare monsteringsalgoritme is voorgestel om die frekwensie-afhanklikheid van die volledige stralingspatroon te modelleer, deur oordeelkundig frekwensie-punte te kies waar die antenna gesimuleer moet word. Die voorgestelde algoritme is gewaarborg om te konvergeer na 'n akkurate model binne 'n beskeie aantal iterasies, wat die effektiwiteit van frekwensie-gebied antenna simulasies verbeter. (iii) 'n Multi-veranderlike aanpasbare monsteringsalgoritme is voorgestel om die volledige stralingspatroon, sowel te modelleer as die S-parameters, as 'n funksie van veelvoudige ontwerpveranderlikes (insluitend frekwensie). Die voorgestelde aanpasbare monsteringstegnieke kan ook die benaderingsfout beheer.

Die voorgestelde surrogaat modelleringstegnieke kan gebruik word om die kalibrasie effektiwiteit van weerkaatsantennas te verbeter (aangesien minder metings nodig is vir wyeband stelsels), sowel as om die ontwerp werkswyse vir antennas te verbeter deur die rekenaar berekeningskoste van die geassosieerde ontwerp aktiwiteite te verminder.

Acknowledgements

I am deeply indebted to my adviser, Prof. Dirk de Villiers, for his generosity and tremendous support during the course of my post-graduate studies. I thank Dirk for expertly guiding me through the different topics of this dissertation, for seeing value in my ideas (even when I doubted them at times) and most of all for asking all the thought provoking questions. I also thank my adviser for going out of his way to make it possible for me to travel, meet other researchers and expand my horizon. Sir, being your student has been a huge honour and privilege.

I wish to thank Prof. Tom Dhaene (Ghent University, Belgium) for making my visit to the SUMO Lab possible, and for his support throughout the duration of the visit and thereafter – Many thanks for the opportunity. Thanks to Dr. Dirk Deschrijver and Dr. Elizabeth Rita Samuel for their help while in Gent. I thank Elizabeth for her kindness and for teaching me much more than I could have hoped to learn in one week. I thank Prof. Francesco Ferranti (Vrije Universiteit Brussel, Belgium) for the visit in Brussels and for sharing his problem solving wisdom with me.

Thanks to my colleagues in the penthouse, past and present, for the generally good working environment. In particular, I thank Dr. André Young for very quickly teaching me the CBFP method as well as some fundamentals of numerical linear algebra, Anathi Hokwana and TJ Phiri for the entertaining discussions on all sorts of topics.

Thanks to SKA South Africa and the NRF for funding my Ph.D. experience through the SARChI program. A word of gratitude to Prof. David Davidson for supporting various applications to fund my postgraduate studies.

My utmost gratitude goes to my family for continuously shaping, educating and supporting me in all my endeavours. They are and always will be a very bright reference in my life. My elder brother is credited for teaching me about life and how to live. *Mwafwaiko bikatampe!*

To Nabila Hatimy, I am grateful for the amazing social life you allowed me to have, for the many other things that you taught me and for your unfailing support whether we were physically together or on different continents!

To God be all the glory!

Dedications

To my mother, the rock upon which my life is built.

Contents

List of Figures

List of Tables

List of Publications

The work presented in this dissertation is based on the following publications:

Journal Publications

1. N. Mutonkole, E.R. Samuel, D.I.L. de Villiers and T. Dhaene, "Parametric Modeling of Radiation Patterns and Scattering Parameters of Antennas," *IEEE Trans. Antennas Propag.*, vol. 64, no. 3, pp. 1023–1031, Mar. 2016.

2. N. Mutonkole and D.I.L. de Villiers, "Multivariate Adaptive Sampling of Parameterized Antenna Responses," submitted to *IEEE Trans. Antennas Propag.*, 2016.

Conference Publications

1. N. Mutonkole and D.I.L. de Villiers, "Adaptive Frequency Sampling for Radiation Patterns and S-parameters of Antennas", submitted to the 11^{th} *European Conf. on Antennas Propag.* (EuCAP), Paris, France, April 2017, pp. 1–5.

2. N. Mutonkole and D.I.L. de Villiers, "An Adaptive Sampling Algorithm for the Efficient Prediction of Antenna Radiation Patterns Over a Wide Frequency Bandwidth", in Proc. 10^{th} *European Conf. on Antennas Propag.* (EuCAP), Davos, Switzerland, April 2016, pp. 1–5.

3. N. Mutonkole and D.I.L. de Villiers, "Characteristic Basis Function Patterns Method for Reflector Antenna Calibration: An Extension to Multiple Frequencies," in Proc. 9^{th} *European Conf. on Antennas Propag.* (EuCAP), Lisbon, Portugal, April 2015, pp. 1–5.

Nomenclature

AFS	Adaptive Frequency Sampling
CBFP	Characteristic Basis Function Pattern
CEM	Computational Electromagnetic
EM	Electromagnetic
FDTD	Finite Difference Time Domain
LHS	Latin Hypercube Sampling
MAS	Multivariate Adaptive Sampling
MBPE	Model Based Parameter Estimation
MoM	Method of Moments
PO	Physical Optics
RMS	Root Mean Square
RRMSE	Relative Root Mean Square Error
SKA	Square Kilometre Array
SVD	Singular Value Decomposition
VF	Vector Fitting

Chapter 1

Introduction

In this dissertation, we describe a set of algorithms to model and characterise antenna responses, i.e., the radiation pattern up to a full sphere as well as the associated scattering parameters where appropriate. The proposed models are to be used in two contexts:

1. **Calibration:** herein, the intended application is the calibration of reflector antennas for direction dependent effects in the context of next-generation radio telescopes such as MeerKAT [1] and the square kilometre array (SKA) [2] . One of the most crucial steps in calibration of next generation radio telescopes requires the knowledge of the radiation pattern over a wide angular region as well as a wide frequency bandwidth.

2. **Antenna design:** in this part, we aim to develop efficient surrogate models of the antenna's full radiation patterns as well as S-parameters. The models are parametrised with respect to design variables (e.g., geometry, frequency). Such models are then intended to be used within the efficient design paradigm of surrogate based modelling and optimisation where the emphasis is on obtaining better designs at a reduced computational cost when compared to traditional methods.

By leveraging techniques from disparate areas of linear algebra, system identification and electromagnetic theory, several algorithms are devised to address the scenarios enumerated above. The proposed algorithms are the focus of the two parts of the dissertation and this is explained in what follows.

1.1 Related Work

This dissertation is not the first body of work to address the modelling challenges described above. Earlier work concerning modelling of the radiation pattern of

reflector antennas include the Jacobi-Bessel method [3] as well as the model-based parameter estimation (MBPE) framework [4–7] popularised by Miller. Other methods involve modelling the angular as well as frequency variation of the pattern, of simple antennas such as dipoles, as a Padé rational function or Slepian modes to capture frequency dependence and polynomials or spherical harmonics to capture angular dependence [8–10]. More recent work models the radiation pattern through characteristics basis function patterns (CBFPs) [11–14] (also part of the MBPE framework). A first attempt at parametrisation of radiation pattern models as a function of the antenna's geometry is made in [15]. The method proposed in [15] is closely related to the techniques in this dissertation in as far as the employed "basis functions" are concerned. However the formulation in [15] is limited to only one variable. In the area of radiation pattern measurements, a technique similar to the CBFP method is discussed in [16], whereas pattern estimation using the signal processing concept of spatially band limited sampling was investigated in a series of papers by Bucci *et al.* [17–20].

We stress that previous work is limited to modelling angular or frequency dependence of the radiation pattern or pattern variation as a function of a single parameter. In this dissertation we propose models that transcend the listed limitations of previous techniques.

S-parameter modelling has been thoroughly covered in several papers in the macromodeling framework [21–25] as well as in an adaptive sampling setting [26–29]. In this dissertation, we couple established S-parameter modelling techniques with the proposed pattern models in order to fully characterise antennas from available (limited) data.

1.2 Contributions

Where this dissertation distinguishes itself from prior work is the extent to which the basic MBPE pattern modelling framework has been generalised and extended to multiple variables to enable the modelling of the radiation pattern with applications to the above mentioned areas of calibration and antenna design.

On the calibration front, a method has been proposed to recover the (unknown) radiation pattern over a wide angular region and wide frequency bandwidth (of up to a decade), using a few directional measurements of the yet to be fully determined pattern at a single frequency. The proposed method is based on collecting many simulated CBFPs at different frequencies and the linear algebraic notion of subspace projection.

Concerning models for antenna design, a more accurate formulation of the technique in [15] has been devised and extended to include dependence on multiple

design parameters. Furthermore, a compact representation of the pattern is used to efficiently model dependence on multiple parameters such as geometry and frequency. Such a representation, in terms of only a few parameters, resulted in the first class of adaptive sampling algorithms that involve the full radiation pattern. Both univariate and multivariate sampling methods are proposed to build models of antenna responses, over a large design space, at a reduced computational cost. Furthermore the new algorithms are coupled with the well-established S-parameter modelling techniques in order to fully characterise antennas at a significantly reduced cost when compared to traditional methods. The obtained models are quick to evaluate and can be used to efficiently carry out standard design activities such as sensitivity analysis, optimisation and design space exploration.

The work presented in this thesis has been published (or submitted) in [30–33], highlighting the novelty and actuality of the accomplished body of work.

1.3 Structure of the Dissertation

This dissertation consists of two parts: Part I is concerned with calibration of reflector antennas where the CBFP framework of [11, 12] is extended to multiple frequencies without requiring additional measurements as discussed in Chapter 2. Part II is concerned with semi-analytical antenna models to be used in a design flow, and consists of Chapters 3 and 4. Chapter 3 focuses on building models of antenna patterns and S-parameters on a fixed grid, with frequency being treated as a "special" variable, i.e., the antenna is simulated at multiple frequencies for each fixed geometry (like in a traditional design work flow). In Chapter 4, a class of adaptive sampling algorithms is presented to efficiently model radiation patterns and S-parameters of antennas as a function of multiple design parameters, including geometry and frequency (hereby treated as an ordinary variable), using a minimum number of electromagnetic (EM) simulations. The proposed algorithms are robust and are guaranteed to converge to accurate models with a fully controllable approximation error.

The proposed methods in both Part I and Part II are validated by means of pertinent numerical examples on a variety of antennas with different radiation mechanisms.

Part I

Pattern Models for Calibration

Chapter 2

Calibration with Characteristic Basis Functions Patterns

The development of next generation radio telescopes such as the MeerKAT [1] and the Square Kilometre Array (SKA) [2] telescopes has brought about the need to develop new generic design as well as calibration techniques. Most existing calibration algorithms employ paraxial approximations to the secondary pattern [34,35] as well as crude approximations, if any, of the frequency dependence of the pattern. Calibration challenges[1] posed by new telescopes include the need to model the secondary pattern of a reflector antenna very accurately up to the second side lobe or possibly down to the noise floor. Gathering such detailed knowledge of the secondary pattern may be time consuming and requires repeated measurements at different frequencies thereby making calibration on a direction by direction basis prohibitively slow.

The SKA and MeerKAT telescopes will make use of reflector antennas to carry out surveys. The structures of these antennas are subject to external forces, such as gravity, that may result in physical deformations leading to a deviation in radiation patterns from ideal operating conditions. A recent paper [12] proposed the use of the characteristic basis function patterns (CBFP) method to rapidly evaluate the radiation pattern of reflector antennas, subject to anticipated physical deformations, from a few directional measurements. In [11], the CBFP method was shown to be the most efficient method to evaluate radiation patterns, compared to analytical models (e.g., Jacobi-Bessel series [3]), in terms of the required number of known samples of the sought after radiation pattern. This is mainly due to the fact that the underlying basis functions (CBFPs) are model-based (i.e., the basis functions have a direct relationship with the physics of the problem at hand) and therefore the CBFP model possesses the least number of solvable parameters

[1] Termed third generation calibration. It takes into account direction-dependent effects (i.e., the reflector antenna's radiation pattern) over a wide angular region.

required to accurately resolve the sought radiation pattern over a large angular region. This translates to fewer directional measurements that are required in order to uniquely and accurately determine the full radiation pattern. Drawing on the benefits of using CBFPs, a technique was proposed in [16] and applied to speed up near-field antenna measurements. The technique in [16] is equipped with an adaptive sampling scheme to select the position where the probe takes near-field measurements. The method in [16] is essentially the same as that in [12], but is applied to a different context and extended to near fields (through a far field to near field transformation). The main difference between the two papers is the intended application: [12] is applied to reflector antenna pattern calibration and [16] to near field antenna measurements. One could argue that these applications are, at their core, one and the same. Both attempt to get information about the actual measured radiation pattern of an antenna, over a wide angular region, through information based on numerical simulations of the patterns (CBFPs) augmented by measurements of the patterns in a few directions. A final note on the work in [12] and [16] is that the same method seems to have been developed independently by at least two groups. This observation stems from the lack of any reference in [16] to previously published work on CBFPs in the antenna radiation pattern estimation context.

The CBFP method, as presented in [11, 12, 16], is only applicable to a single frequency and evaluating the full radiation pattern at a different frequency requires a new set of measurements. In this chapter, a method is devised to extend the work in [12] to evaluate the full pattern in a wide frequency bandwidth without requiring a new set of measurements at each frequency of interest.

2.1 Characteristic Basis Function Patterns

Characteristic basis function patterns are physics-based (i.e., results of accurate computer simulations or measurements) functions that accurately represent the radiation characteristics of antenna systems. This method was originally proposed in [13] to model the radiation pattern of dense antenna arrays. It was later expanded and demonstrated in [14] on a finite array of tapered slot antennas, and the first application to single beam reflector antenna systems was reported in [12], where the CBFP method was applied to calibrate for slowly time-varying effects such as feed and/or sub-reflector displacements due to temperature variations or gravity.

Following the discussion in [12, 14], the CBFP method consists of reconstructing a radiation pattern as a linear combination of a few basis functions as

$$\boldsymbol{F}_r(\Omega, s) = \sum_{n=1}^{N} \alpha_n \boldsymbol{f}_n(\Omega, s), \tag{2.1}$$

where $\boldsymbol{F}_r(\Omega, s) \in \mathbb{C}^{N_p \times 1}$ is the approximated pattern in a general direction $\Omega = (\theta, \phi)$ and at a frequency s. The symbol $\boldsymbol{f}_n(\Omega, s) \in \mathbb{C}^{N_p \times 1}$ denotes the physics-based CBFPs, which may be given by an analytical pattern model, or are directly obtained from EM simulations, or measurements, and N denotes the number of CBFPs. The CBFPs may be the co- or cross-polarised component of the radiation pattern, or the $\theta-$ or $\phi-$component of the radiated electric field. We will use the results of EM simulations as CBFPs throughout this chapter. Note that $N_p = N_\theta N_\phi$, where N_θ and N_ϕ are the number of far field points in the $\theta-$ and $\phi-$directions respectively, with θ denoting the polar angle and ϕ the azimuthal angle in a standard spherical coordinate system.

2.1.1 Generating CBFPs

In a calibration context, the basis functions are generated as follows: the primary basis function corresponds to the radiation pattern under ideal operating conditions while the secondary basis functions are additional patterns modelling several anticipated physical deformations that results in pattern drifts. Sources of pattern drifts include the effects of external forces, such as uneven thermal expansion and gravity, resulting in support arm deformation and reflector surface deformation as reported in [11, 12].

Let $\mathcal{X}$ denote the set of all conceivable physical deformations of a reflector antenna and $\mathcal{F}$ denote the subspace of all radiation patterns emanating from the deformations in $\mathcal{X}$. Furthermore, let $\boldsymbol{f}_1$ denote the primary CBFP and $\boldsymbol{f}_n$ $(n \geqslant 2)$ denote the secondary CBFPs. The general idea is then that the generated set of CBFPs, $\mathcal{S} = \{\boldsymbol{f}_1\} \cup \{\boldsymbol{f}_2, \cdots, \boldsymbol{f}_N\}$, spans the subspace $\mathcal{F}$, i.e., the CBFPs are the basis vectors of $\mathcal{F}$ and an arbitrary pattern in $\mathcal{F}$ can therefore be expressed as a linear combination of the CBFPs.

For instance, in Fig. 2.1, the CBFPs are generated by simulating the effects of support arm deformation in an offset Gregorian system. Such deformation results in displacements of the feed and sub-reflector. The secondary CBFPs are then obtained, through EM simulation, by moving the feed/sub-reflector to positions δ_i, $i = 1, 2, \cdots, 8$, at the corners of the cuboid as illustrated in Fig. 2.1. The primary CBFP corresponds to the pattern at the nominal (or ideal) position δ_0, and the dimensions of the cuboid represent the extremes of the expected deformations.

The objective here is to generate a minimum set of N CBFPs that covers the anticipated deformations in the most efficient manner. The set of CBFPs may be generated upfront by means of the space-filling principle of adhesion, i.e., neighbouring points lie as far away from each other as possible [36].

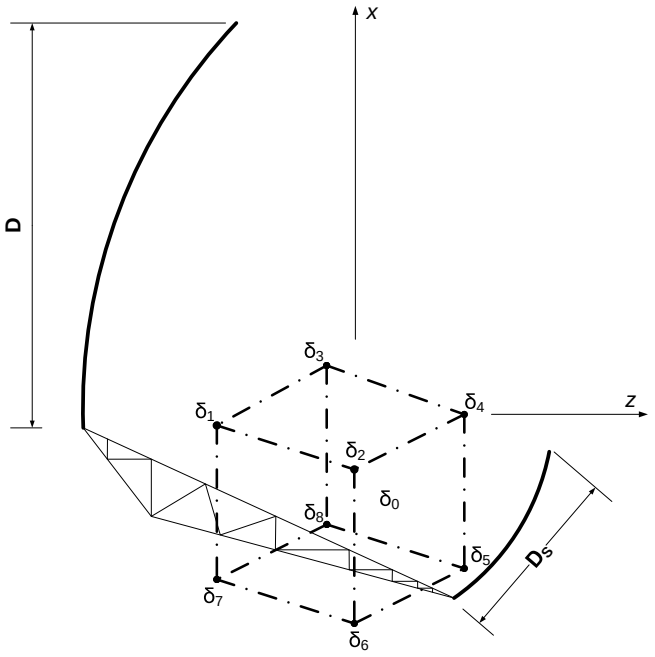

Figure 2.1: Geometry of the reflector antenna on which the CBFP method is executed. The positions of the feed/sub-reflector are designated by δ_j, with δ_0, at the centre of the cube, being the ideal location of the feed/sub-reflector, corresponding to the primary basis function pattern. $\delta_{j\neq 0}$ are the new positions due to support arm deformations, each corresponding to a secondary basis function pattern.

2.1.2 Solving Model Coefficients

The coefficients α_n, in (2.1), are obtained by taking M measurements of $\boldsymbol{F}_r(\Omega)$ and solving the resulting system of linear equations either directly by using the Moore-Penrose pseudo-inverse or by orthogonalising the basis functions, by means of a singular value decomposition (SVD), as a pre-processing step to enhance modelling accuracy [11].

Let $\mathbf{F}_{\mathrm{M}}$ be an $N_p \times N$ matrix whose columns are the CBFPs in (2.1). In applying SVD, only the first N_R ($N_R \leqslant N$) left-singular vectors of $\mathbf{F}_{\mathrm{M}}$ are retained, constituting a (possibly) reduced set of CBFPs, denoted by $\mathbf{U}_{\mathrm{R}} \in \mathbb{C}^{N_p \times N_R}$. These vectors correspond to the singular values of $\mathbf{F}_{\mathrm{M}}$ above a certain threshold value, ϵ, relative to the largest singular value [12]. The model coefficients, for each frequency s, are then given by

$$\boldsymbol{\alpha}_s = [\mathbf{U}_{\mathrm{R}}(\Omega_R)]^{\dagger} \boldsymbol{F}_r(\Omega_R), \tag{2.2}$$

where Ω_R are the N_R distinct directions in which measurements of the yet to be determined pattern $\boldsymbol{F}_r(\Omega)$ are taken, and the superscript † indicates the pseudo-

inverse of a matrix. The recovered full pattern is then given by[2]

$$\boldsymbol{F}_r(\Omega) = \mathbf{R}(\Omega)\boldsymbol{\alpha}_s, \tag{2.3a}$$

$$\mathbf{R}(\Omega) = [\boldsymbol{r}_1(\Omega), \boldsymbol{r}_2(\Omega), \cdots, \boldsymbol{r}_{N_R}(\Omega)], \tag{2.3b}$$

where $\mathbf{R}(\Omega) \in \mathbb{C}^{N_p \times N_R}$ is a matrix whose columns are given by

$$\boldsymbol{r}_k(\Omega) = \frac{1}{\sigma_k}\mathbf{F}_{\mathrm{M}}(\Omega)\boldsymbol{V}_k(\Omega), \tag{2.4}$$

where σ_k is the k^{th} singular value of $\mathbf{F}_{\mathrm{M}}(\Omega)$ and $\boldsymbol{V}_k(\Omega) \in \mathbb{C}^{N \times 1}$ is the corresponding k^{th} column of the right singular matrix $\mathbf{V}(\Omega) \in \mathbb{C}^{N \times N_R}$, resulting from the SVD of $\mathbf{F}_{\mathrm{M}}(\Omega)$.

It is worth mentioning that the accuracy of the solution to (2.2) depends on the selection of the testing points Ω_R, which in turn is directly related to the conditioning of the matrix $\mathbf{U}_{\mathrm{R}}(\Omega_R)$. The inversion is most accurate for a well-conditioned matrix $\mathbf{U}_{\mathrm{R}}(\Omega_R)$. A method was proposed in [12] to select Ω_R so as to minimise the condition number of $\mathbf{U}_{\mathrm{R}}(\Omega_R)$. A similar method is adopted in this work.

Furthermore, since a truncation of the left-singular matrix of the SVD realisation of $\mathbf{F}_{\mathrm{M}}$ is employed[3], a truncation error arises and is given by [37]

$$E_T = \sum_{i=N_R+1}^{N} \sigma_i^2, \tag{2.5}$$

where σ_i is the i^{th} singular value of $\mathbf{F}_{\mathrm{M}}$. The value of the truncation error may, in some cases, be significant and it must therefore be taken into consideration when choosing N_R. A rule of thumb of $\tau = \frac{\sigma_{N_R}}{\sigma_1} = 10^{-6}$, where σ_1 and σ_{N_R} are the first and ${N_R}^{th}$ singular values of $\mathbf{F}_{\mathrm{M}}$, was used as the criterion for selecting N_R in [11,12]. This value of τ is sufficiently small to minimize the truncation error in most cases and is thus used where appropriate in this report.

The CBFP method as described in [11,12,14] (and in the previous paragraphs) is limited to a single frequency and repeated measurements are required to extract model coefficients for different frequencies in a wideband system. The number of such repeated measurements may quickly become large if finely sampled wideband systems are of interest. A method to extend the CBFP method to multiple frequency points is proposed in the next section. The method does not require repeated measurements at different frequencies. It requires only a single set of measurements at a single frequency (retaining the complexity of [11, 12, 14]), and relies on a subspace projection technique. The method is described in detail in the next section.

[2]For a comprehensive tutorial involving the used of right-singular vectors, the reader is referred to Appendix C of [11].

[3]We stress that this is not always the case since $N_R \leqslant N$. i.e., The inequality is not strict.

2.2 Extension to Multiple Frequencies

As mentioned in previous sections, the CBFP method as described in [11, 12, 14] is limited to a single frequency and repeated measurements are required to extract model coefficients for different frequencies in a wideband system.

Given that the secondary pattern varies in a highly non-linear fashion as a function of frequency[4], it is thus a difficult task to mathematically model the frequency dependence of the full pattern.

The challenge of this section is to obtain the model coefficients $\boldsymbol{\alpha}$, after SVD, at different frequencies without taking measurements of the yet to be determined pattern at all frequencies of interest. Fortunately, in a calibration context, CBFPs at many frequencies can easily be generated using EM simulations, which are then exploited to recover the radiation pattern at all frequencies using a subspace projection technique. The technique requires only a few measurements at a single frequency in order to accurately determine the radiation pattern at all other frequencies in the bandwidth of interest.

The main idea behind the extension algorithm is that the model coefficients obtained from the solution of (2.2), at one frequency, are mapped to other frequencies using a set of transformation matrices. The transformation matrices consist of basis vectors of the subspace of all expansion coefficients at various frequencies. These basis vectors are derived from the knowledge of the basis functions at multiple frequencies in a procedure described below.

Consider a set of Q frequency points

$$S = \{s_1, s_2, \cdots, s_Q\}. \tag{2.6}$$

Given a set of N CBFPs for each frequency in S, an $N_R \times N$ transformation matrix, $\mathbf{W}(s_j)$, is generated for each frequency, $s_j \in S$, by sampling each of the first N CBFPs at $M = N_R$ points and solving (2.1) using the SVD method. That is

$$\mathbf{W}(s_j) = [\boldsymbol{w}_1(s_j), \boldsymbol{w}_2(s_j), \cdots, \boldsymbol{w}_N(s_j)], \tag{2.7}$$

where $\boldsymbol{w}_k(s_j)$ is a column vector of model coefficients corresponding to the solution for the k^{th} basis function ($k \in \{1, 2, \cdots, N\}$). The vector $\boldsymbol{w}_k(s_j)$, in (2.7), is obtained by replacing $\boldsymbol{F}_r(\Omega)$, in (2.2), by the actual basis function $\boldsymbol{f}_k(\Omega)$ at a frequency s_j as

$$\boldsymbol{w}_k(s_j) = [\mathbf{U}_{\mathrm{R}}(\Omega_s, s_j)]^{\dagger} \boldsymbol{f}_k(\Omega_s, s_j). \tag{2.8}$$

Each $\boldsymbol{w}_k(s_j)$, in (2.7), is a basis vector of the subspace, Λ_{s_j}, of all expansion coefficients, α_k in (2.1), at a frequency s_j. The basis vectors, $\boldsymbol{w}_k$, span Λ_{s_j} if and

[4]The gain/directivity increases, the half-power beam width decreases and the sidelobe levels and their angular locations are difficult to predict, especially outside the plane of symmetry.

only if the CBFPs span the subspace of all patterns emanating from the expected physical deformations[5].

The expressions in (2.7) and (2.8) are applied to basis functions at Q different frequencies to generate a set of transformation matrices

$$T = \{\mathbf{W}(s_1), \mathbf{W}(s_2), \cdots, \mathbf{W}(s_Q)\}, \tag{2.9}$$

with each transformation matrix containing the basis vectors of Λ_{s_j} at a frequency s_j.

If the basis functions model a sufficiently linear system, then transformation matrices at different frequencies s_p and s_q, in S, are projections of one another and therefore there exists a linear map between model coefficients at s_p and s_q.

To predict an arbitrary pattern at multiple frequencies, a set of $M = N_R$ directional measurements of the pattern are taken at a single frequency $s_p \in S$, from which model coefficients, $\boldsymbol{\psi} = [\alpha_1, \alpha_2, \cdots, \alpha_{N_R}]$, are obtained by solving (2.2) (much like in [12]).

Based on $\boldsymbol{\psi}$, coefficients at other frequencies are determined by first computing the mapping vector $\boldsymbol{\lambda}$ as

$$\boldsymbol{\lambda} = [\mathbf{W}(s_p)]^{\dagger}\boldsymbol{\psi}, \tag{2.10}$$

where $\mathbf{W}(s_p) \in T$.

Once the vector $\boldsymbol{\lambda}$ is found from single frequency measurements, the CBFP model expansion coefficients at any other frequency $s_j \in S$ are then given by the linear combination of the columns of the appropriate transformation matrix $\mathbf{W}(s_j)$, in (2.9), as

$$\boldsymbol{\alpha} = \mathbf{W}(s_j)\boldsymbol{\lambda}. \tag{2.11}$$

The expression in (2.11) allows one to determine the radiation pattern at an arbitrary frequency within the model's range without the need for measurements to be taken at that particular frequency.

An initial computational effort is required to generate the set in (2.9). However, this effort needs to be done only once and the elements of T, in (2.9), may then be stored and used to predict the wideband radiation patterns from single frequency measurements. Negating the need for repeated measurements can dramatically speed up calibration of wideband systems and thus enhancing the method in [12].

It is important to note that the method presented herein relies on the assumption that the modelled system is linear. In a calibration context, the system can be linearised by increasing the number of basis functions within the modelling domain.

The next section presents a few numerical examples to validate the proposed method.

[5]This is the assumption made when generating CBFPs.

2.3 Numerical Examples

Herein, the following examples are given: one involving an analytical Gaussian feed and the other involves a planar sinuous feed [38]. Both feeds illuminate the offset Gregorian reflector shown in Fig. 2.1, with a projected aperture of 13.5 m in diameter similar to the unshaped MeerKAT dishes [39]. The investigated frequency range is a 3 : 1 bandwidth. These examples demonstrate the effectiveness of the proposed technique in modelling the effects of support arm deformation in an offset Gregorian reflector system. The CBFPs are generated as illustrated in Fig. 2.1, and the extent of the movements of the feed/sub-reflector from their ideal positions is given in Table 2.1 [40].

Table 2.1: Positional variations for the sub-reflector and feed. All values are in millimetres.

Direction	Feed	Sub-reflector
$\hat{x}$	± 7.70	± 10.0
$\hat{y}$	± 3.90	± 5.00
$\hat{z}$	± 15.4	± 20.0

Additionally, a decade bandwidth case, where the variation of the feed's position in a 2D plane, is investigated. This is done in order to calibrate for the possible feed misalignment that may arise as a result of the feed selection scheme in the MeerKAT telescope [1].

2.3.1 Gaussian Feed

A -12 dB taper Gaussian feed is used to generate 9 CBFPs, as shown in Fig. 2.1, as well as additional test patterns at random positions within the domain in Table 2.1. The pattern for which the feed and sub-reflector displacements are $\delta_F = (5.467; -3.85; 14.245)$ mm and $\delta_{SR} = (7.1; -5; 18.5)$ mm respectively, which yields the largest modelling error (empirically determined by comparing results of all test patterns), is used to illustrate the effectiveness of the algorithm in Section 2.2.

A plot of the CBFPs, after SVD, is shown in Fig. 2.2a where an increasingly dynamic behaviour, as a function of the angular direction θ, can be observed by comparing the dominant CBFP (single dominant peak) to the higher order ones. Furthermore, the peaks of the various CBFPs indicate the (θ, ϕ) directions in which each CBFP would contribute the most to the reconstructed pattern and hence represent the ideal set of directions in which to take measurements of the (unknown) radiation pattern. The sampling directions, Ω_R, obtained through the heuristic method in [11] (and used in this dissertation) are indeed very close to the angular

directions at which the columns of the left-singular matrix, from SVD realisation of a column-stacked matrix of CBFPs, have their maximum. Fig. 2.2a thus serves as a proof for the efficacy of the heuristic proposed in [11].

Moreover, scaling the CBFPs in Fig. 2.2a with their corresponding singular values reveal that the shape of the radiation pattern is mainly captured by the dominant CBFP (after SVD), as shown in Fig. 2.2b, while the higher order bases mainly contribute to determining other pattern dynamics the exact locations of the side lobes.

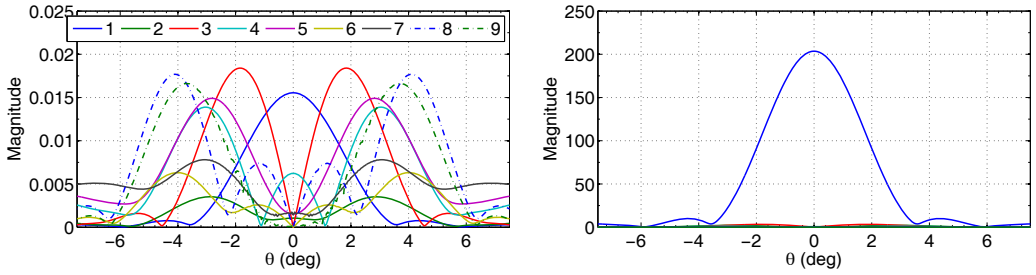

(a) (b)

Figure 2.2: The traces show the entries of the left-singular matrix of the CBFPs after SVD, in the $\phi = 90°$ plane. The dominant CBFP exhibits slow angular variation while higher order CBFPs have a more dynamic variation, as shown by the increasing number of dominant peaks within the displayed angular region. (a) The basis functions are not scaled with their corresponding singular values. (b) Scaled basis functions.

Experiments showed that retaining the first 6 left-singular columns, after SVD, led to an approximated pattern, $\boldsymbol{F}_r(\Omega)$ in (2.1), with minimum approximation error (i.e., the truncation error E_T in (2.5) is very small and the condition number of $\mathbf{U}_{\mathrm{R}}$ in (2.8) is also small), and this finding is thus applied in this example.

Fig. 2.3 shows the predicted pattern at $f = 1.22$ GHz using projected model coefficients obtained from sampling the antenna's pattern at 0.74 GHz.

The maximum normalised error of the full predicted pattern, shown in Fig. 2.3, is -41.98 dB. The maximum error, obtained by directly applying the CBFP method at 1.22 GHz, is -65.81 dB, demonstrating a maximum absolute difference of only 7.45×10^{-3} with the results of the proposed algorithm. The error is normalised relative to the main beam's peak.

A natural question arises as to which frequency, s_p, is most suitable for measurement purposes (and thus solving for ψ) in order to have predicted patterns with the least modelling error for a given bandwidth.

For the considered $3:1$ bandwidth, choosing s_p to be the centre frequency (arithmetic mean of S) leads to maximum modelling errors below -43 dB, which is lower than having s_p being chosen as either of the extreme frequencies in the band of interest as shown in Fig. 2.4, or at any other intermediate frequency.

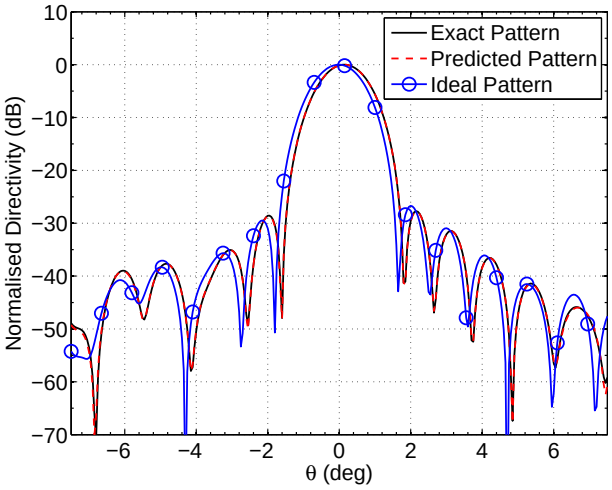

Figure 2.3: Predicted pattern in the $\phi = 150°$ plane. The ideal pattern corresponds to the primary basis function at 1.217 GHz. This particular cut is the $\phi-$cut in which the maximum prediction error of the full radiation pattern occurs.

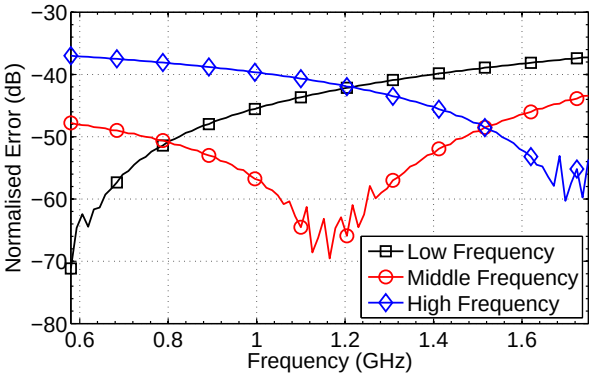

Figure 2.4: Gaussian feed: Maximum normalised modelling error as a function of frequency. Low Frequency: $s_p = 0.58$ GHz. Middle Frequency: $s_p = 1.17$ GHz. High Frequency: $s_p = 1.75$ GHz.

2.3.2 Planar Sinuous Feed

In this example, 12 basis functions are generated in a similar manner as in Section 2.3.1, except that a planar sinuous antenna, with a frequency-dependent radiation pattern (shown in Fig. 2.5), is used as the feed. That is, in addition to the positions in Table 2.1 (see Fig. 2.1), additional patterns are generated at the following positions: $\delta_9^F = (-3.85; -3.85; -11.55)$ mm, $\delta_{10}^F = (2.70; 2.31; -10.01)$ mm and $\delta_{11}^F = (5.47; -3.85; 14.25)$ mm. The equivalent sub-reflector positions are given by $\delta_k^{SR} = \delta_k^F / 0.77$.

The test pattern (not included in the set of basis functions), in this example, is given by positions $\delta_F = (4.7; -3.5; 11.2)$ mm and $\delta_{SR} = (6.10; -4.55; 14.55)$ mm.

All 12 left-singular columns, after SVD, are used in the modelling process since it results in the smallest approximation errors as shown in Fig. 2.6.

Fig. 2.7 shows predictions at frequencies of $f = 0.894$ and $f = 1.53$ GHz, obtained by taking pattern measurements, in 12 distinct directions (θ, ϕ), at $f = 0.82$

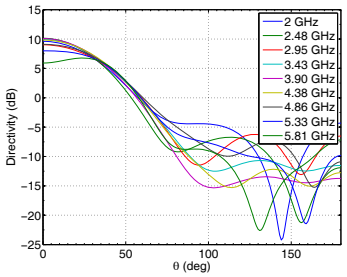

Figure 2.5: Typical radiation pattern of a planar sinuous antenna for difference frequencies.

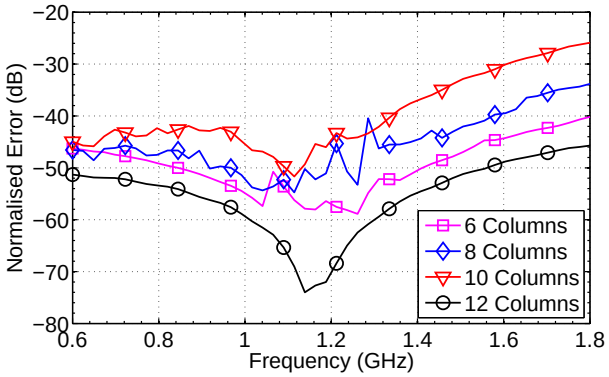

Figure 2.6: Normalised errors for different numbers of retained left-singular columns, after singular value decomposition of the original set of 12 CBFPs. The normalised errors are obtained by sampling at the middle frequency ($s_p = 1.16$ GHz) and applying the method in Section 2.2. The small condition numbers in the case of retaining 6 or 8 columns offset the effects of the resulting large truncation error. For matrices with similar conditioning, like the case of 10 and 12 columns, the effect of the truncation error is clearly visible.

GHz. The errors of the pattern cuts, in which maximum reconstruction inaccuracies occur, are also shown.

As shown in Fig. 2.8, the application of the algorithm in Section 2.2 by solving for model coefficients in (2.2) at or near the centre frequency leads to the least modelling errors, smaller than -45 dB. The errors in Fig. 2.8 are typical for feed/sub-reflector displacements within the domain in Table 2.1.

This example demonstrates the accuracy of the proposed method when a practical feed, with a non-symmetric frequency-dependent radiation pattern, is used.

2.3.3 Decade Bandwidth Case

As future radio telescopes, such as the SKA, are to operate over very large bandwidths, possibly a decade, it is therefore imperative to evaluate the proposed method over a decade bandwidth.

Due to severe non-linearities as a result of feed and/or sub-reflector displacements at high frequencies (above about 2.5 GHz), a much larger number of basis functions is required to accurately estimate the pattern using (2.1). Furthermore, the resulting high dimensionality of the model coefficients vector, $\boldsymbol{\alpha}$, leads to a

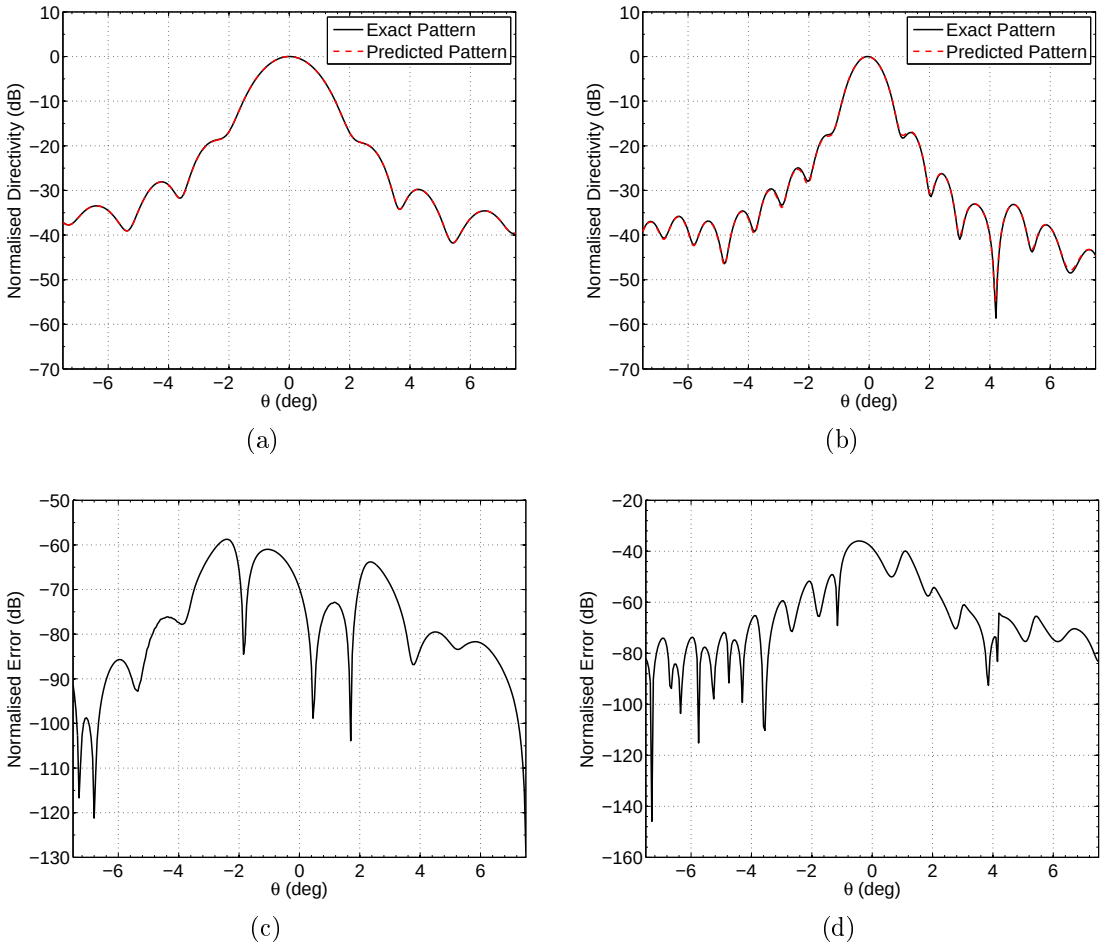

Figure 2.7: Reconstructed radiation patterns obtained by measuring at $f = 0.82$ GHz: (a) Pattern cut in the $\phi = 90°$ plane at $f = 0.894$ GHz. (b) $\phi = 55°$ cut at $f = 1.53$ GHz. (c) Normalised error in the $\phi = 90°$ plane at $f = 0.894$ GHz. (d) Normalised error in the $\phi = 55°$ plane at $f = 1.53$ GHz.

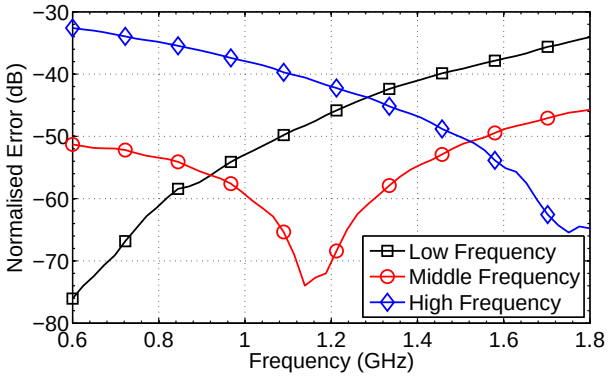

Figure 2.8: Sinuous feed: Maximum normalised modelling error as a function of frequency. Low Frequency: $s_p = 0.60$ GHz. Middle Frequency: $s_p = 1.16$ GHz. High Frequency: $s_p = 1.80$ GHz.

somewhat degraded level of accuracy if (2.1) is applied directly.

To address the accuracy problem, $k-$sparse approximation [41] is used to greatly reduce the number of significant entries of $\boldsymbol{\alpha}$, leading to improvements in modelling accuracy of almost an order of magnitude as can be seen in Table 2.2 and Fig. 2.9a.

In $k-$sparse approximation of the pattern, only the first k entries of the vector $\boldsymbol{\alpha}$ are retained, while the remaining entries, which contribute to numerical noise in the reconstruction process in this case, are set to zero.

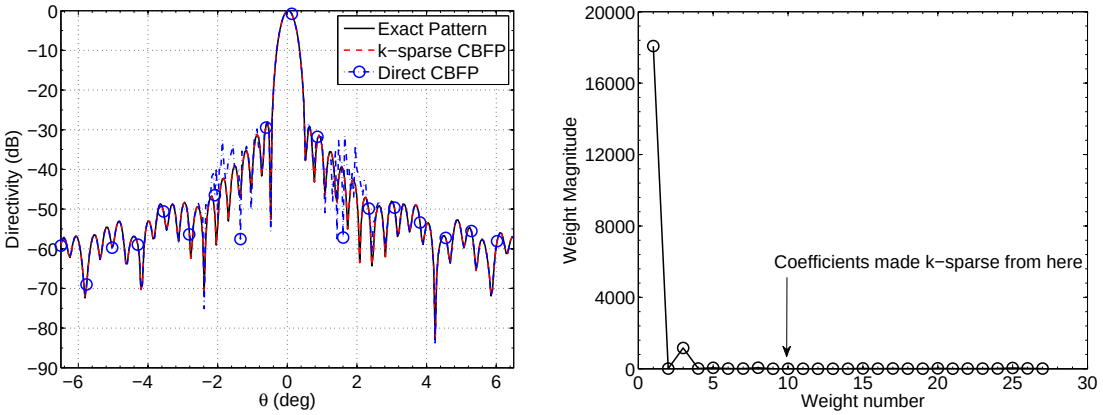

(a) (b)

Figure 2.9: Comparison of reconstructed patterns by directly employing the CBFP method in (2.1) and by using the CBFP method augmented by a $k-$sparse approximation of the model coefficient vector, in the $\phi = 90°$ plane, at 4.11 GHz. Notice the vast improvement in modelling capability with a maximum normalised error decreasing from -34.43 dB to -57.39 dB. (b) Magnitude of the approximated model coefficients.

Table 2.2: Comparison of maximum normalised errors obtained using the direct CBFP method vs. $k-$sparse CBFP.

Frequency (GHz)	Direct CBFP Error (dB)	$k-$sparse CBFP Error (dB)
0.58	-66.13	-87.69
1.50	-49.50	-80.34
2.50	-37.14	-65.67
3.50	-47.38	-64.96
4.57	-44.42	-56.59
5.03	-33.91	-58.08
5.80	-50.11	-58.62

In the examples of Fig. 2.9a and Table 2.2, 34 basis functions are used, of which, 27 are retained after SVD. The model coefficients vector, $\boldsymbol{\alpha}$, has a dimension of 27 and its last 18 entries are set to zero, via $k-$sparse approximation. Application of $k-$sparse approximation is straight-forward in this case, because the entries of the vector $\boldsymbol{\alpha}$ are sorted in order of their contribution as a result of SVD, as is evident in Fig. 2.9b. The secondary patterns of this case are generated by moving the feed in a plane with $x-$ and $y-$ranges shown in Table 2.1, and a maximum grid size of $0.02\lambda_{max}$, where λ_{max} is the wavelength at the maximum frequency.

The secondary basis function patterns, generated in this manner, simulate possible positioning errors that might arise with the feed selector scheme in the MeerKAT and the proposed SKA telescopes [2]. The feed used in this example is a Gaussian feed with an edge taper of -12 dB.

The method in Section 2.2, augmented with $k-$sparse approximation, is then applied to estimate the full radiation pattern over a decade bandwidth, with maximum estimation errors less than -45 dB across the entire band as shown in Fig. 2.10. As in previous examples, sampling at or near the centre frequency of the band yields the least overall reconstruction error.

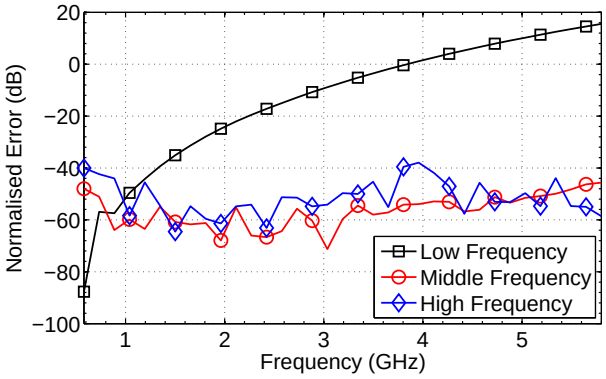

Figure 2.10: Maximum normalised modelling error as a function of frequency. Low Frequency: $s_p = 0.58$ GHz. Middle Frequency: $s_p = 3.04$ GHz. High Frequency: $s_p = 5.80$ GHz. The calculated errors are typical of patterns obtained as a result of moving the feed anywhere within the $x - y$ plane delimited by the values in Table 2.1.

2.4 Conclusion

An extension of the CBFP method to multiple frequencies has been presented in this chapter. The algorithm uses simple techniques from linear algebra to efficiently estimate the radiation pattern at multiple frequencies using a few directional measurements of the pattern obtained at a single frequency. It is shown that dimensionality reduction by means of $k-$sparse approximation vastly improves reconstruction errors in cases where the number of basis function is large. The proposed method does not require a priori knowledge of the exact deformation of the system and is applicable for a bandwidth ratio of up to $10:1$ with estimation errors less than -40 dB over several side lobes. This algorithm can potentially greatly speed up the calibration of modern wideband radio telescopes by providing accurate radiation patterns across a wide frequency bandwidth.

The work presented in this chapter was published in 9^{th} European conference on antennas and propagation [30].

Part II

Parameterized Models for Antenna Design

Chapter 3

Parametric Modelling of Antenna Patterns

Modern antenna design procedures often involve activities such as design space exploration, optimisation and sensitivity analysis. These normally require multiple full-wave and/or asymptotic electromagnetic (EM) analyses of the antenna for different geometric parameter values, and are expensive due to the typically large computational cost per simulation. Design targets often involve figures of merit that are derived from the knowledge of the full radiation pattern (e.g., aperture efficiency, directivity or cross-polarisation) or the design targets may indeed involve the radiation pattern over a large angular region (e.g., pattern masks in antennas used for satellite communication, radar cross section studies). A typical antenna design cycle can thus greatly benefit from a method that rapidly provides radiation patterns, with an accuracy similar to computationally expensive EM simulations, for varying combinations of the antenna's geometrical parameters (i.e., the design variables).

This chapter describes a novel data-driven method to model the radiation patterns (over a large angular region) of antennas as a function of the geometry of the antenna. The radiation pattern model consists of a linear combination of characteristic basis function patterns (CBFPs), where the expansion coefficients of the CBFPs are functions of geometrical features of the antenna. We also include a method to model the geometry-dependent variation of S-parameters, in order to fully characterise the antenna, from the same set of EM simulations.

3.1 Related Work

It is widely known that the efficiency of data-driven techniques is enhanced if the underlying models have a connection with the physics of the problem at hand, as such models have the least number of solvable parameters and thus require

fewer data in order to yield accurate results. This modelling methodology is called model based parameter estimation (MBPE). For instance, it has been shown in [11] that CBFP models yield accurate radiation patterns using far fewer data points compared to methods such the Jacobi-Bessel pattern model[1].

MBPE is a modelling technique described by Miller in [4–7], and can be summarized as follows: a few points are used to interpolate a given response in time/frequency or in terms of angular dependence, using an underlying function that is based on the physics of the problem at hand (e.g., the sinc function for the radiation pattern of a reflector antenna in [6]).

Following the MBPE approach, techniques to model radiation patterns of simple feeds such as dipoles have been described in [8, 9]. These models interpolate the pattern in both frequency and a wide angular region $\Omega = (\theta, \phi)$ in the spherical coordinate system. The frequency dependence is expressed as a Padé rational function, while the angular variation of the pattern is expressed as polynomials in [8] or in terms of spherical harmonics [9]. Another pattern modelling method was proposed in [10] where the angular variation is also expressed as spherical harmonics while the frequency dependence is described using Slepian mode expansion.

It is worth noting that the methods in [4–10] are not immediately suitable for design activities as the pattern models are not parameterized with respect to the antenna's physical dimensions (i.e., the design parameters). This limitation is addressed in this chapter, where a model of the full radiation pattern as a function of varying antenna geometry is proposed.

A method to interpolate radiation patterns was recently proposed in [15], where the variation of the physical problem was captured by imposing a function such as a complex exponential or orthogonal polynomials. The method in [15] is based on a linear least-squares regression technique and its accuracy is strongly dependent upon the choice of the fitting function. Furthermore, it is limited to a single varying parameter.

This chapter presents a method to accurately model the radiation pattern of an antenna, subject to multiple varying design parameter (i.e., geometry of the antenna). The method utilises CBFPs, a parametrisation of the expansion coefficients based on a subspace projection technique as well as positive interpolation operators. The proposed method is explained in detail in what follows.

3.2 Radiation Pattern Modelling

The problem at hand consists of accurately predicting radiation patterns corresponding to an arbitrary set of geometric parameters $\boldsymbol{x}^*$, within a given design

[1] Essentially a weighted summation of the product of sinusoids and Bessel functions.

space $\mathcal{D}$. In Chapter 2, a matrix projection based method was proposed to obtain expansion weights at multiple frequencies without explicitly solving (2.1) at each frequency of interest. The methods in [15] and Chapter 2 are limited to one dimensional parameter variations. To be more useful in a practical antenna design, the radiation pattern models [15] need to be extended to account for the variation of multiple geometric parameters, and this is presented in what follows.

Consider a limited estimation set of Q points

$$\mathcal{X}^{\text{est}} = \{\boldsymbol{x}_1, \boldsymbol{x}_2, \cdots, \boldsymbol{x}_Q\}, \tag{3.1}$$

and a corresponding set of CBFPs

$$\mathcal{F}^{\text{est}} = \{\boldsymbol{f}_1^e(\Omega, s), \boldsymbol{f}_2^e(\Omega, s), \cdots, \boldsymbol{f}_Q^e(\Omega, s)\}, \tag{3.2}$$

where $\boldsymbol{x}_k$ denotes a vector of geometric parameters of the antenna, $\boldsymbol{f}_k^e(\Omega, s)$ is the corresponding radiation pattern and $\mathcal{X}^{\text{est}} \in \mathcal{D}$.

Starting from Q basis functions in (3.2), a $Q \times Q$ matrix, $\mathbf{W}(s_j)$, of expansion coefficients is generated for each frequency s_j by sampling each of the Q CBFPs at Q distinct points, Ω_s, and solving (2.1) using the SVD method. This yields a matrix, similar to the one in (2.7), whose columns are the basis vectors of the subspace of all expansion coefficients for the radiation patterns emanating from any point in the design space $\mathcal{D}$. The basis vectors, at a frequency s_j, are given by

$$\boldsymbol{w}_k(s_j) = [\mathbf{U}_{\text{R}}(\Omega_s, s_j)]^{-1} \boldsymbol{f}_k^e(\Omega_s, s_j), \tag{3.3}$$

where $\mathbf{U}_{\text{R}}$ is the left-singular matrix of the SVD realisation of a column-stacked matrix of the CBFPs in (3.2).

Each basis vector, $\boldsymbol{w}_k(s_j)$, is a unique vector with no zero entry, effectively linking each unique point in the estimation set to a unique vector of expansion coefficients, which is necessary for parametrisation. Equation (3.3) can be interpreted as as an orthogonal projection of the radiation patterns in (3.2) into a subspace, $\mathcal{W}$, that is spanned by the columns of the matrix $\mathbf{W}$. The orthogonal projection is carried out using a common matrix $\mathbf{U}_{\text{R}}$ for all estimation points. This results in the CBFP expansion coefficients, in the subspace $\mathcal{W}$, having a smooth geometry-dependent variation over the constrained design space of interest, such that the expansion coefficients at an arbitrary point in the design space can be obtained by multivariate interpolation of the columns of $\mathbf{W}$ using, for example, simplicial methods [31].

Therefore, the recovered radiation pattern in (2.3a) is reformulated as

$$\boldsymbol{F}_r(\Omega, s) = \mathbf{R}(\Omega, s)\boldsymbol{\alpha}_v(\boldsymbol{x}^*), \tag{3.4}$$

where, for a one-dimensional parametric modeling problem,

$$\boldsymbol{\alpha}_v(\boldsymbol{x}^*) = \sum_{k=1}^{Q} \boldsymbol{T}_{x_k} \ell_k(\boldsymbol{x}^*), \tag{3.5}$$

and $\boldsymbol{x}^*$ is a point within the design space $\mathcal{D}$ where the radiation pattern is to be evaluated. The symbol $\boldsymbol{T}_{x_k}$ represents the known interpolation nodes given by the expansion coefficients computed in (3.3) and the interpolation kernel $\ell_k(\boldsymbol{x}^*)$ is a scalar function with properties

$$\ell_k(\boldsymbol{x}_i) = 1, \quad \text{if } \boldsymbol{x}_i \in \mathcal{X}^{\text{est}}, \tag{3.6a}$$

$$\ell_k(\boldsymbol{x}_i) \geq 0. \tag{3.6b}$$

For instance, $\ell_k(\boldsymbol{x}^*)$ can be chosen as a piecewise linear function or a cubic spline whose robust implementations are readily available in MATLAB [42].

For the $N-$dimensional parametric modeling case, $\boldsymbol{\alpha}_v(\boldsymbol{x}^*)$ can be expressed as

$$\boldsymbol{\alpha}_v(\boldsymbol{x}^*) = \sum_{k_1=1}^{Q} \cdots \sum_{k_N=1}^{Q} \boldsymbol{T}_{(x_{k1} \cdots x_{kN})} \ell_{k_1}(x_1^*) \cdots \ell_{k_N}(x_N^*), \tag{3.7}$$

where $\boldsymbol{x}^* = [x_1^*, \cdots, x_N^*]$ and the kernel functions $\ell_{k_i}(\cdot)$ satisfy (3.6).

In contrast with the technique in [15], the accuracy of the proposed method doesn't depend on a judiciously chosen fitting function, but it relies on a well-conditioned common projection matrix, $\mathbf{U}_{\text{R}}$, that emanates from the SVD of a matrix of CBFPs with the property of having a very small minimum singular value (typically $< 10^{-3}$). Furthermore, the proposed method can handle more than one varying design parameter, representing a significant improvement over the state of the art in [15].

Modelling the pattern, over a full sphere, can be accomplished by having two sets of CBFPs: one consisting of the $\theta-$component of the radiated electric far-field $\mathcal{F}_\theta^{\text{est}}$, and the other set consists of the $\phi-$component of the radiated far-field $\mathcal{F}_\phi^{\text{est}}$. The modelling steps (3.3)$-$(3.7) are then performed separately using $\mathcal{F}_\theta^{\text{est}}$ and $\mathcal{F}_\phi^{\text{est}}$ respectively and the resulting full radiated far-field may then be obtained.

3.3 S-Parameter modeling

Although the focus of this chapter is on the modelling of radiation patterns, this section briefly discusses how to parametrically model the associated scattering parameters in order to completely characterise the antenna.

A set of S-parameters is obtained from EM simulations for each point in the estimation set in (3.1). Since the number of points in the estimation set is typically

small, statistical modeling techniques such as Kriging, co-Kriging or neural networks [43–45] are not suitable to accurately model the S-parameter variations over the design space of interest. Instead, parametric macromodeling methods [22,46–49] are used.

The parametric macromodeling technique begins by fitting a frequency-dependent rational function in pole-residue form, using the vector fitting (VF) algorithm [50], to S-parameter data. The rational function is of the form

$$H^p_{\boldsymbol{x}_i}(s) = r_0 + \sum_{n=1}^{K} \frac{r_n}{s - z_n}, \tag{3.8}$$

where r_0 is the direct coupling constant, r_n are the residues and z_n are the system's poles, which are determined iteratively using vector fitting [50], and K is the order of the approximation. Note that r_0, r_n and z_n are dependent on the design space point $\boldsymbol{x}_i$ in the estimation set (3.1). The expression in (3.8) is then converted to a Gilbert state-space realisation [51], where the transfer function is given by

$$H_{\boldsymbol{x}_i}(s) = \mathbf{C}_{\boldsymbol{x}_i} \left(s\mathbf{I} - \mathbf{A}_{\boldsymbol{x}_i}\right)^{-1} \mathbf{B}_{\boldsymbol{x}_i} + \mathbf{D}_{\boldsymbol{x}_i}, \tag{3.9}$$

and the matrices $\mathbf{A}_{\boldsymbol{x}_i} \in \mathbb{C}^{K\times K}$ is a diagonal matrix of poles, $\mathbf{C}_{\boldsymbol{x}_i} \in \mathbb{C}^{1\times K}$ is a row vector of residues, and $\mathbf{B}_{\boldsymbol{x}_i} \in \mathbb{N}^{K\times 1}$ is a unity vector while $\mathbf{D}_{\boldsymbol{x}_i} \in \mathbb{R}$ equals the direct coupling term r_0. The expression in (3.9) is henceforth referred to as a *root macromodel*, and all root macromodels $H_{\boldsymbol{x}_i}(s)$, with $\boldsymbol{x}_i \in \mathcal{X}^{est}$, have the same order K. The parametric macromodel may then be obtained by interpolation of the state-space matrices as

$$\widetilde{H}(\boldsymbol{x}^*, s) = \sum_{k=1}^{Q} \boldsymbol{T}_{x_k} \ell_k(\boldsymbol{x}^*), \tag{3.10}$$

where $\boldsymbol{T}_{x_k}$ represents a state-space matrix ($\mathbf{A}_{\boldsymbol{x}_k}, \mathbf{B}_{\boldsymbol{x}_k}, \mathbf{C}_{\boldsymbol{x}_k}$ or $\mathbf{D}_{\boldsymbol{x}_k}$) and $\ell_k(\boldsymbol{x}^*)$ is the interpolation kernel satisfying (3.6).

However, the interpolation of Gilbert state-space matrices may suffer from a non-smooth variation of the state-space matrices over the design space due to the sensitivity of poles to even slight deviations from their nominal values, and this may lead to inaccurate results [48]. For this reason, similarity transforms are first applied to the state-space matrices, with the result being that all state-space matrices corresponding to the points (3.1) are projected into a common subspace. Such a projection leads to a smooth variation of the entries of the state-space matrices over the design space of interest. The parametrisation is then completed by interpolating the state matrices using positive interpolation kernels.

Note that there are infinitely many possible similarity transforms and deriving an optimal transform is still an open problem. However, popular similarity transforms include the barycentric and Sylvester transforms, details of which can be

found in [48, 49]. For completeness, a brief discussion of the barycentric parametric macromodelling approach is provided in what follows.

A more accurate parametric macromodel is obtained by converting the pole-residue transfer function in (3.8) into the barycentric form [49] as

$$H^b_{\boldsymbol{x}_i}(s) = \frac{\boldsymbol{F}_0 + \sum_{n=1}^{K} \boldsymbol{F}_n \phi_n(s)}{f_0 + \sum_{n=1}^{K} f_n \phi_n(s)}, \tag{3.11}$$

where the frequency-dependent basis function is defined as

$$\phi_n(s) = \frac{1}{s - a_n} \tag{3.12}$$

and the system's poles, a_n, are fixed and independent[2] of any design space point $\boldsymbol{x}_i$. The poles, occurring in conjugate pairs, are typically chosen to be linearly spaced over the bandwidth of interest (i.e., $[f_{min}, f_{max}]$) as

$$a_n = p_r \pm j \cdot p_i, \tag{3.13}$$

where $j = \sqrt{-1}$, $p_r = -p_i \times 10^{-3}$ and $p_i = [2\pi f_{min} : \frac{2\pi(f_{max} - f_{min})}{[0.5K]} : 2\pi f_{max}]$ [22, 49, 50].

The parameters of the numerator and denominator of (3.11) are found by imposing that $H^b_{\boldsymbol{x}_i}(s) = H^p_{\boldsymbol{x}_i}(s)$, which yields the following conditions:

$$\sum_{n=1}^{K} f_n \prod_{\substack{n'=1 \\ n' \neq n}}^{K} (z_l - a_{n'}) = -f_0 \prod_{n'=1}^{K} (z_l - a_{n'}) \quad \text{for } l = 1, \cdots, K, \tag{3.14}$$

$$\boldsymbol{F}_n = f_n \cdot H^p_{\boldsymbol{x}_i}(a_n) \quad \text{for } n = 1, \cdots, K, \tag{3.15}$$

$$\boldsymbol{F}_0 = f_0 \cdot r_0. \tag{3.16}$$

It is easy to prove the relation in (3.14) by expanding the expression in (3.11) as

$$H^b_{\boldsymbol{x}_i}(s) = \frac{\boldsymbol{F}_0 + \sum_{n=1}^{K} \boldsymbol{F}_n \phi_n(s)}{f_0 + \sum_{n=1}^{K} f_n \phi_n(s)} = \frac{\boldsymbol{F}_0 \prod_{n=1}^{K}(s - a_n) + \sum_{n=1}^{K} \boldsymbol{F}_n \prod_{\substack{k=1 \\ k \neq n}}^{K}(s - a_n)}{f_0 \prod_{n=1}^{K}(s - a_n) + \sum_{n=1}^{K} f_n \prod_{\substack{k=1 \\ k \neq n}}^{K}(s - a_n)}, \tag{3.17}$$

and setting the denominator to zero when $s = z_n$ since (3.11) and (3.8) are equivalent. By fixing the value of f_0, the coefficients, f_n, can be obtained from the system of linear equations in (3.14). Condition (3.15) originates from setting $H^b_{\boldsymbol{x}_i}(a_n) = H^p_{\boldsymbol{x}_i}(a_n)$ and knowing f_n, the coefficients $\boldsymbol{F}_n$ can thus be solved. The

[2] This effectively addresses the pole sensitivity issue elucidated earlier, since direct pole interpolation is avoided.

final condition, (3.16), is found by imposing the equality of the pole-residue and barycentric transfer functions as $s \to \infty$.

Having computed the coefficients of the transfer function in (3.11), a state-space realization can then be obtained by first deriving state-space matrices $\{\mathbf{A}_{\boldsymbol{x}_i}^{num}, \mathbf{B}_{\boldsymbol{x}_i}^{num}, \mathbf{C}_{\boldsymbol{x}_i}^{num}, \mathbf{D}_{\boldsymbol{x}_i}^{num}\}$ and $\{\mathbf{A}_{\boldsymbol{x}_i}^{den}, \mathbf{B}_{\boldsymbol{x}_i}^{den}, \mathbf{C}_{\boldsymbol{x}_i}^{den}, \mathbf{D}_{\boldsymbol{x}_i}^{den}\}$ for the numerator and denominator of (3.11) respectively [48, 49]. The state matrices are given by

$$\mathbf{A}_{\boldsymbol{x}_i}^{num} = \mathbf{A}_{\boldsymbol{x}_i}^{den} = \text{blkdiag}\{a_n \mathbf{I}_P\}, \tag{3.18a}$$
$$\mathbf{B}_{\boldsymbol{x}_i}^{num} = \mathbf{B}_{\boldsymbol{x}_i}^{den} = [\mathbf{I}_P, \cdots, \mathbf{I}_P]^T, \tag{3.18b}$$
$$\mathbf{C}_{\boldsymbol{x}_i}^{num} = [\boldsymbol{F}_1, \cdots, \boldsymbol{F}_K], \tag{3.18c}$$
$$\mathbf{C}_{\boldsymbol{x}_i}^{den} = [f_1 \mathbf{I}_P, \cdots, f_K \mathbf{I}_P], \tag{3.18d}$$
$$\mathbf{D}_{\boldsymbol{x}_i}^{num} = \boldsymbol{F}_0, \tag{3.18e}$$
$$\mathbf{D}_{\boldsymbol{x}_i}^{den} = f_0 \mathbf{I}_P, \tag{3.18f}$$

where $n = 1, \cdots, K$, $\mathbf{I}_P$ is an identity matrix of order P and the superscript ^{T} denotes the transpose operator. The final state-space matrices of the barycentric transfer function (3.11) are then obtained, after some algebraic manipulations, as

$$\widetilde{\mathbf{A}}_{\boldsymbol{x}_i} = \mathbf{A}_{\boldsymbol{x}_i}^{den} - \mathbf{B}_{\boldsymbol{x}_i}^{den} \left(\mathbf{D}_{\boldsymbol{x}_i}^{den}\right)^{-1} \mathbf{C}_{\boldsymbol{x}_i}^{den}, \tag{3.19a}$$
$$\widetilde{\mathbf{B}}_{\boldsymbol{x}_i} = \mathbf{B}_{\boldsymbol{x}_i}^{den} \left(\mathbf{D}_{\boldsymbol{x}_i}^{den}\right)^{-1}, \tag{3.19b}$$
$$\widetilde{\mathbf{C}}_{\boldsymbol{x}_i} = \mathbf{C}_{\boldsymbol{x}_i}^{num} - \mathbf{D}_{\boldsymbol{x}_i}^{num} \left(\mathbf{D}_{\boldsymbol{x}_i}^{den}\right)^{-1} \mathbf{C}_{\boldsymbol{x}_i}^{den}, \tag{3.19c}$$
$$\widetilde{\mathbf{D}}_{\boldsymbol{x}_i} = \mathbf{D}_{\boldsymbol{x}_i}^{num} \left(\mathbf{D}_{\boldsymbol{x}_i}^{den}\right)^{-1}. \tag{3.19d}$$

An accurate parametric model, within the design space $\mathcal{D}$, may then be obtained by interpolating the state-space matrices (3.19a)–(3.19d) by using (3.10).

3.4 Method Complexity

The pattern modelling algorithm (Sec. 3.2) involves simple algebraic operations such as SVD and matrix inversions (of very small matrices), and a serial (as opposed to parallel) implementation provides sufficiently fast model building and evaluation times. E.g., a model with 49 CBFPs (over a full sphere with $N_\theta = 181$ and $N_\phi = 361$) is built in 11.89 seconds per frequency point, and evaluated in 0.32 seconds (see Sec. 3.5 for details on the computing platform). However, the building time can be significantly reduced as the algorithm lends itself to a certain degree of parallelism:

1. The computation of each column, $\boldsymbol{w}_k(s_j)$, of $\mathbf{W}(s_j)$ in (3.3) is independent for each $k \in \{1, \cdots, Q\}$ and can therefore be done in parallel.

2. The matrix $\mathbf{W}(s_j)$ can be computed in parallel for each frequency s_j.

The $S-$parameter modelling algorithm in Sec. 3.3 is typically an order of magnitude faster compared to the pattern modelling algorithm, both in terms of model construction and evaluation. Furthermore, it also lends itself to some level of parallelism as the construction of root macromodels is done independently for each point in the design space.

Both algorithms in this chapter can be executed on estimation points in a uniform or scattered grid. The number of EM simulations required, in the estimation set (3.1), depends on the number of parameters involved and on the dynamic behaviour over the design space.

3.5 Numerical Examples

In this section, the method proposed in Sec. 3.2 is validated through some examples with different antennas, illustrating the versatility of the method. The worst case root mean square error ($\varepsilon_{\max}^{\mathrm{RMS}}$), between the parametric models and the validation data samples, is chosen to assess the quality of both the pattern and return loss models. The error metric is given by

$$\varepsilon^{\mathrm{RMS}}(\boldsymbol{x}) = \sqrt{\frac{1}{N_d}\sum_{k=1}^{N_d}\left|G_k(\boldsymbol{x}) - \widetilde{G}_k(\boldsymbol{x})\right|^2}, \tag{3.20}$$

$$\varepsilon_{\max}^{\mathrm{RMS}} = \varepsilon^{\mathrm{RMS}}(\boldsymbol{x}_m), \tag{3.21}$$

where $\boldsymbol{x}$ is a point in the validation set and $G_k(\boldsymbol{x})$ is the validation data, $\widetilde{G}_k(\boldsymbol{x})$ is the prediction from the model, N_d is the number of sample points and $\boldsymbol{x}_m$ is the point in the validation set that maximises (4.5).

The number of points in the estimation, in this chapter, is selected beforehand by trial and error. This ambiguity in selecting the number of estimation points is addressed in Chapter 4, where the points in the estimation set are selected adaptively.

All experiments are performed using MATLAB [42], on a 64-bit Windows platform with an Intel Core i7 – 2600 CPU at 3.4 GHz and 16 GB of RAM.

3.5.1 Dipole Antenna

The effect of varying the length of a vertical dipole antenna, radiating in free space, is modelled in this example. This example is similar to the modelling example considered in [8], where we model the effects of varying the length of the dipole on the pattern at one frequency instead of modelling the frequency dependence of the pattern of a fixed length dipole as was done in [8]. The proposed method, however, does not attempt to interpolate the spatial distribution of the radiation pattern.

The length of the antenna is given as $l = x\lambda_0$, where λ_0 is the wavelength at $f_0 = 842.86$ MHz, and $x \in [0.5, 1.5]$. The estimation set consists of 15 points uniformly sampled in the range $[0.5, 1.5]$. The model is validated at 20 randomly generated points (not in the estimation set) within the modelling range. All EM simulations are done using FEKO [52], a commercial Method of Moments (MoM) solver.

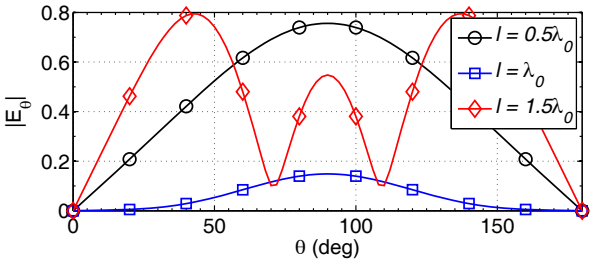

Figure 3.1: Selected basis functions of the dipole from the $\mathcal{F}_\theta^{\text{est}}$ in the $\phi = 90°$ plane. Only 3 CBFPs are shown for clarity and to illustrate pattern variation for different dipole lengths.

The CBFPs in this example are $\mathcal{F}_\theta^{est}$ and $\mathcal{F}_\phi^{est}$ for each point in the estimation set, as explained in Sec. 3.2, and a plot of the CBFPs is shown in Fig. 3.1, revealing a non-smooth variation of the radiation pattern as a function of l and thus making a direct interpolation prone to inaccuracies. However, a smooth variation of the expansion coefficients, as shown in Fig. 3.2, allows an accurate recovery of the full pattern using (3.4).

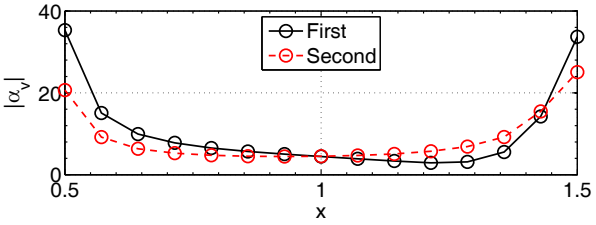

Figure 3.2: Variation of the magnitude of the first two entries of the expansion coefficients as a function of the estimation points. Only two entries are shown for clarity and also because they dominate the remaining entries in terms of magnitude. The markers (○) denote the estimation points.

A comparison between the model and actual radiation pattern is shown in Fig. 3.3 for a few points in the validation set, where the increase in directivity and side lobe levels can be clearly seen as the length of the dipole increases. A cubic spline is used as the interpolation kernel. The maximum magnitude and phase modelling errors in Fig. 3.3 are $\varepsilon^M = 2.6 \times 10^{-3}$ V/m and $\varepsilon^\Phi = 0.011$ radians respectively. Note that the proposed model has only 15 solvable parameters compared to 56 parameters required for the example in [8], thus demonstrating the compactness of the proposed pattern model. A comparison with the technique in [15], with Legendre

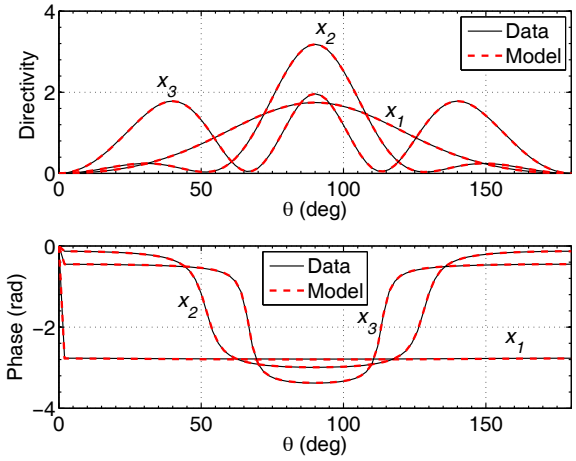

Figure 3.3: Directivity variation (top panel) and phase variation (bottom panel) of the corresponding radiated co-polarised electric field, in the $\phi = 90°$ plane, for different points in the validation set, with dipole lengths $x_1 = 0.625\lambda_0, x_2 = 1.225\lambda_0$ and $x_3 = 1.425\lambda_0$. The patterns are modelled at $f_0 = 842.86$ MHz.

functions and high order polynomials being used as the parameter-dependent fitting functions, yields similar results to the proposed method at low frequencies (< 900 MHz). The results obtained with the method in [15] are less accurate at higher frequencies as shown in Fig. 3.4. Indeed, Fig. 3.4 demonstrates the robustness of our method, with respect to [15], when there is a large dynamic variation in the angular-dependent basis functions (CBFPs). Moreover, with the approach in [15] it can be observed, in Fig. 3.4, that more accurate results are obtained when using a high order polynomial as a fitting function compared to the case where Legendre fitting functions are used. This confirms the strong dependence, of the method in [15], on the choice of the fitting function. It is difficult to select the best fitting function beforehand.

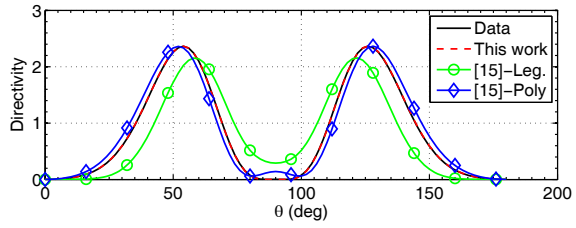

Figure 3.4: Comparison of the modelling capabilities of the proposed approach and the method in [15], with two different choices of parameter-dependent functions namely: Legendre (Leg.) and polynomial (Poly) functions. The patterns are shown in the $\phi = 90°$ plane, at a frequency of 1.06 GHz.

The modelling of the associated reflection coefficients is achieved with root macromodels (see Sec. 3.3) of order 5, and the interpolation kernel is also a cubic spline function. Highly accurate modelling results are shown in Fig. 3.5, where the effects of increasing the length of the dipole can be clearly seen.

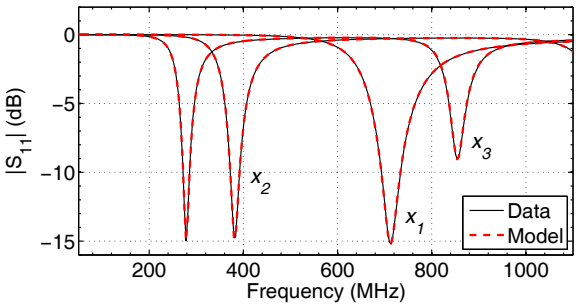

Figure 3.5: Reflection coefficients at selected points in the validation set: $x_1 = 0.575\lambda_0, x_2 = 1.075\lambda_0$ and $x_3 = 1.475\lambda_0$. The appearance of a second resonant frequency within the simulated bandwidth can be seen as the length of the dipole increases beyond a wavelength.

The modeling error (3.21) for the entire radiation pattern, evaluated for frequencies in the range $[50, 1100]$ MHz, is 0.1109 while the error for reflection coefficients is 9.4×10^{-3}.

3.5.2 Axially Corrugated Choke Horn Antenna

An axially corrugated horn antenna with three chokes is modelled in this example. The antenna is depicted in Fig. 3.6 and the design variables are listed in Table 3.1, where a_c is the complement of the horn's flare angle and d_c is the diameter of the input waveguide. The width and depth of the corrugations are fixed at $0.120\lambda_0$ and $0.273\lambda_0$ respectively, where λ_0 is the wavelength at $f_0 = 1.5$ GHz. The thickness of each ridge is fixed at $0.024\lambda_0$.

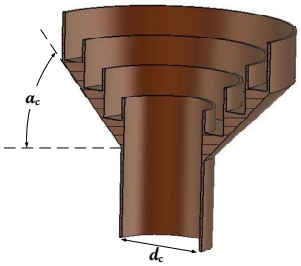

Figure 3.6: Simulation model of an axially corrugated choke horn.

Table 3.1: Design parameters of the choke horn antenna.

Parameter	Min.	Max.
a_c	$0°$	$50°$
d_c	$0.9\lambda_0$	λ_0
Frequency	$0.867f_0$	$1.167f_0$

The estimation grid consists of a 6×6 grid of uniformly sampled points (a_c, d_c) in the range specified in Table 2.1 and the validation samples consist of a 5×5 grid

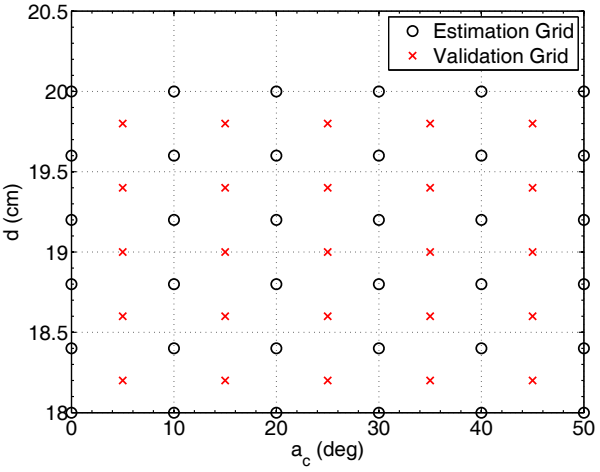

Figure 3.7: Estimation and validation grids.

of points defined as shown in Fig. 3.7. The horn is simulated with the time domain solver in CST Microwave Studio (CST-MWS) [53] and the variation of CBFPs is shown in Fig. 3.8.

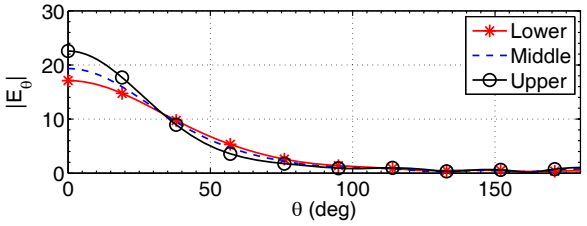

Figure 3.8: Selected basis functions from the $\mathcal{F}_{\theta}^{est}$ set in the $\phi = 90°$ plane. Only 3 basis functions (at the lower $(0°, 0.9\lambda_0)$ and upper $(50°, \lambda_0)$ corners as well as the middle $(20°, 0.96\lambda_0)$ of the design space) are shown for clarity.

The parametric model is constructed as detailed in Sec. 3.2 and a piecewise linear function is used as the interpolation kernel. The model is the evaluated at points in the validation sets and selected results are shown in Fig. 3.9 (with $\varepsilon^M = 0.1049$ and $\varepsilon^{\Phi} = 0.0347$) where the effect of increasing the flare angle's complement, a_c, can clearly be observed.

The maximum modelling error at the validation points is 0.29 and 0.1276 for magnitude and phase respectively. The variation of the modelling error as function of the design variables is shown in Fig. 3.10. The error plots reveal more dynamic variations of the radiation pattern with respect to the flare angle. However, the trajectories of the CBFP expansion coefficients are continuous across the design space such that the resulting model is accurate over the whole design space. This example validates the proposed pattern modelling algorithm even in the case of a large non-linear variation of the radiation patterns within the design space.

Modelling of the corresponding reflection coefficients requires a local approach as the frequency behaviour is different, in terms of the presence of resonances and

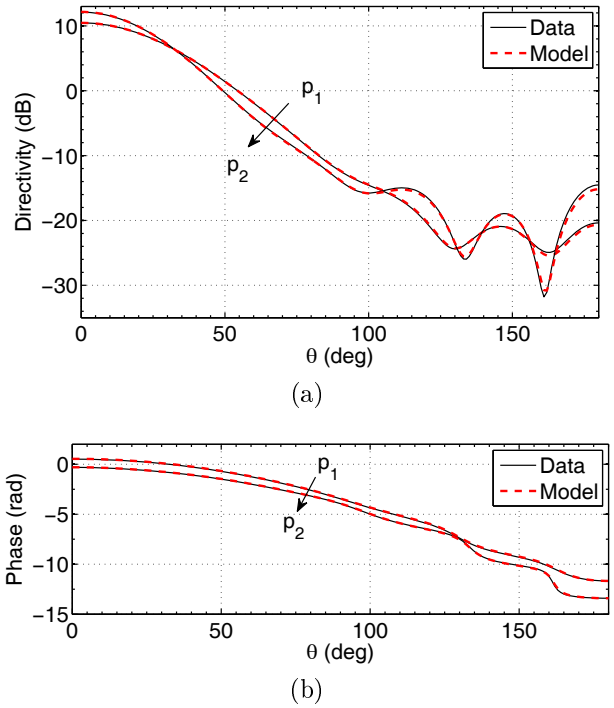

Figure 3.9: (a) Directivity variation, (b) Phase variation across the design space for a fixed $d_c = 19.8$ cm while a_c varies from p_1 to p_2 as $a_c = 5°$ and $a_c = 45°$ respectively. The patterns are evaluated at 1.3 GHz, in the $\phi = 90°$ plane and the increase in directivity is clear as the flare angle decreases.

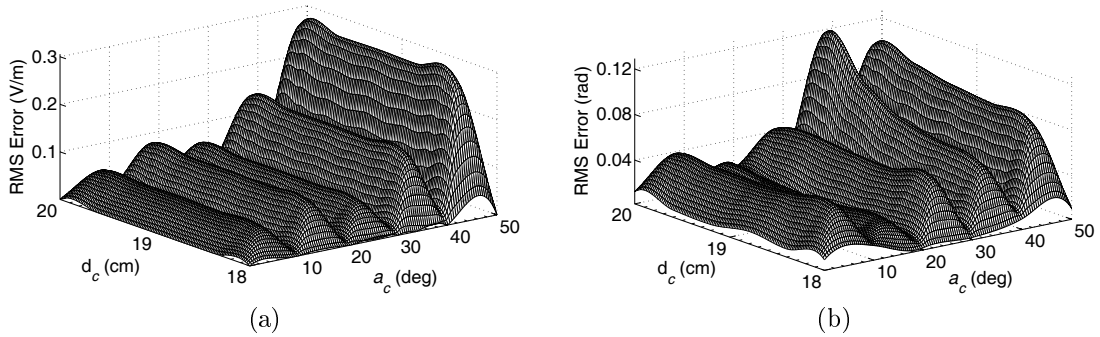

Figure 3.10: Radiation pattern modelling: (a) Magnitude modelling error, (b) phase modelling error over the design space, at 1.75 GHz, where maximum errors occur.

the general trend, in different regions of the design space (i.e., the trajectories of the state-space matrices are not smooth across such a large design space). Therefore, different fitting orders are used in different regions of the design space, with the number of poles varying from 5 to 8, in order to yield relatively accurate results. The fitting orders were automatically determined by iteratively fitting S-parameter data with rational functions of increasing order until an accuracy of -60 dB is reached. A more dynamic variation of reflection coefficients as a function of the flare angle is observed in this example, and therefore the design space is divided in regions according to flare angle values, and each region is fitted with the appropriate number of poles. The variation of the modelling error in the design space is shown

in Fig. 3.11 and a plot of the model with maximum error is shown in Fig. 3.12.

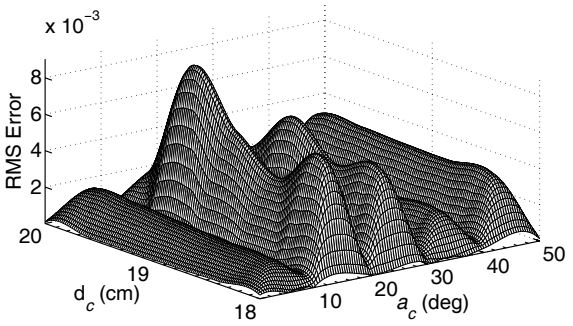

Figure 3.11: S-parameter modeling error over the design space.

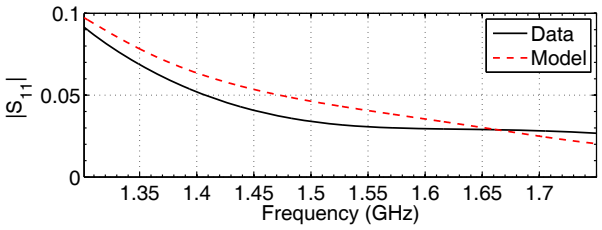

Figure 3.12: Comparison between data and model at the point in the validation set with maximum error.

3.5.3 Convergence Study of the CBFP Models

In this section, we present some results concerning the accuracy of the CBFP models as a function of the number of points in the estimation set. To this end, we consider the example in Sec. 3.5.2 and both regular and scattered grids are considered. For the scattered grid case, estimation points are selected upfront and adaptively according to a design space filling rule such that the design space coverage is maximised.

Models constructed with different numbers of estimation points are evaluated on a dense 9×9 grid of validation points and the results are presented in Table 3.2, where a spline and linear interpolation kernels are used for regular and scattered grids respectively.

The results in Table 3.2 generally reveal lower modelling errors for scattered grids compared to regular grids with a similar number of points. Furthermore, a monotonic decline in modelling errors is observed as the number of estimation points increases, with steady-state values occurring at around 36 estimation points. The slightly higher error for the case of 49 estimation points, in a regular grid, is due to Runge effects at the edge of the design space.

Table 3.2: Pattern modelling mean RMS errors over all validation points as the number of estimation points increases for both regular and scattered grids.

Scattered Grid			Regular Grid		
Points	Magnitude	Phase	Points	Magnitude	Phase
13	0.0553	0.1189	16	0.1214	0.1389
25	0.0360	0.0950	25	0.0972	0.0999
34	0.0271	0.0766	36	0.0101	0.0265
48	0.0244	0.0691	49	0.0441	0.0571

Table 3.2 generally shows a higher modelling error of phase compared to magnitude. This is because a larger number of estimation points are required to capture rapid phase variations for accuracy levels similar to the magnitude errors in Table 3.2. This is illustrated in Fig. 3.2 where it may be inferred that fewer estimation points can be used due to the almost constant values of the magnitudes of expansion coefficients between $x \approx 0.7$ and $x \approx 1.3$. However, all 15 points were required to accurately capture the phase variations shown in Fig. 3.3. Thus, for applications where only magnitudes of the radiated far-field are of interest, accurate models can be achieved with a smaller estimation set.

3.6 Conclusion

This chapter presented a novel algorithm to efficiently model the full radiation pattern of an antenna as a function of its geometry. The proposed method models radiation patterns as a linear combination of CBFPs, where the expansion coefficients are parametrised with respect to multiple design variables. Accurate models are constructed from a limited set of EM simulations and can be used to efficiently carry out antenna design activities where multiple simulations are required. Numerical simulations confirm the accuracy of the proposed method for different antennas.

The proposed method relies on a preassigned number and distribution of samples in the geometry space. It was shown that including more samples generally improves the accuracy of the model until some level of convergence is achieved. The current formulation does not provide any information on the number or distribution of samples required to guarantee a certain level of model accuracy, and this issue is addressed in the following chapter.

The work presented in this chapter was published in an international journal, namely, the IEEE Transactions on Antennas and Propagation as a full paper [31].

Chapter 4

Adaptive Sampling Algorithms

In Chapter 3, a method to obtain accurate radiation patterns as a function of multiple design parameters was proposed. The proposed technique relied on a predefined (regular or scattered) grid of estimation points and therefore its accuracy can only be determined after model building. The model proposed in Chapter 3 requires some *a priori* knowledge of the antenna's dynamic behaviour as a number of estimation points need to be allocated in a region of fast variation to enhance accuracy, as discussed in Sec. 3.5.3. The performance of the algorithm is not guaranteed if executed "blind", unless a sufficiently large number of estimation points is used (this may be inefficient as it might result in over-sampling).

Furthermore, the models in Chapter 3 are built on a frequency by frequency basis, i.e., all estimation grids have to be simulated at every frequency of interest. For a wideband antenna, this process might be computationally very expensive due to the typically large computational cost per simulation.

This Chapter presents adaptive sampling algorithms that allow the technique in Chapter 3 to be used "blind" by sequentially selecting estimation points. Two algorithms are proposed: a univariate *adaptive frequency sampling* (AFS) algorithm and a general *multivariate adaptive sampling* (MAS) algorithm. Both algorithms use the principle of reflective exploration [24] and have the added benefit of having a fully controllable error. The proposed methods are described in subsequent sections.

4.1 Adaptive Frequency Sampling

Modern antenna design is carried out by means of computational electromagnetic (CEM) simulation software based on frequency-domain techniques including, but not limited to, the Method of Moments (MoM), Physical Optics (PO) or on time-domain techniques such as the finite difference time domain (FDTD) method. A non-exhaustive list of commercial EM simulators includes [52–54].

Time-domain simulators have the advantage of producing data with a high spec-

tral content in a single simulation run. A drawback of frequency-domain methods is that the computational cost of simulations increases drastically if a large number of frequency points is considered. This is due to the fact that surface current computations are repeated for each frequency point. This is of particular concern for the design of wideband antennas as it requires the knowledge of the full radiation pattern (or figures of merit derived from the pattern) as well as scattering parameters (S-parameters) or admittance parameters over a wide frequency bandwidth.

To reduce the frequency domain simulation cost for S-parameters, several adaptive sampling algorithms [21,26,27,29,55] do exist to obtain accurate S-parameters, using a few frequency points, over a wide bandwidth. Concerning radiation patterns, some techniques exist to efficiently interpolate the radiation pattern in frequency [8, 10]. While [8, 10] improve the computational efficiency of evaluating radiation patterns in the frequency domain, they require human intervention as the support points (of the interpolant) are selected experimentally, making it difficult to include these methods in an optimization procedure as the "optimal" location and number of support points may vary as the design evolves.

Fig. 4.1 shows the variation of radiation patterns of a horn antenna (shown in Fig. 4.3) as frequency increases. It is apparent that there exists a trend or similarity in the radiation patterns such that the radiation pattern at intermediate frequencies may be obtained using the knowledge of the pattern at only a few frequency points.

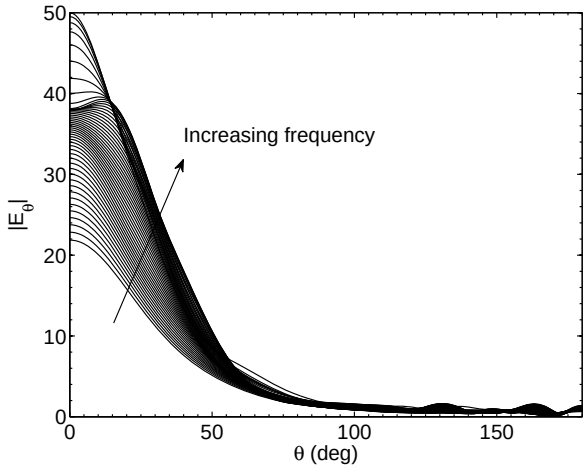

Figure 4.1: Variation of the $\theta-$component of the radiation pattern of a horn antenna as frequency varies from $1 - 1.75$ GHz, in the $\phi = 90°$ plane.

For a given bandwidth, there exists a set of frequency points which yield radiation patterns that form basis vectors that span the subspace of all radiation patterns, such that the radiation pattern at any frequency within a bandwidth of interest, may be obtained as a linear combination of the basis vectors (CBFPs).

The question at hand is how to choose the set of N frequency points where the basis functions are calculated (i.e., the interpolation support points) in the most efficient manner.

This section presents an adaptive frequency sampling algorithm to obtain the full radiation pattern of an antenna over a wide bandwidth. The pattern is modelled as a linear combination of CBFPs, where the expansion coefficients are parametrised with respect to frequency. The parametrised expansion coefficients are then interpolated to give the full pattern at any frequency within the bandwidth of interest. The algorithm selects support points adaptively, using two Kriging [56] interpolants (other interpolants may also be used) of different complexities as the reflective functions, such that a set of linearly independent (not in a strict sense) CBFPs is obtained. In this context, linear independence is achieved if the ratio of the smallest to the largest singular value, of a column-stacked matrix of CBFPs, is below a certain value ε and the difference between the two Kriging functions is smaller than a certain threshold Δ. The values of ε and Δ thus serve as absolute error control measures of the approximation, as they can be used to trade complexity (number of frequency samples) for modelling accuracy. The method can thus be used to greatly improve the efficiency of frequency-domain antenna simulations, as it requires only the knowledge of the radiation pattern at a few frequency points in order to accurately predict the pattern over a large frequency bandwidth, dramatically reducing simulation cost. The technique is described in subsequent sections.

4.1.1 Reflective Exploration

Reflective exploration is a popular technique employed in many adaptive sampling algorithms [24, 26, 29, 55]. It involves two models, called *reflective functions*, of a given response (e.g., S-parameters), where one model, $\mathcal{M}_h$, is considered to be of high accuracy while the second model, $\mathcal{M}_l$, is of lower accuracy. For instance, in [26], the reflective functions to model S-parameters are rational functions of different orders, whereas, in [29], the reflective functions $\mathcal{M}_h$ and $\mathcal{M}_l$ are mathematically similar. However, they are selected such that $\mathcal{M}_h$ is built using N simulation data points while $\mathcal{M}_l$ is built using $N-1$ data points (i.e., $\mathcal{M}_h$ contains additional information about the problem).

New sample points are selected where $|\mathcal{M}_h - \mathcal{M}_l|$ is maximum and this process is repeated iteratively till $|\mathcal{M}_h - \mathcal{M}_l| < \Delta$, where Δ is a prescribed threshold. Note that the convergence criterion of the basic reflective exploration approach (i.e., $|\mathcal{M}_h - \mathcal{M}_l| < \Delta$) may be extended to include physical consistency measures such as passivity [26] or it may be combined with a binary search method to further enhance accuracy, as is done in [24].

In the next section we apply the reflective exploration paradigm to the adaptive

frequency sampling of radiation patterns by constructing reflective functions on the expansion coefficients of CBFPs, coupled with a new stopping criterion that ensures convergence to an accurate model. This is presented in what follows.

4.1.2 Sampling Algorithm

The aim of the algorithm is to generate a minimum number of CBFPs, at near optimal locations (frequency points), such that the antenna's radiation pattern can be accurately determined at any frequency, within a specified bandwidth, as a linear combination of the CBFPs.

Given N CBFPs, obtained from simulated radiation patterns at N frequency points, an $N_R \times N$ matrix of expansion coefficients, $\mathbf{W}$, is obtained by sampling each of the N CBFPs at N_R distinct points, Ω_R, as

$$\mathbf{W} = [\boldsymbol{w}(s_1), \boldsymbol{w}(s_2), \cdots, \boldsymbol{w}(s_N)], \tag{4.1}$$

where $\boldsymbol{w}(s_k) = [w_1, w_2, \cdots, w_{N_R}]^T$ is a column vector of expansion coefficients corresponding to the solution for the k^{th} basis function (i.e., pattern at a frequency s_k). The vector $\boldsymbol{w}(s_k)$, in (4.1), is obtained similarly to (2.8) and (3.3) as

$$\boldsymbol{w}(s_k) = [\mathbf{U}_{\mathrm{R}}(\Omega_R)]^{\dagger} \boldsymbol{f}_k(\Omega_R), \tag{4.2}$$

where $\mathbf{U}_{\mathrm{R}}$ is the left-singular matrix of the SVD realisation of a column-stacked matrix of the CBFPs, $\boldsymbol{w}(s_k)$ is a unique non-zero vector and $\boldsymbol{f}_k$ is the simulated radiation pattern at a frequency s_k.

The method begins by simulating the antenna at a few frequency points in order to obtain the initial set of CBFPs. Reflective exploration is then applied on the expansion coefficients of the CBFPs until the ratio of the minimum to maximum singular values of the matrix of CBFPs decreases below a user specified value, ε. The method is described as follows:

1. The antenna is simulated at $P \geqslant 3$ equispaced frequency points and the CBFPs are stored in a column-stacked matrix, $\mathbf{F}_{\mathrm{M}}$.

2. The ratio, $\frac{\sigma_{min}}{\sigma_{max}}$, of the smallest to the largest singular value of $\mathbf{F}_{\mathrm{M}}$ is computed. If $\frac{\sigma_{min}}{\sigma_{max}} < \varepsilon$, the adaptive sampling loop is terminated and Step 6 is executed. Otherwise, the expansion coefficients are computed using (4.2) and collected in a matrix as in (4.1).

3. Two Kriging models, of different complexity, are built for each of the first two rows of (4.1) (i.e., $e_1 = [w_1(s_1), \cdots, w_1(s_N)]$ and $e_2 = [w_2(s_1), \cdots, w_2(s_N)]$), which consist of the two dominating entries, in terms of magnitude, of the computed vectors in (4.2). The high complexity model, $\mathcal{M}_h : \mathbb{R} \to \mathbb{R}$, has

one extra data point, which is the latest simulated frequency point s_k and the top two entries of its associated expansion vector $\boldsymbol{w}(s_k)$, whereas the low complexity model, $\mathcal{M}_l : \mathbb{R} \to \mathbb{R}$, consists of all previous data points. The Kriging models are thus used as reflective functions herein and they are built using the popular and open source DACE toolbox [57].

4. $\mathcal{M}_h$ and $\mathcal{M}_l$ are compared across the investigated bandwidth, except for the interval containing the latest simulated frequency point. See Fig. 4.2 for details.

5. A new frequency point is selected where $|\mathcal{M}_h - \mathcal{M}_l|$ is largest for the Kriging models through both e_1 and e_2. The antenna is then simulated at the new frequency and $\mathbf{F}_{\mathrm{M}}$ is updated, and the algorithm is repeated from Step 2.

6. An additional frequency point is selected at the centre of the largest interval of the samples selected in Steps $1-5$. The matrix $\mathbf{F}_{\mathrm{M}}$ is updated, and $\mathcal{M}_h$ and $\mathcal{M}_l$ are calculated as in Step 3. If $|\mathcal{M}_h - \mathcal{M}_l| < \Delta$, through both e_1 and e_2, then the user defined ε was sufficient for convergence. Otherwise, the convergence criterion is updated as $\varepsilon = 0.75\frac{\sigma_{min}}{\sigma_{max}}$ and the algorithm is repeated from Step 2. The symbol Δ is the maximum allowed difference between $\mathcal{M}_h$ and $\mathcal{M}_l$, and is a user defined input to the algorithm.

Note that $\mathcal{M}_h$ and $\mathcal{M}_l$ will, in the first few iterations, vary significantly until close to convergence where the addition of a new point does not significantly alter the Kriging functions (i.e., $|\mathcal{M}_h - \mathcal{M}_l|$ is small. see Fig. 4.2). This can be explained by the fact that, in the initial iterations of the algorithm, there are too few basis functions to span the whole subspace, resulting in a substantial changes in the singular values of $\mathbf{F}_{\mathrm{M}}$ with the addition of each new basis function.

Some steps of the proposed adaptive sampling algorithm are elaborated upon in what follows:

i) The Kriging functions are constructed for the top two entries of the columns of (4.1). The variation of these two entries is related to the dynamical behaviour of the radiation pattern (e.g., the variation of e_1 is closely correlated with the antenna's peak directivity as a function of frequency). Furthermore, the accuracy of the predicted radiation pattern is very sensitive to large deviations from the nominal values of w_1 and w_2. Hence the need for the reflective functions to model both e_1 and e_2.

ii) The interval containing the latest simulation point is ignored in Step 4, of the algorithm, because $\mathcal{M}_l$ has no information in that interval. Without this measure, the maximum of $|\mathcal{M}_h - \mathcal{M}_l|$ may occur at the (already simulated) latest point and the iterative algorithm would stall.

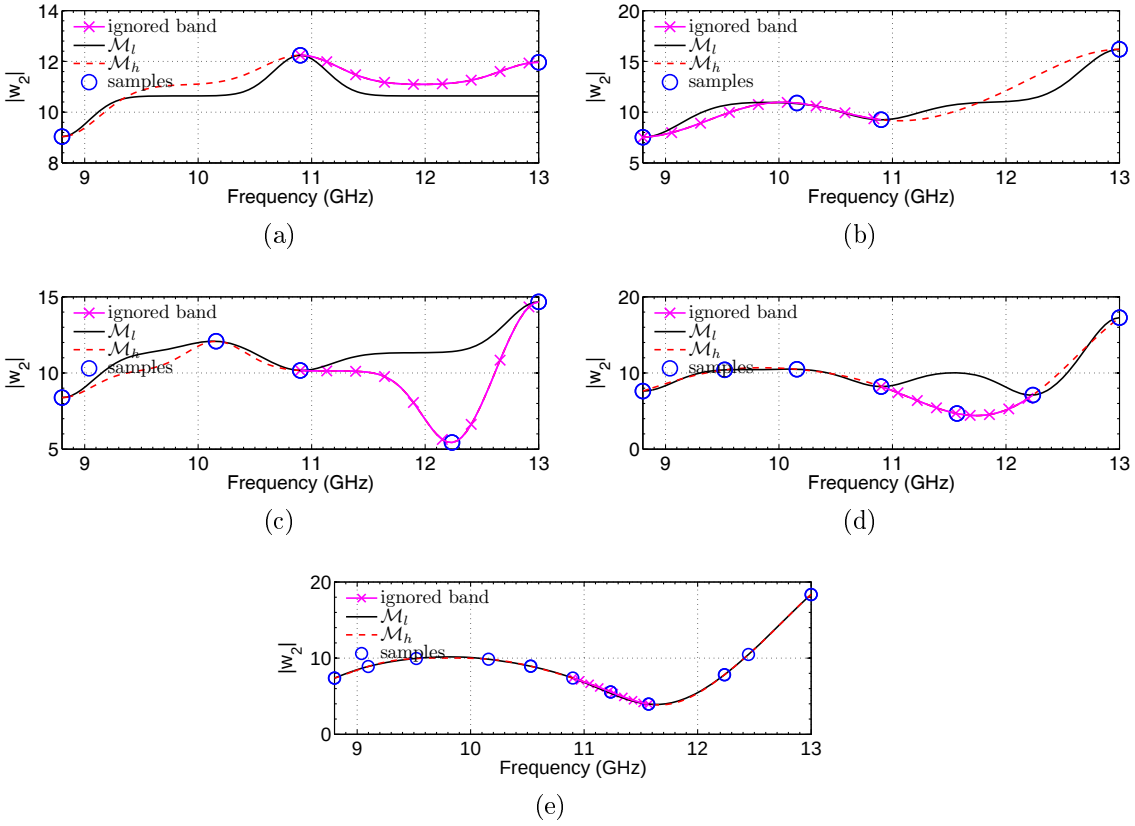

Figure 4.2: Kriging interpolants through the expansion coefficients of CBFPs, e_2 (described in Step 3), for different iterations of the algorithm: (a)-(d) correspond to Iteration #1 through Iteration #4. The ignored frequency band, containing the latest simulated frequency point, is also shown. These plots are for the horn example described in Sec. 2.3 where $\varepsilon = 10^{-4}$ and $\Delta = 0.2$. Note that (d) shows the convergence check of the algorithm (Step 6) which is executed after the user defined $\varepsilon = 10^{-4}$ is reached after Iteration #3. The algorithm carries on as $|\mathcal{M}_h - \mathcal{M}_\ell| > \Delta$ as clearly shown in (d). The outcome of the algorithm, upon convergence, is shown in (e).

iii) Step 6 of the algorithm has a dual purpose. Firstly, it serves as a validation check to confirm whether the variation in the magnitude of expansion coefficients is insignificant upon the addition of a new sample drawn from the largest unexplored frequency interval. Secondly, it serves as a self-correcting measure to ensure the algorithm's convergence even when the convergence criterion ε is poorly chosen. This step provides some robustness to the method and enhances the reliability of the algorithm in a completely unsupervised setting such as optimisation.

4.1.3 Parametrisation of Expansion Coefficients

Once the AFS algorithm has converged, (4.2) is executed on the obtained CBFPs and the resulting expansion coefficients are collected, column-wise, in a matrix as in (4.1). The parametrisation of the expansion coefficients may then, in general, be achieved by interpolating the columns of $\mathbf{W}$, in frequency, using positive interpo-

lation kernels and expressing the CBFP expansion coefficients as [31]

$$\boldsymbol{\alpha}_v(s) = \sum_{k=1}^{N} \boldsymbol{T}_{s_k} \ell_k(s), \tag{4.3}$$

where s is the desired frequency at which the radiation pattern is to be evaluated, while the symbol $\boldsymbol{T}_{s_k}$ represents the known interpolation nodes given by (4.1) and $\ell_k(s)$ is a positive scalar function [31]. However, for a one dimensional problem, as is the case in this section, a more robust parametrisation may be accomplished by expressing $\boldsymbol{\alpha}_v(s)$ as a rational function in an orthogonal basis as

$$\boldsymbol{\alpha}_v(s) = \frac{\sum_{v=1}^{V} \boldsymbol{n}_v \mathcal{C}_v(s)}{\sum_{q=1}^{Q} \boldsymbol{d}_q \mathcal{C}_q(s)}, \tag{4.4}$$

where V and Q are the orders of the numerator and denominator respectively, and the coefficients $\boldsymbol{n}_v$ and $\boldsymbol{d}_q$ are obtained by fitting the right hand side of (4.4) on $\boldsymbol{T}_{s_k}$. $\mathcal{C}_k(s)$ is the k^{th} Chebyshev polynomial of the first kind.

Pertinent numerical examples are presented in the next section to validate the proposed algorithm.

4.1.4 Numerical Examples

Two examples are provided herein involving a horn antenna with a slowly varying radiation pattern as a function frequency, and a sinuous antenna with a more dynamic radiation pattern.

Corrugated Horn

A corrugated horn, operating over a relative bandwidth of 1.5 : 1, is used to illustrate the effectiveness of the proposed algorithm. The horn, shown in Fig. 4.3, is simulated over a bandwidth $f \in [8.8, 13]$ GHz.

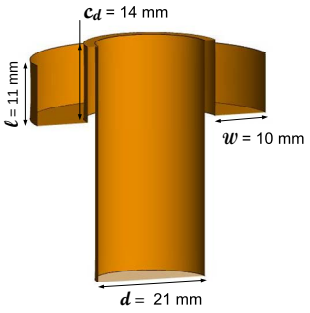

Figure 4.3: Model of the used corrugated horn, with one corrugation. The length of the circular waveguide part of the antenna is 44 mm.

The algorithm in Sec. 4.1.2 begins with an initial distribution of $P = 3$ frequency points $f = [8.8, 10.9, 13]$ GHz and adaptively selects 8 other frequency

points $f = [10.16, 12.24, 9.52, 11.57, 12.45, 10.53, 9.10, 11.23]$, as described in Steps $1-6$, resulting in a total of 11 CBFPs.

The relative root mean square error (RRMSE) between the model and validation data samples is chosen to assess modeling accuracy. The RRMSE is defined as

$$E(s) = \sqrt{\frac{\sum_{k=1}^{N_d} \left| G_k(s) - \widetilde{G}_k(s) \right|^2}{\sum_{k=1}^{N_d} |G_k(s)|^2}}, \tag{4.5}$$

where $G_k(s)$ is the validation data and $\widetilde{G}_k(s)$ is the prediction from the model. Note that G_k and $\widetilde{G}_k$ are generic variables that denote either directivity or the phase of the co-polarised electric field. Validation samples are obtained by simulating the horn at 100 equispaced points in $[8.8, 13]$ GHz.

The values of ε and Δ are set to 10^{-4} and 0.2 respectively. However, a convergence value of $\frac{\sigma_{min}}{\sigma_{max}} < \varepsilon$ is reached after 3 iterations of the algorithm, at which point the model fails the validation check (Step 6 of the algorithm), as shown in Fig. 4.2d, and the value of ε is subsequently refined until an accurate model is obtained, as described in Sec. 4.1.2.

The final value of ε is given by 9.2×10^{-8}, demonstrating the robustness of the method with respect to a poor selection of the ε convergence criterion. The choice of Δ is flexible as it can be used in conjunction with ε to trade accuracy for complexity. However a value of $\Delta \geqslant 0.2$ is recommended as a smaller value may result in oversampling.

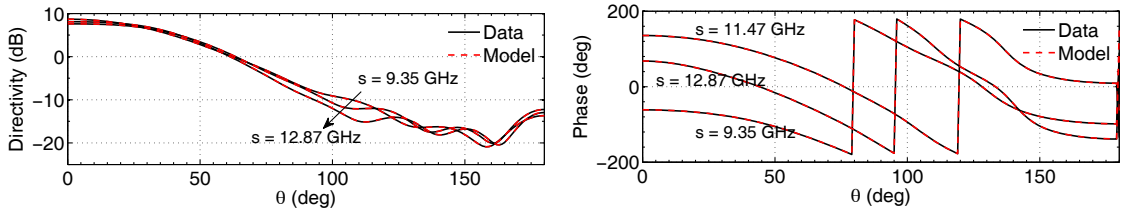

(a) (b)

Figure 4.4: Magnitude and phase plots in the $\phi = 45°$ plane, and at frequencies $s \in \{9.35, 11.47, 12.87\}$ GHz.

The maximum RRMSE for magnitude and phase are 3.17×10^{-4} and 2.22×10^{-2} respectively. A comparison between the pattern obtained from the CBFP model and validation samples is shown in Fig. 4.4, where there's no visible difference between model and validation data, confirming the effectiveness of our proposed approach.

The evolution of the prediction error, through the iterations of the algorithm, is shown in Fig. 4.5a, where the relationship between the value of the convergence criterion, ε, and the model's accuracy can be inferred in Fig. 4.5b. While from a

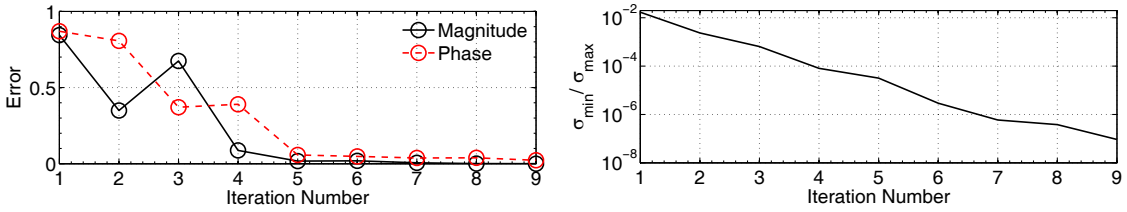

(a) (b)

Figure 4.5: Convergence vs iterations. (a) Maximum magnitude and phase error over 100 validation frequency points, as a function of selected CBFPs through iterations. (b) value of the convergence criterion $\varepsilon = \frac{\sigma_{min}}{\sigma_{max}}$ through iterations. The errors are computed using (4.5). Notice the levelling after 5 iterations with only slight decreases until the final iteration.

magnitude point of view, the error at Iteration 4 leads to fairly accurate results, however, the corresponding error in phase (> 0.03), is equivalent to a phase difference of up to 4° between the model and validation data. Fig. 4.5 illustrates the trade-offs that can be made, with respect to complexity and accuracy of the model, by varying ε.

It is worth noting that the model is built and evaluated in 0.159 s per frequency point, resulting in a speed-up of 154× with respect to the EM simulation which runs at 24.52 s per frequency point on a 64-bit Windows platform with an Intel Core i7 – 2600 CPU at 3.4 GHz and 16 GB of RAM.

Planar Sinuous Antenna

The algorithm in Sec. 4.1.2 is executed on an antenna with a more dynamic variation in the radiation pattern as a function of frequency. For this purpose, a wideband planar sinuous antenna [38] is used. The antenna operates over a bandwidth ratio of 3 : 1, from 2 – 6 GHz, and is shown in Fig. 4.6.

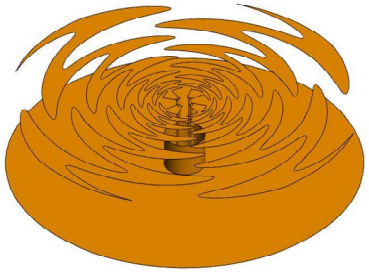

Figure 4.6: Planar sinuous antenna with an angular width of 30°, growth rate of 0.83 and rotation angle of 19°, as well as a height of 21 mm above the circular ground plane.

The proposed algorithm is applied to the antenna starting with $P = 3$ equispaced frequency points, with Δ and ε being set at 0.5 and 10^{-7} respectively for high modelling accuracy. A total of 35 frequency points are selected to meet the convergence requirements (corresponding to an average sampling rate of one point every 117.6 MHz). The dynamic nature of the radiation pattern over frequency

is demonstrated in Fig. 4.8 where the dynamic variation of e_1 over frequency is shown. A strong correlation exists between the trend in Fig. 4.8 and the trend of the antenna's directivity as a function of frequency, as reported in [58].

The dynamic variation of the sinuous antenna's radiation pattern results in the slower convergence rate of the algorithm, i.e., more points are required compared to, for instance, the horn antenna example of the previous section. This can be seen in Fig. 4.7 where there are not only large errors initially, but also, the slope of the SVD spectrum in Fig. 4.7b is not as steep as the one in Fig. 4.5b.

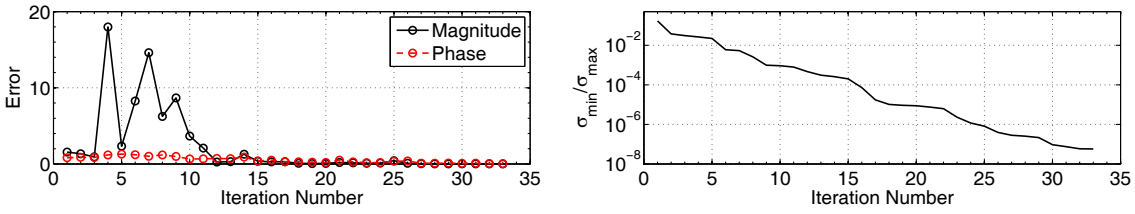

(a) (b)

Figure 4.7: Convergence vs iterations. (a) Maximum magnitude and phase error over 100 validation frequency points, as a function of selected CBFPs through iterations. (b) value of the convergence criterion $\varepsilon = \frac{\sigma_{min}}{\sigma_{max}}$ through iterations. The errors are computed using (4.5). The large magnitude modelling errors at the initial stages of the algorithm are a testament to the dynamic nature of the pattern.

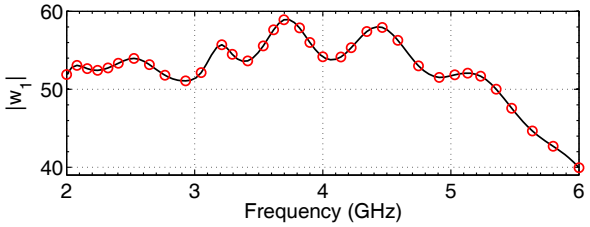

Figure 4.8: Variation of the expansion weights e_1 (see Sec. 4.1.2) as a function of frequency. The solid is a spline interpolant through the points selected by the proposed sampling algorithm. The markers (○) indicate the selected frequency points.

The model is built as described in Sec. 4.1.3 and a validation set of 200 frequency points is used to assess the model's accuracy. A maximum RRMSE of 9.9×10^{-3} and 4.63×10^{-2} are obtained for magnitude and phase respectively.

The model is built and evaluated in 0.64 s per frequency point compared to the 35.65 s for a full-wave EM simulation, resulting in a speed up of 55×.

Fig. 4.9 shows a comparison between the model and validation data at a few frequency points where the highest modeling errors occur, and a good agreement is observed.

The method developed in Sec. 4.1 has been tested on a variety of other (electrically small) antennas (including the pyramidal sinuous antenna, several horns and other log-periodic feeds) with results that are similar to the ones presented in Sec.

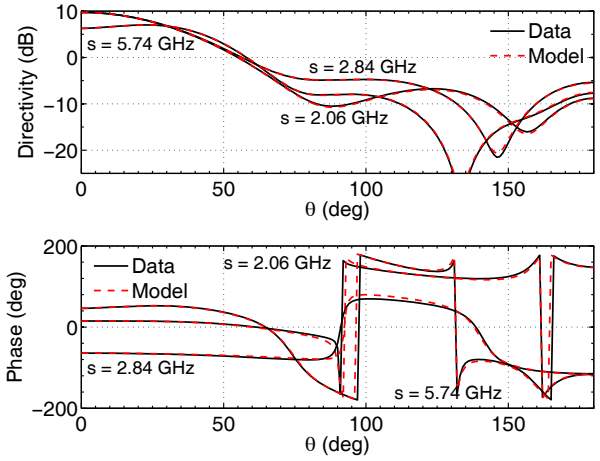

Figure 4.9: Comparison between model and validation data at frequencies where the largest modeling errors occur. The top panel shows directivity plots while the bottom panel shows the phase of the co-polarised electric field, in the $\phi = 90°$ plane.

4.1.4. The black box algorithm developed herein can be used to greatly reduce the computational cost of frequency domain simulations of antennas.

4.1.5 Inclusion of S-parameters – AFS

Herein, we extend the 1-D AFS algorithm of the preceding sub-sections to include the frequency-dependent S-parameters. Note that the reflective exploration framework (see Sec. 4.1.1) within which the AFS algorithm was developed, allows a straight forward extension to include S-parameters. Indeed, ideas from [27] can be readily used in tandem with the algorithm of Sec. 4.1.2, and this is briefly described in what follows.

Define $\mathcal{M}_h^s$ and $\mathcal{M}_l^s$ as reflective functions to model S-parameters, such that $\mathcal{M}_h^s$ has an additional data point (i.e., the latest simulation point) compared to $\mathcal{M}_l^s$, similar to the functions in Sec. 4.1.2. A natural choice for $\mathcal{M}_{\{h,l\}}^s$ is some type of rational function as was done in [26, 27, 29]. Note that, an adaptive frequency sampling algorithm to model impedance characteristics of antennas was presented in [59], where the frequency dependence was modelled as a ratio of two power series polynomials. It was however shown in [60], that the use of power series based rational functions result in a rapid increase in the condition number of the modelling matrix as the number of samples increases. This increase in condition number leads to lower modelling accuracy (sometimes manifested by extra spikes in the response) when compared to cases where better conditioned modelling matrices are used (e.g., VF). We use rational functions, in pole-residue form (leading to a well conditioned modelling matrix), created through the vector fitting (VF) technique [50], as reflective functions for S-parameters.

Having defined the reflective functions, we define the following functions before

defining the ranking criterion

$$\mathcal{Y}_s(f_t) = |\mathcal{M}_h^s - \mathcal{M}_l^s|, \tag{4.6}$$

$$\mathcal{Y}_p(f_t) = \left|\mathcal{M}_h^{(j)} - \mathcal{M}_l^{(j)}\right|, \tag{4.7}$$

$$\mathcal{J}_s(f_t) = \frac{\mathcal{Y}_s(f_t)}{\sum_{t=1}^{T} \mathcal{Y}_s(f_t)}, \tag{4.8}$$

$$\mathcal{J}_p(f_t) = \frac{\mathcal{Y}_p(f_t)}{\sum_{t=1}^{T} \mathcal{Y}_p(f_t)}, \tag{4.9}$$

where f_t denotes a frequency point in a set $\mathcal{S} = \{f_1, f_2, \cdots, f_T\}$ with the property that it contains all frequency points in a given bandwidth except for those in an interval containing the latest simulated point (See Sec. 4.1.2 and Fig. 4.11 for more details). The symbols $\mathcal{Y}_s$ and $\mathcal{Y}_p$ are the differences between the reflective functions of the S-parameters and CBFP expansion coefficients (and hence the radiation pattern), respectively and $j \in \{1, 2\}$ as explained in Sec. 4.2.4. The ranking criterion is then defined as

$$R(f_t) = \mathcal{J}_s(f_t) + \mathcal{J}_p(f_t). \tag{4.10}$$

The criterion in (4.10) consists of two terms that are normalised to be in the range $(0, 1)$ and thus, $\mathcal{J}_s(f_t)$ and $\mathcal{J}_p(f_t)$ have the same meaning in that context. The next frequency point to be simulated is the point $f_t \in \mathcal{S}$ that maximises (4.10).

The algorithm converges when

$$\mathcal{Y}_p(f_t) < \Delta_1 \quad \text{and} \quad \mathcal{Y}_s(f_t) < \Delta_2 \quad \forall f_t \in \mathcal{S}, \tag{4.11}$$

where Δ_1 and Δ_2 are user-defined values that in effect, can be used to control the amount of approximation error the resulting model possesses.

The proposed combined adaptive sampling algorithm inherits the validation check and convergence enforcement measures of the AFS method in Sec. 4.1.2. It is important to note however that fewer points are required to model S-parameters (as opposed to radiation patterns) because the chosen reflective functions are model-based, i.e., $\mathcal{M}_{\{h,l\}}^s$ have a direct physical connection to the nature of S-parameters.

The resulting radiation patterns from simulations at each of the selected frequency points are used to build a pattern model using the CBFP framework (See Sec. 4.1), while S-parameter data, corresponding to selected frequencies, are used to fit a rational function, through the VF method, which is then evaluated at all frequencies within the bandwidth of interest. A pertinent application example is presented in what follows.

Pyramidal Sinuous Antenna

The algorithm of the previous section is applied to efficiently model frequency-dependent radiation patterns and S-parameters of the pyramidal sinuous antenna

shown in Fig. 4.10 (this antenna is a projection of the basic planar antenna in [61] onto a pyramid). The bandwidth of interest is $[2, 6]$ GHz and the convergence criteria are set as $\Delta_1 = 0.5$ and $\Delta_2 = 0.05$. The magnitude of the convergence thresholds is inferred from the expected order of magnitude of the underlying functions being modelled. For the radiation pattern case we expect the most significant expansion coefficients to be in the order of the radiation pattern field strength, and for the reflection coefficient S-parameters we expect the magnitude to be smaller than -10 dB. The commercial code FEKO [52] is used for EM simulations.

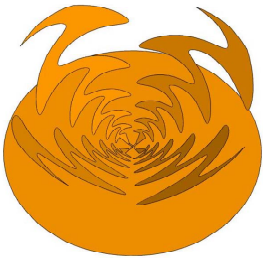

Figure 4.10: Simulation model of the pyramidal sinuous antenna.

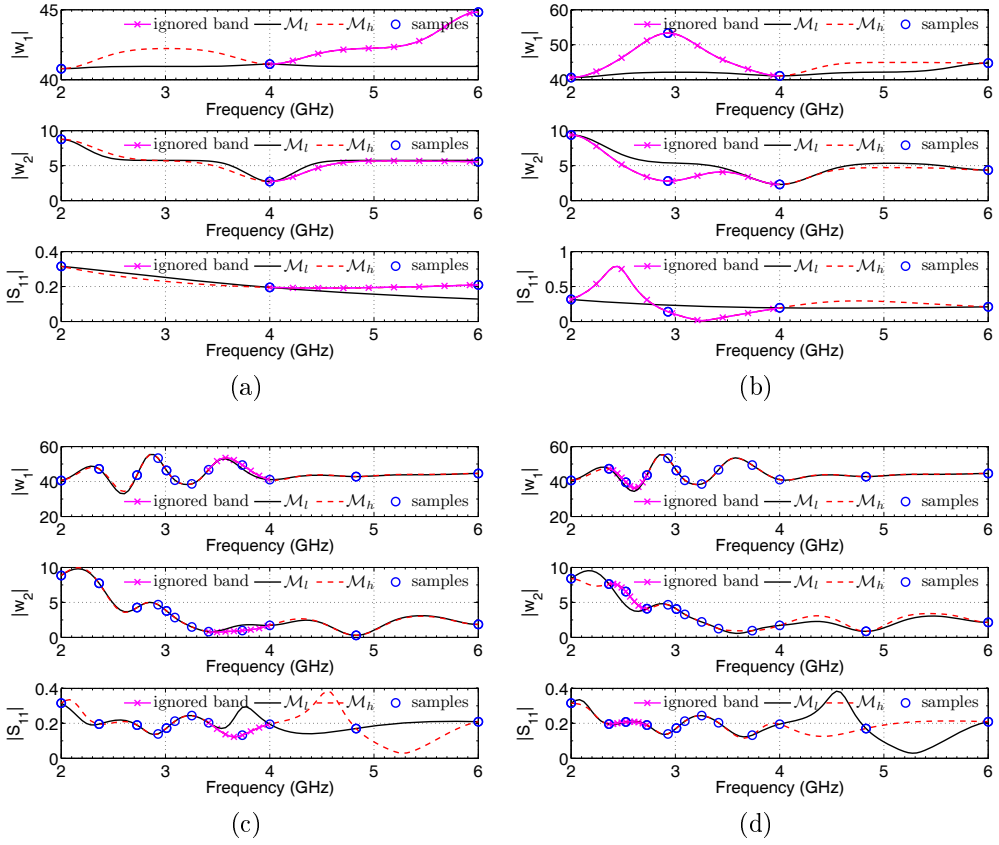

Figure 4.11: Few iterations of the proposed algorithm on the response of a pyramidal sinuous antenna. The top panel in each figure shows the second entry of the expansion coefficients of CBFPs while the bottom panel shows the reflective functions of S-parameters in dB. (a) Iteration #1 . (b) Iteration #2. (c) Iteration #10. (d) Iteration #11.

Similarly to the method in Sec. 4.1.2, the present algorithm begins by simulating the antenna at three equidistant frequency points (the two extremes and the middle frequency), and subsequent frequencies are adaptively selected as described in the fully automated procedure of the previous section. This algorithm also inherits the validation step of the method in Sec. 4.1.2, wherein threshold values are refined if reflective functions do not meet convergence criteria upon adding a new sample in a large unexplored frequency band. A few iterations of the proposed method are shown in Fig. 4.11, where one can observe initial large errors between reflective functions due to an insufficient number of poles and too few basis functions for S-parameters and radiation patterns respectively.

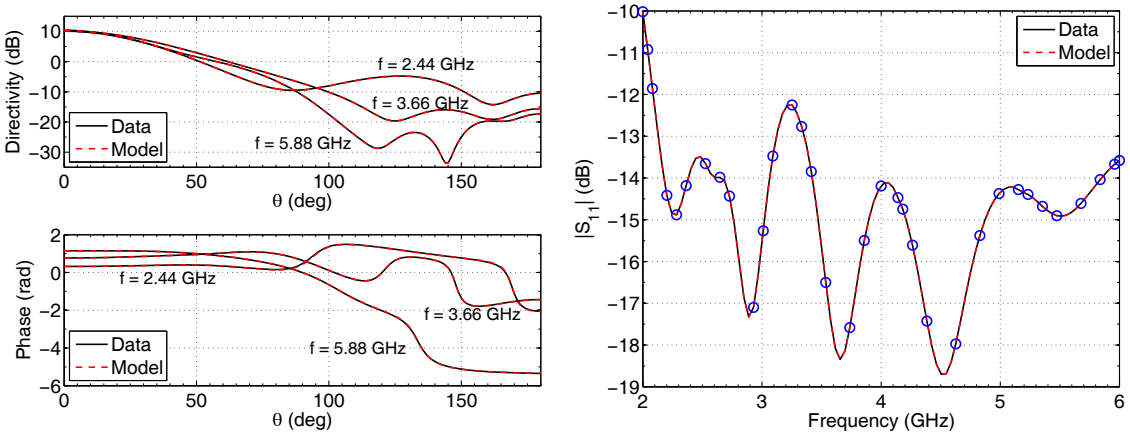

(a) (b)

Figure 4.12: (a) Comparison between data and model of the radiation pattern at selected frequency points in the validation set. (b) S-parameters: data vs. model built using VF through the selected points shown as markers (○).

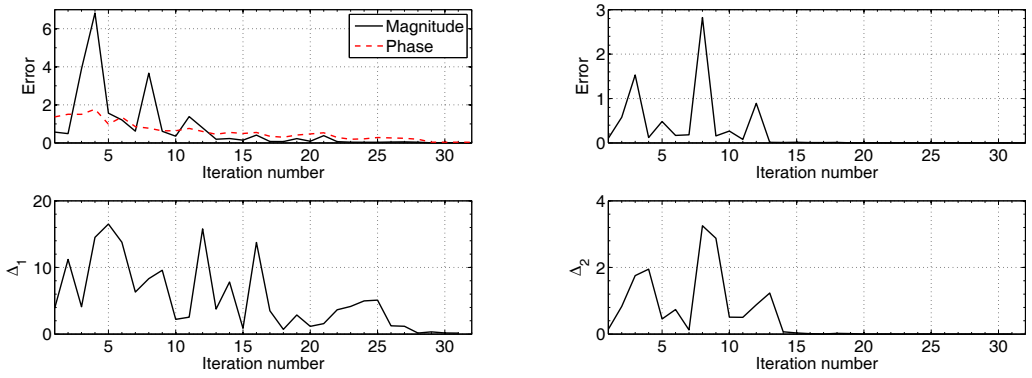

(a) (b)

Figure 4.13: (a) Top panel: pattern approximation error as the algorithm evolves. Bottom panel: Evolution of the pattern convergence threshold Δ_1. (b) Top panel: S-parameter approximation errors. Bottom panel: Variation of convergence threshold Δ_2 through iterations of the algorithm. Notice how well $\Delta_{\{1,2\}}$ track the actual errors, justifying their usage as indicators of convergence.

The algorithm converges after a total of 34 points have been selected and the resulting models have maximum magnitude RRMSE values of 8.07×10^{-5} and 4.2×10^{-3} for the S-parameters and radiation patterns respectively. The corresponding maximum phase error, between the pattern model and validation data, is 3.31×10^{-2}. The evolution of approximation errors is shown in Fig. 4.13 where we make the following observations: (i) the values of Δ_1 and Δ_2 are a good approximation of the actual modelling; (ii) Far fewer points are required to get an accurate S-parameter model compared to the radiation pattern – this stems directly from the fact that the reflective functions used (rational functions) have a direct connection with the physics of S-parameters.

A plot of the radiation patterns, at selected validation points, is shown in Fig. 4.12 where there's no visible difference between model and validation data traces. Similar results were obtained with different types of (electrically small) antennas, including horns.

4.2 Multivariate Adaptive Sampling

Like in many adaptive sampling algorithms, the goal is to select new sample points in potentially interesting regions of the parameter space. This could be regions with perceived rapid variation in the quantity of interest or simply large regions that are yet to be sampled. A multivariate adaptive sampling (MAS) algorithm is generally required to balance between *exploration* (i.e., adding points in large unsampled regions.) and *exploitation* (i.e., adding new points in regions of rapid function variation). These two properties are central to the development of several sequential sampling algorithms that have been used to tackle several important problems in different disciplines [21, 36, 55, 62].

While the previous section dealt with univariate adaptive frequency sampling, the focus of this section is on extending the univariate algorithm to a multivariate setting where the considered variables may be geometrical parameters and frequency. The MAS algorithm developed here is based on the exploitation and exploration features highlighted in the previous paragraph.

4.2.1 Exploration

As stated above, exploration consists of scanning the parameter space to detect regions that have not been sampled. This process is independent of the function (e.g., radiation patterns, scattering parameters, etc...) being modelled, and is only related to the coordinates of the current points in the parameter space.

Consider an N-dimensional parameter space, $\mathcal{P}$, with P sample points

$$\mathcal{X} = \{\boldsymbol{x}_1, \boldsymbol{x}_2, \cdots, \boldsymbol{x}_P\}. \tag{4.12}$$

The region of $\mathcal{P}$ (i.e., the hypervolume[1]) occupied by each point, $\{\boldsymbol{x}_k\}_{k=1}^{P}$, is computed in order to determine sparsely sampled regions. The problem of finding sparsely populated regions was previously encountered when considering 1-D frequency sampling. In that context, the solution is trivial in that one can identify the sizes of the regions between samples by a simple difference operator on the sample positions vector. Extending this idea to higher dimensional spaces requires calculation of the hypervolume occupied by each point. The hypervolume of each point is quantified by means of Voronoi tessellations and this process is described in what follows.

Voronoi Tessellation

A Voronoi tessellation [63] of the parameter space, $\mathcal{P}$, containing the points in (4.12), consists of dividing $\mathcal{P}$ into $\{C_k\}_{k=1}^{P}$ cells, such that each cell C_k is a set of all points that are closer to the point $\boldsymbol{x}_k$ than any other point in $\mathcal{X}$. Formally, each cell is defined as

$$\text{dom}(C_k) = \{\boldsymbol{x} \in \mathbb{R}^N | \delta(\boldsymbol{x}, \boldsymbol{x}_k) \leqslant \delta(\boldsymbol{x}, \boldsymbol{x}_i)\}, \tag{4.13}$$

where $\boldsymbol{x}_i \in \mathcal{X} \setminus \{\boldsymbol{x}_k\}$, $\delta(\cdot, \cdot)$ represents the Euclidean distance between two points and $\text{dom}(C_k)$ is the domain of C_k.

In other words, C_k contains the point $\boldsymbol{x}_k$ and a "ball" around it. The hypervolume, V_k, of the "ball" around $\boldsymbol{x}_k$ is equivalent to the portion of the parameter space occupied by $\boldsymbol{x}_k$. A large V_k implies a sparsely sampled region while a small value indicates a densely sampled region of $\mathcal{P}$. An example of a Voronoi tessellation of a 2-D parameter space is shown in Fig. 4.14.

The value of V_k can be computed exactly for bounded Voronoi diagrams. The cost of exact hypervolume computations does not scale well with the number of samples as well as dimension [64]. However, the cell volume, V_k, can be estimated accurately and cheaply using Monte Carlo simulations [21,36,64]. This approach is well suited for our purposes as it is fast (only involving fast point-wise operations like addition and subtraction) and scales well with the dimension of the parameter space. The cell volume estimation algorithm can be summarised as follows:

1. K points are uniformly randomly generated within the parameter space $\mathcal{P}$. We denote the set of the generated random points as $\mathcal{K}$.

[1] Hypervolume is used herein as a generic term that stands for area in the 2-D case and volume in the 3-D case.

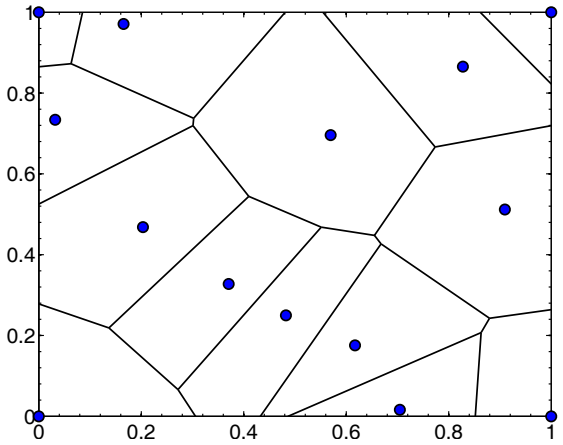

Figure 4.14: Voronoi diagram of a 2-D parameter space. The line segments represent the boundaries of the Voronoi cells, C_k, for each point. The intersections of the line segments are the (well defined) Voronoi vertices. These vertices are important for the MAS algorithm as will be explained later on. The cells at the $x-$ and $y-$limits of the graph are not bounded.

2. Initialize $T_k \leftarrow 0$, where T_k is a counter for the number of points in $\mathcal{K}$ that are closest to $\boldsymbol{x}_k \in \mathcal{X}$, i.e., in the cell C_k.

3. For each point $\boldsymbol{p} \in \mathcal{K}$, compute the Euclidean distance with the points in $\mathcal{X}$ and set $T_k \leftarrow T_k + 1$ if $\boldsymbol{p}$ is closer to $\boldsymbol{x}_k$ than any other point in $\mathcal{X}$.

4. The hypervolume, V_k, of each cell, C_k, is then estimated as $V_k \leftarrow \frac{T_k}{K}$.

The accuracy of the above algorithm (being Monte Carlo based) depends on the number of random samples K. A value of $K = 100P$ was found to yield a sufficiently low error on the estimated hypervolume when compared to exact hypervolume computations [64], and this value is used throughout this chapter.

Cells with large volumes correspond to sparsely sampled regions and they are thus associated with high exploration scores.

4.2.2 Selection of Candidate Points

In any adaptive sampling algorithm a set of candidate points for the following sample must be defined. In low dimensional cases, such as the 1-D case described earlier in the AFS algorithm, this step is almost implicit in the method in that almost any number of candidate points along the frequency axis can be considered. Selection of the next sample requires maximization of some function, like (4.10) in Sec. (4.1.5), and this is normally achieved by simply testing the function value at a large number of discrete points along its argument. When the dimensionality of the parameter space grows, this method becomes increasingly difficult due to the curse of dimensionality, and will eventually become intractable for large spaces that should be "smoothly" evaluated – even when very fast modelling functions are used.

We therefore require a formal description of some finite set of candidate points to consider for the sample to be used in the next iteration.

Given a set of sample points in the parameter space, a Voronoi tessellation is performed and the *Voronoi vertices* (see Fig. 4.14 and Fig. 4.28) are selected as candidate points. We consider Voronoi vertices as the best candidate points for the MAS algorithm as they are a finite set of well-defined points that lie the farthest away from the current sample points, and are thus least influenced by the behaviour of the function at the sample points.

4.2.3 Exploitation

Exploitation is the act of selecting new samples in regions of the parameter space where there are rapid function variations. To detect such regions, we use the principle of reflective exploration as described in Sec. 4.1.1 and demonstrated in Sec. 4.1.2, for the 1-D case. An extension of the reflective exploration idea of Sec. 4.1 to the general N-dimensional (N-D) case is presented in this section.

Consider the set of points in (4.12), with $\boldsymbol{x}_P$ being the point from the latest simulation. Furthermore, consider a set of T candidate points

$$\mathcal{T} = \{\boldsymbol{p}_1, \cdots, \boldsymbol{p}_T\}, \tag{4.14}$$

obtained as described in Sec. 4.2.2. Exploitation is then carried out according to the steps described below:

1. The radiation patterns corresponding to all points in $\mathcal{X}$ are column-stacked in a matrix $\mathbf{F}_{\mathrm{M}}$ and the expansion coefficients are computed and stored according to (4.2) and (4.1)[2].

2. Let e_1 and e_2 denote the first and second rows of the matrix $\mathbf{W}$ in (4.1) (i.e., Vectors of the two dominant entries of the self-expansion coefficients). Let $\mathcal{M}_{\{h,l\}}^{(i)}$ denote a Kriging interpolant with e_i as the output, where $i \in \{1, 2\}$. The most accurate reflective function, $\mathcal{M}_h^{(i)} : \mathbb{R}^N \to \mathbb{R}$, is a Kriging interpolant trained on all points in $\mathcal{X}$. The other reflective function, $\mathcal{M}_l^{(i)} : \mathbb{R}^N \to \mathbb{R}$, is also a Kriging interpolant with training points $\mathcal{X} \setminus \{\boldsymbol{x}_P\}$ (i.e., all points except the most recent sample). In summary, two reflective functions are built for each of the vectors e_1 and e_2.

3. Let $\mathcal{V} \subset \mathcal{T}$ be the set of Voronoi vertices belonging to C_P, the Voronoi cell that has the latest point, $\boldsymbol{x}_P$, as an interior point. The points in $\mathcal{V}$ are closest to $\boldsymbol{x}_P$ and hence are considered to be biased towards $\mathcal{M}_h$, since $\mathcal{M}_l$ has no

[2]Here the symbol s_k that represents frequency in Sec. 4.1.2 is replaced by a generic symbol $\boldsymbol{x}_k$ that represents a vector of geometric variables and frequency.

information in this region. A new set of candidate points is thus obtained as $\mathcal{T}_{new} = \mathcal{T} \setminus \mathcal{V}$. This step is a generalisation from the 1-D case, where points in a segment were ignored (see Sec. 4.1.2), to the N-D case, where points in a hypervolume are ignored.

4. The functions $\mathcal{M}_h^{(i)}$ and $\mathcal{M}_l^{(i)}$ are evaluated on the candidate points in $\mathcal{T}_{new}$ and the difference between the two reflective functions is computed. A region of rapid function variation contains the point in $\mathcal{T}_{new}$ at which $\left|\mathcal{M}_h^{(i)} - \mathcal{M}_l^{(i)}\right|$ is maximum, as an interior point.

The procedure highlighted in the steps above, is used for exploitation purposes for a general N-D parameter space. This procedure differs from the one in Sec. 4.1.2 in the way candidate points are selected: only Voronoi vertices are used instead of all points inside relevant Voronoi cells. In addition to the reasons stated in Sec. 4.2.2, candidate points are selected in this way in order to mitigate possible over-estimation errors that may arise with Kriging at the edges of the parameter space. This is prone to occur in the initial iterations of the sampling algorithm, due to the sparse distribution of samples, and may result in an incorrect bias towards the edges.

Reflective functions are used to determine regions of fast variations, in contrast to the local linear approximation technique used in [21, 36, 62]. The clear advantage of the proposed approach is that the dynamics of the model are taken into account as regions of non-linear variation, that may not be detected by the linear approximation method, are readily handled by the non-linear reflective functions.

4.2.4 Ranking and Sample Selection

Exploitation Score

The exploitation score is computed for each of the candidate point in $\mathcal{T}_{new}$. First, we identify whether the maximum difference $\left|\mathcal{M}_h^{(i)} - \mathcal{M}_l^{(i)}\right|$ occurs for $i = 1$ or $i = 2$, and we denote this value of i as j. Next, we only consider the models $\mathcal{M}_{\{h,l\}}^{(j)}$ and compute a normalised exploitation score for each of the candidate points as

$$Q(\boldsymbol{p}_t) = \frac{\overline{Q}(\boldsymbol{p}_t)}{\sum_{t=1}^{T_{new}} \overline{Q}(\boldsymbol{p}_t)}, \tag{4.15}$$

where $\overline{Q}(\boldsymbol{p}_t) = \left|\mathcal{M}_h^{(j)} - \mathcal{M}_l^{(j)}\right|$, with $\mathcal{M}_{\{h,l\}}^{(j)}$ being Kriging functions evaluated at $\boldsymbol{p}_t$ and $t = \{1, 2, \cdots, T_{new}\}$, with T_{new} being the number of points in $\mathcal{T}_{new}$.

Exploration Score

The exploration score consists of first computing the hypervolume of each candidate point when added to the set of current points in the parameter space (4.12). A

normalised exploration score is then obtained as

$$V(\boldsymbol{p}_t) = \frac{\overline{V}(\boldsymbol{p}_t)}{\sum_{t=1}^{T_{new}} \overline{V}(\boldsymbol{p}_t)}, \tag{4.16}$$

where $\overline{V}(\boldsymbol{p}_t)$ is the hypervolume of the Voronoi cell containing the point $\boldsymbol{p}_t \in \mathcal{T}_{new}$.

Note that the normalisation of the difference between reflective functions in (4.15) as well as the cell volumes in (4.16) serves the purpose of scaling both metrics in the same range of $(0, 1)$. This is especially important in the context of a weighted ranking score discussed in Sec. 4.3.

Furthermore, note that, ideally, (4.16) is computed for each candidate point on the set $\mathcal{X} \cup \{\boldsymbol{p}_t\}$. The implication of this is that a new Voronoi tessellation is computed for each of the considered candidate points. For each of these tessellations, the volume estimate must be computed for each of the candidate points (which will in general be different from that of the original samples). This procedure, from a practical implementation vantage point, becomes an unacceptably slow process as the number of sample points in $\mathcal{X}$ (and hence the number of candidate points) or the problem's dimension increases, sometimes being slower than an EM simulation.

Instead, we propose an approximate method where the cell volumes are computed at once using the set $\mathcal{X} \cup \mathcal{T}_{new}$, which lends itself to a fast implementation, with fast distance computation routines. Moreover, the possible errors, introduced by computing cell volumes in this way[3], especially for very close candidate points, are minimised by the normalisation term in (4.15). Also, very closely spaced candidate points are likely to have similar exploitation scores. The runtime for sequential volume computation as well as our proposed approach, where only one Voronoi tesselation is required which adds all the candidate points to the original sample points, is shown in Fig. 4.15a for varying numbers of candidate points emanating from the 2-D horn problem of Sec. 4.3. A marginal increase in computation time with increasing numbers of samples is observed with our approach whereas an undesirable exponential increase in computing time is observed with the sequential computation method. Sequential volume computation time is even worse for high-dimensional modelling problems as the number candidate points increases linearly (A proof for this statement is given by Euler's formula for connected graphs [63]). Fig. 4.15b shows exploration scores obtained using sequential volume computations as well as using our proposed approach. It is apparent from Fig. 4.15b that the trends of exploration scores are similar in that candidate points with large (or small) exploration scores are accurately captured in both cases. Fortunately, for the MAS algorithm, only a relative exploration score (i.e., the ability to tell whether a candidate point occupies a region that is larger (or smaller) than another candidate point) is required as a selection metric and thus our approach to volume

[3] As opposed to a sequential computation on $\mathcal{X} \cup \{\boldsymbol{p}_t\}$.

computation is valid. It should also be stressed here that the exploration score is only required in the algorithm to identify sparsely sampled regions in the parameter space. Selecting the wrong candidate point in terms of the actual volume occupied by that specific point will not significantly alter the performance of the algorithm as long as the selected point is among the most sparsely spaced ones. This method yields sensible and useful information about the design space exploration. As such, the time benefits clearly outweigh accuracy concerns and thus justifying this design decision.

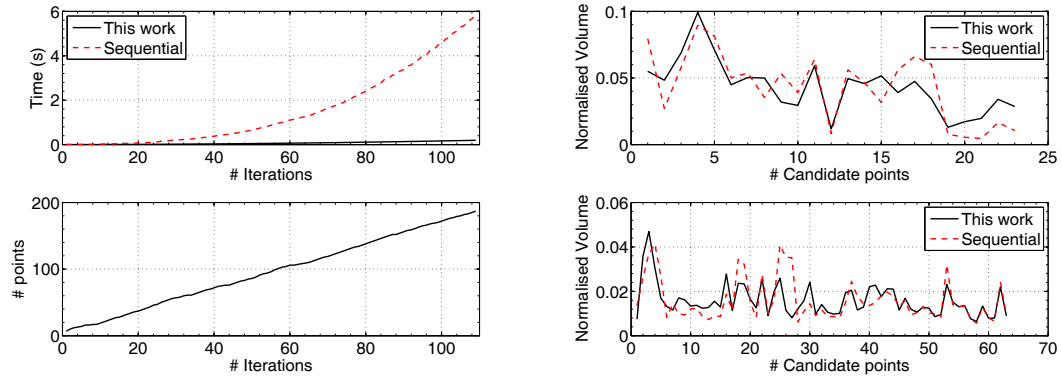

(a) (b)

Figure 4.15: (a) Computation time (top panel) to obtain cell volumes: Sequential vs. our implementation on $\mathcal{X} \cup \mathcal{T}_{new}$. Number of candidate points for each iteration (bottom panel). (b) Comparison of exploration scores, obtained with the computation methods in (a), for different iterations of the MAS algorithm (similar results are obtained for all iterations). These results are obtained from the horn example investigated in Sec. 4.2.6 with equal weighting factors.

In general, one may consider to limit the number of candidate points for high-dimensional design spaces. A procedure to limit this number would be to compute the exploitation score of the candidate points on the set $\mathcal{T}_{new}$ and retaining only the first M points with the highest scores. An exploration score may then be computed for the retained points. This approach is viable since exploitation scores are orders of magnitude faster to evaluate when compared to exploration scores.

Ranking and Selection

Having computed the exploration and exploitation scores, the ranking of candidate points is quantified as

$$R(\boldsymbol{p}_t) = \beta_1 Q(\boldsymbol{p}_t) + \beta_2 V(\boldsymbol{p}_t), \tag{4.17}$$

where $t = \{1, 2, \cdots, T_{new}\}$, and the sample point to be simulated next is the candidate point $\boldsymbol{p}_t$ at which (4.17) is maximum. The simple formulation of the ranking score in (4.17) allows a great deal of flexibility as the same algorithm can be easily biased towards either exploration or exploitation by varying the weighting factors $\beta_{\{1,2\}}$.

Note that both exploration and exploitation scores have normalised values in the range $(0, 1)$ and they thus have the same "meaning" in the context of the ranking score.

The MAS algorithm may then be summarised for an N-D parameter space, with T points, as: (i) Select candidate points; (ii) compute the exploration score; (iii) compute the exploitation score; (iv) compute the ranking score and select the candidate point with maximum ranking score as the next sample to evaluate; and (v) repeat steps (i)–(iv) until a stopping criterion is reached.

As a final note, one can consider the difference between this algorithm and that proposed for AFS. In the 1-D AFS algorithm the exploration step is essentially left as a final error checking mechanism, whereas here it is included explicitly in the ranking score for each iteration. This must be done in high dimensional spaces to avoid situations where the exploitation stagnates and converges in a small sub-region of the design space - a situation which is easily avoided on a line as in AFS.

4.2.5 On the Stopping Criterion of the MAS Algorithm

Theorem 1 *Upon convergence of the MAS algorithm, the addition of an extra data point does not significantly alter the landscape of the function of all expansion coefficients of the CBFPs.*

Proof. Let $\mathbf{F}_{\mathrm{M}}$ be a column-stacked matrix of CBFPs. As a result of the basic formulation in (2.1), the CBFPs are linearly independent vectors that span the set of all radiation patterns $\mathcal{F}$. Therefore, upon convergence, the addition of any radiation pattern vector $\boldsymbol{f}$ to $\mathbf{F}_{\mathrm{M}}$, resulting in a matrix $\mathbf{Z}$, does not increase the rank of the resulting matrix (i.e., $\mathrm{rank}\{\mathbf{Z}\} \not> \mathrm{rank}\{\mathbf{F}_{\mathrm{M}}\}$). In other words, the value of smallest singular value, σ_{min}, of $\mathbf{Z}$ is 0. Since, the expansion coefficients are computed using the left singular matrix, the solutions obtained with $\mathbf{F}_{\mathrm{M}}$ and $\mathbf{Z}$ will be identical. □

The above theorem is theoretically correct. In practice however, the value of σ_{min} is always greater than zero and thus linear independence, of the CBFPs, is considered to be achieved if the difference between the minimum singular values of $\mathbf{F}_{\mathrm{M}}$ and $\mathbf{Z}$ is negligible. The above remark can be justified by observing the singular value spectrum, expressed as the ratio $\delta = \frac{\sigma_{min}}{\sigma_{max}}$, as the number of basis functions increases. Such a singular value spectrum is shown in Fig. 4.16 for a pyramidal sinuous antenna and a horn antenna. An initial sharp decrease in δ is observed for the first iterations, followed by a levelling of the curve at which point, only a marginal decrease is observed as more basis functions are added. From our experiments on various antennas, the SVD spectrum levels off after a value of $\delta = 10^{-10}$ has been reached.

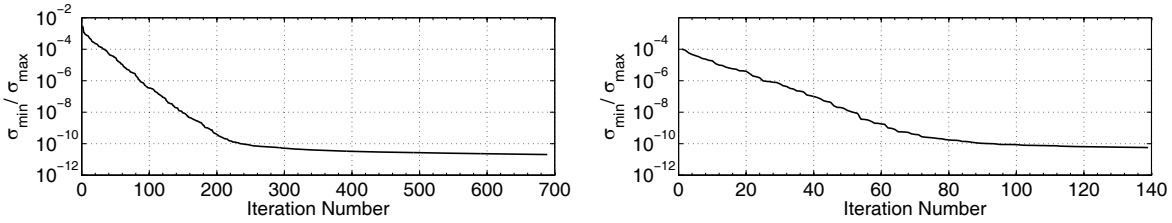

Figure 4.16: SVD spectra for (a) pyramidal sinuous antenna with 4 variable parameters, including frequency. (b) Corrugated horn antenna with 3 variables including frequency.

Having thus obtained linearly independent basis vectors, according to Theorem 1, it only remains to guarantee the accuracy of linear combinations of basis vectors for the MAS algorithm to converge. This is achieved when

$$\mathcal{H}\left\{\max\left\{\left|\mathcal{M}_h^{(i)} - \mathcal{M}_l^{(i)}\right|\right\}\right\} < \lambda \quad \text{for} \quad i \in \{1, 2\}, \tag{4.18}$$

where $\mathcal{H}\{\cdot\}$ is a moving average function, with a window size of about 30, and λ is a pre-set tolerance, i.e., the difference between reflective functions in Sec. 4.2.3.

In summary, the convergence criterion consists of checking whether the δ variation (i.e., the gradient of the SVD spectrum) is minimal, followed by ascertaining that the difference between reflective functions is smaller than a user-defined tolerance, λ (typically a small number). An in-depth discussion of ways of choosing λ is provided in Sec. 4.3. Some conservative values of λ are chosen for the examples in Sec. 4.2.6.

The MAS algorithm allows a user to adaptively generate radiation pattern models of arbitrary accuracy, and is easy to implement as most of the information required (such as Voronoi tessellation data) is readily obtained from native MATLAB functions. The user-defined accuracy parameter, λ, can be used as a measure of absolute error control. The next section presents some pertinent numerical examples to validate the proposed method.

4.2.6 Numerical Examples I

Three illustrative examples are presented in this section. The first involves a horn antenna operating near the cut-off frequency of its input waveguide. The other two examples involve high dimensional ($\geqslant 4$) parameter spaces.

The RRMSE, in (4.5), between the model and validation data samples is used to assess modelling accuracy.

Note that a low-rank approximation of the left-singular matrix of the full CBFP matrix ($\mathbf{F}_{\mathrm{M}}$), obtained upon completion of the MAS algorithm, is used to build the parametric model of the radiation pattern. This is achieved by firstly computing the economy size SVD of $\mathbf{F}_{\mathrm{M}}$ and then only retaining a few singular values and

their corresponding left- and right-singular vectors. The low-rank approximation is necessary for the following reasons: (i) most of the structure of $\mathbf{F}_{\mathrm{M}}$ can be captured using a few singular values (i.e., the singular values spectrum is rapidly decreasing); (ii) errors arising as a result of interpolating/fitting very small values are avoided; (iii) the time it takes to build a model is significantly reduced.

1. Horn Near Cut-Off

A horn, similar to the one in Fig. 3.6, is investigated in this example. The diameter of the horn's input waveguide is $d_c = 0.19$ m (which has a cut-off frequency of 0.92 GHz for the fundamental TE_{11} mode). The investigated example is a bivariate problem, with the variables being the flare angle of the horn $a_c \in [0°, 7°]$ and frequency $f \in [0.95, 1.20]$ GHz. The antenna's directivity, at broadside, varies in a highly non-linear manner, between 2.5 dB and 11 dB. The shape of the radiation pattern also varies significantly over this parameter space.

The MAS algorithm is executed starting from 10 points until the stopping criterion of $\lambda = 1$ is reached (which required 83 samples). The pattern model is constructed using Kriging as the interpolation kernel where a Matérn $\frac{5}{2}$ correlation function is used. The Matérn $\frac{5}{2}$ function is defined as

$$\psi = \left(1 + \sqrt{5}t + \frac{\sqrt{5}t^2}{3}\right) \exp\{-\sqrt{5}t\},$$

where $t = \sqrt{\sum_{m=1}^{K} \theta \times d_m^2}$, θ is the Kriging hyper-parameter, K is the number of points and d_m is the pairwise Eucledian distance [56, 65].

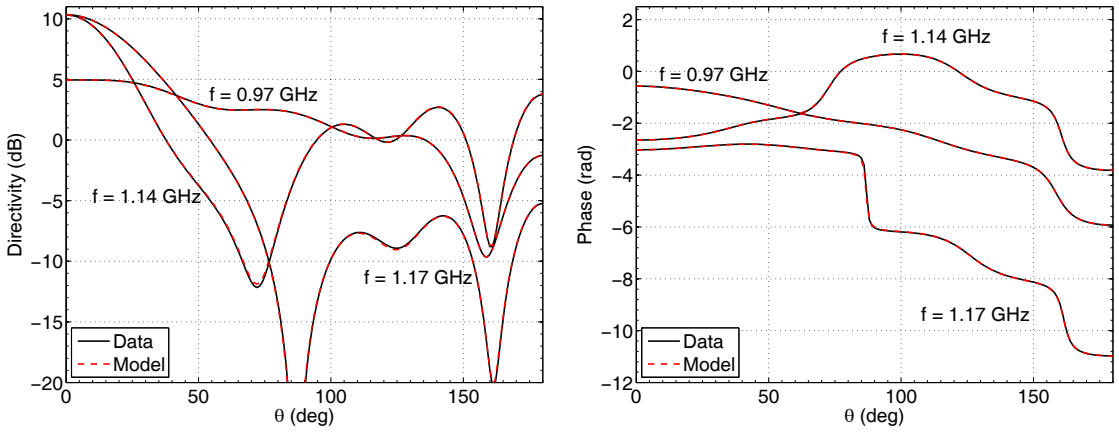

(a) (b)

Figure 4.17: (a) Directivity and (b) phase plots of the pattern in the $\phi = 90°$ plane, for a_c fixed at 1.25° while frequency varies from 0.97 GHz to 1.17 GHz. The non-linear variation of the pattern is obvious, with small changes in frequency resulting in significant pattern variations as can be seen for the cases where $f = 1.14$ GHz and $f = 1.17$ GHz.

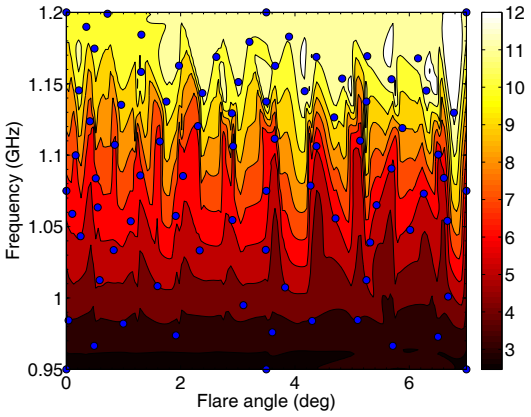

Figure 4.18: Sample distribution after the MAS algorithm has converged. The contour plot (generated with 164 points) of the broadside directivity is shown as a reference. Regions of slow and rapid variation can be seen to be sparsely and densely sampled respectively.

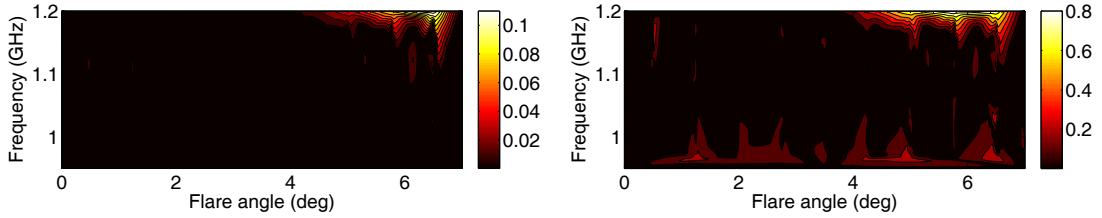

(a) (b)

Figure 4.19: (a) Maximum magnitude and (b) phase error plots of the full pattern for the entire parameter space, for 83 selected samples ($\lambda = 1$). The very low errors in the majority of the parameter space demonstrate the effectiveness of the proposed method.

The resulting model is validated over a regular 9×9 grid of points and the results are depicted in Fig. 4.17 for selected points in the validation set. The distribution of samples is shown in Fig. 4.18 where regions of fast variations can clearly be seen to be more densely sampled (even though reflective exploration is not directly performed on directivity values).

The maximum approximation RRMSE of the pattern, amongst all points in the validation set, is 0.165 and 0.882 for magnitude and phase respectively. The maximum errors occur at the edges of the parameter space as shown in Fig. 4.19, where Kriging is known to be inaccurate. Errors in the rest of the parameter space are relatively low, yielding radiation patterns with the levels of accuracy shown in Fig. 4.17. Modelling errors can be further reduced by decreasing the convergence threshold λ as is shown in Fig. 4.20 where $\lambda = 0.3$ (requiring 150 samples).

Table 4.1 compares the levels of accuracy obtained using the MAS algorithm with those that are obtained using a pre-allocation of sample points by means of Latin hypercube sampling (LHS). The comparison is made for 83 and 150 points.

Results in Table 4.1 show that errors obtained with the MAS algorithm are consistently lower in both cases, albeit with the difference being small. However,

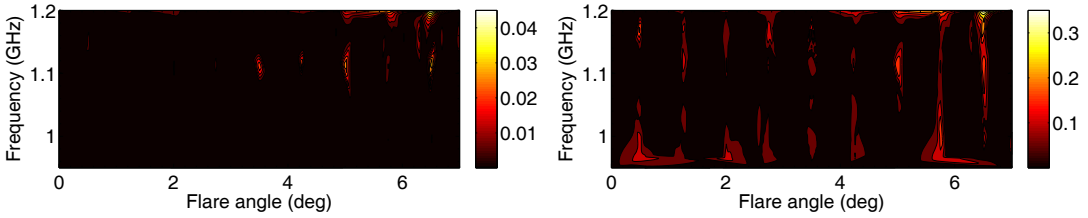

(a) (b)

Figure 4.20: Errors in directivity for 150 selected samples ($\lambda = 0.3$): (a) magnitude error, (b) phase error. The reduction in error is clear when compared to Fig. 4.19a.

Table 4.1: Magnitude RRMSE comparison between samples selected by the MAS algorithm and LHS.

83 samples			150 samples		
Error	MAS	LHS	Error	MAS	LHS
max	0.1159	0.1297	max	0.0478	0.0556
median	0.0029	0.0037	median	0.0020	0.0022
mean	0.0072	0.0142	mean	0.0051	0.0045

with LHS being a statistical sampling rule, some instances of generated samples may yield much poorer results. One such instance is investigated in what follows.

In this example, 150 points are selected using LHS enhanced by corner points. The distribution of samples is shown in Fig. 4.21, with the modelling errors being as follows: (i) mean error: 0.0068, (ii) median error: 0.0029, (iii) max. error: 0.1216. The maximum error achieved is worse than that obtained with fewer samples (83) using the MAS algorithm. This example clearly illustrate the pitfalls of simply pre-allocating samples using LHS, as unacceptably large errors in the model may occur. Also, separate instances of the sample generation leads to separate results (some good, some bad as illustrated in this section), due to the stochastic nature of a typical LHS implementation. In contrast, the proposed MAS algorithm guarantees convergence to a pattern model of *arbitrary and fully controllable accuracy*.

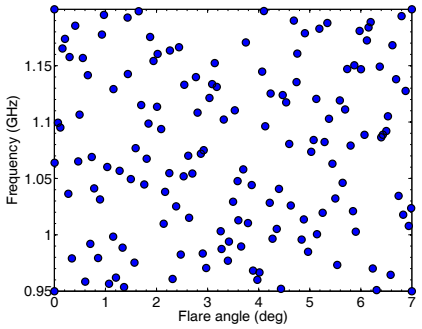

Figure 4.21: Distribution of 150 samples selected through LHS.

2. 5–D Horn Problem

A 5−D modelling problem, of the radiation pattern of a horn antenna, is explored in this section. The antenna is shown in Fig. 4.22 and the design variables are tabulated in Table 4.2. The modelled variables are of practical importance as they are usually considered in a typical design of corrugated horns.

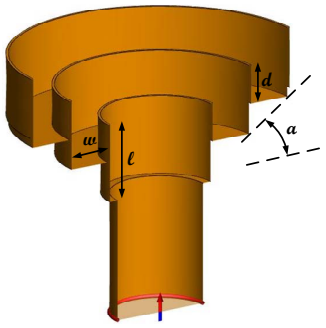

Figure 4.22: Simulation model of the horn antenna. The design variables are clearly indicated.

Table 4.2: Design parameters of the 5−D horn problem.

Parameter	Min.	Max.
a	0°	35°
ℓ	0.09 m	0.17 m
w	0.06 m	0.085 m
d	0.06 m	0.085 m
f	1 GHz	1.75 GHz

The MAS algorithm is executed on the horn starting with a set of 82 points that includes corner points as well as a subset of points generated by means of LHS. The convergence criterion is set as $\lambda = 0.055$, resulting in a total of 624 sample points (i.e., 624 calls to the EM simulator).

Using the collected data, a model for the expansion coefficients of the CBFPs is built using Kriging, with a Matérn $\frac{5}{2}$ correlation function, as the interpolant [31]. The model is built using a low-rank approximation of the column-stacked matrix of the simulated radiation patterns, i.e., the full column-rank (rank-624) matrix is approximated by a low-rank (rank-50) matrix through a truncated SVD.

The model is tested on 300 validation points (generated using LHS) and the maximum and mean errors (RRMSE) on directivity are 0.0581 and 0.0104 respectively. Concerning phase, the maximum and mean RRMSE are 0.7766 and 0.2907 respectively. The error distributions are shown in Fig. 4.23 for both directivity and

phase[4], while the patterns corresponding to the maximum and median errors are shown in Fig. 4.24.

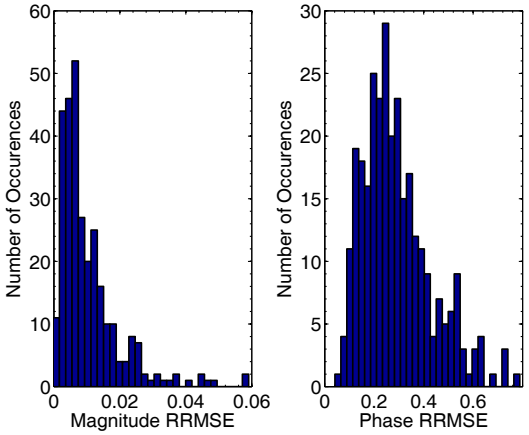

Figure 4.23: Error distribution in the validation set. Left panel: directivity. Right panel: phase. It can clearly be seen that validation points with large errors are outliers in the data, in most instances corresponding to regions near the edges of the design space.

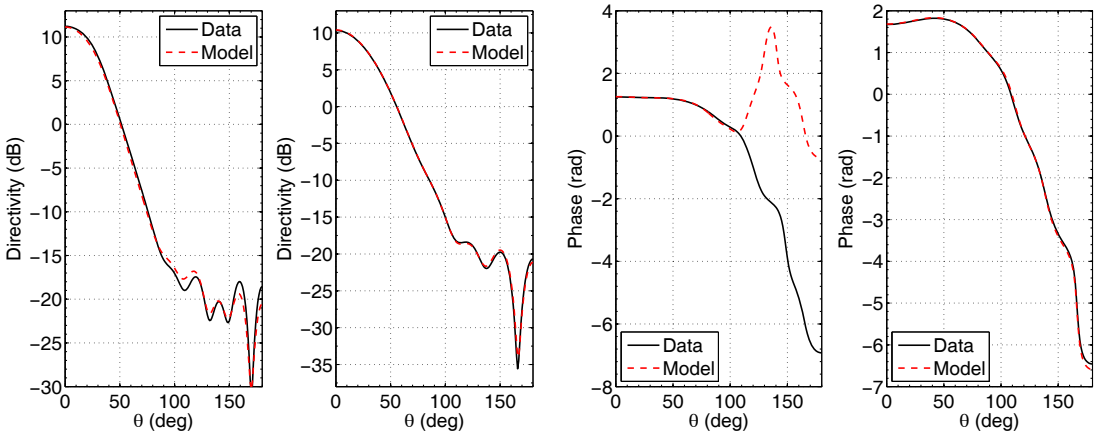

(a) Magnitude (b) Phase

Figure 4.24: Worst-case and median error (left and right panel of (a) and (b) respectively) comparison between the model and validation set in the $\phi = 90°$ plane. The full errors can of course be seen in Fig. 4.23.

It is apparent from Fig. 4.24 that the modelling error is more pronounced in the phase of the radiation pattern. However, for applications where the phase of the pattern is required, such as for reflector feed antennas, the phase is usually needed up to a limited angle $\theta_{\max} \ll 180°$, i.e., the main beam region where the magnitude of the pattern is large. As shown in Fig. 4.24b, the worst case recovered phase is accurate beyond the main beam of the radiation pattern and thus the obtained model is usable even for such applications.

[4]The phase error is computed as the RRMSE of the co-polarised electric field.

4.3 Inclusion of S-parameters – MAS

In this section, we extend the algorithms proposed in the previous section to include S-parameter dependence. We stress that the discussion on S-parameters is limited to the reflection coefficient. However, the developed techniques can easily be extended to model the full scattering matrix by adopting the approach of multiple reflective functions similar to the one discussed in Sec. 4.2. The end results are algorithms that can be used to efficiently fully characterise a multi-port antenna.

An extension of the MAS algorithm to include S-parameter dependence is presented in this section. We first remark that S-parameter dependence is, in general, polynomial in geometric parameters and rational in frequency. In light of the above observation, the multivariate modelling of S-parameters can be accomplished by means of the following expression borrowed from the parametric macromodeling literature [22, 23, 25, 49]

$$\boldsymbol{R}(s,\boldsymbol{g}) = \frac{N(s,\boldsymbol{g})}{D(s,\boldsymbol{g})} = \frac{\sum_{p=0}^{P}\sum_{\boldsymbol{v}\in V} c_{p\boldsymbol{v}}\phi_p(s)\varphi_{\boldsymbol{v}}(\boldsymbol{g})}{\sum_{p=0}^{P}\sum_{\boldsymbol{v}\in V} \tilde{c}_{p\boldsymbol{v}}\phi_p(s)\varphi_{\boldsymbol{v}}(\boldsymbol{g})}, \tag{4.19}$$

where $\phi_p(s) = \frac{1}{s-a_p}$ is a rational function of frequency s, and $\varphi_{\boldsymbol{v}}(\boldsymbol{g})$ is a geometry-dependent basis function (a piecewise linear function in [49] or polynomials in [25]). The formulation in (4.19) requires treating frequency as a special parameter, i.e., running EM simulations at multiple frequency points for each fixed geometry (an anti-thesis to the MAS algorithm of Sec. 4.2 where frequency is treated like any other parameter).

Therefore, in order to easily integrate S-parameter modelling with the MAS technique, a general interpolating function like Kriging is chosen to model S-parameter dependence, as in [21], where frequency and geometry-dependent variables are treated alike.

The exploitation technique described in Sec. 4.2.3 is applied to S-parameters, with the obvious modification that the actual S-parameter values are used as function outputs, and an exploitation score is computed as in Sec. 4.2.4. The new ranking criterion to select the next point (to run the EM simulation at) is then defined as

$$R_n(\boldsymbol{p}_t) = \beta_1 Q^r(\boldsymbol{p}_t) + \beta_2 Q^s(\boldsymbol{p}_t) + \beta_3 V(\boldsymbol{p}_t), \tag{4.20}$$

where $V(\boldsymbol{p}_t)$ is the exploration defined in (4.16), $Q^s(\boldsymbol{p}_t)$ is the exploitation score of S-parameters (i.e.,(4.15) applied to S-parameter data), $Q^r(\boldsymbol{p}_t)$ is the exploitation score of radiation patterns and $\boldsymbol{p}_t$ is a point in the set of candidate points, $\mathcal{T}_{new}$ (see Sec. 4.2.2 and Sec. 4.2.3).

Differently from the criterion in Sec. 4.2.5 (see (4.18)), the stopping criteria for the pattern and S-parameters are normalised to be in a common range of (0,1). Furthermore, this normalisation allows one to more intuitively define a stopping

criterion regardless of the values of the antenna's gain[5]. The stopping criteria for the pattern and S-parameters are defined as

$$\mathcal{H}\left\{\max\left\{\left|\frac{\mathcal{M}_h^{(j)}-\mathcal{M}_l^{(j)}}{\mathcal{M}_h^{(j)}}\right|\right\}\right\}<\lambda_1, \tag{4.21}$$

$$\mathcal{H}\left\{\max\left\{\left|\frac{\mathcal{M}_h^{s}-\mathcal{M}_l^{s}}{\mathcal{M}_h^{s}}\right|\right\}\right\}<\lambda_2, \tag{4.22}$$

where $\lambda_{\{1,2\}}$ are user-defined tolerance, $\mathcal{H}\{\cdot\}$ is defined as in (4.18) and $\mathcal{M}^s_{\{h,l\}}$ are the S-parameter reflective functions.

The averaging functions in (4.18) and (4.22) are smooth and generally decreasing approximations of the true error (i.e., difference between reflective functions). The true error function is not smooth or monotonic due to changing candidate points from one iteration to another as shown in Fig. 4.27a. Therefore, the true error is not suitable as a measure of convergence. On the other hand, since $\mathcal{H}\{\cdot\}$ is smooth and monotonically decreasing, the stopping criteria $\lambda_{\{1,2\}}$ can be chosen to be small in order to ensure that all relevant features of the reflective functions are captured over the design space (in line with standard reflective exploration principles). Our experiments on various antennas suggest that values of $\lambda_{\{1,2\}} \leqslant 1\times10^{-2}$ are sufficient in order to obtain accurate models, with smaller values leading to even more accurate models at the cost of an increasing number of EM simulations. The values of λ_1 and λ_2 can effectively be used to control the approximation error of the models built with the generated basis functions.

The extended MAS algorithm then converges when the expressions in (4.21) and (4.22) are both satisfied n times (where n is a small integer), to build some robustness into the algorithm.

Some pertinent numerical examples are presented in the subsequent section to validate the extended MAS approach.

4.3.1 Numerical Examples II

Three examples are presented herein. The first example involves the same horn antenna from Section 4.2.6, the second involves a 6−D aperture coupled patch antenna and the final example involves a log-periodic pyramidal sinuous antenna.

1. Horn Near Cut-off

The extended MAS algorithm is executed, on the horn of Sec. 4.2.6, starting from 10 points until the stopping criteria of $\lambda_1 = \lambda_2 = 10^{-3}$ are reached, which required an additional 103 samples selected adaptively by using a balanced weighting scheme,

[5]Antennas with high gain are associated with high values of e_1 and e_2.

$\beta_i = 1\ \forall i$, in the ranking score of (4.20). The pattern and S-parameter models are constructed using Kriging as the interpolation kernel where a Matérn $\frac{5}{2}$ correlation function is used. The resulting models are validated over a dense grid of 1024 points, shown in Fig. 4.25, and the pattern results are depicted in Fig. 4.26 for selected points in the validation set (the selected points are those with median validation errors).

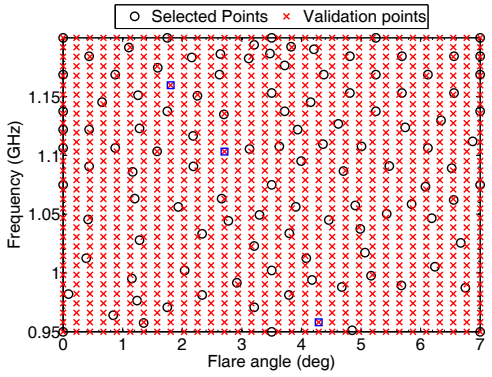

Figure 4.25: Estimation and validation samples

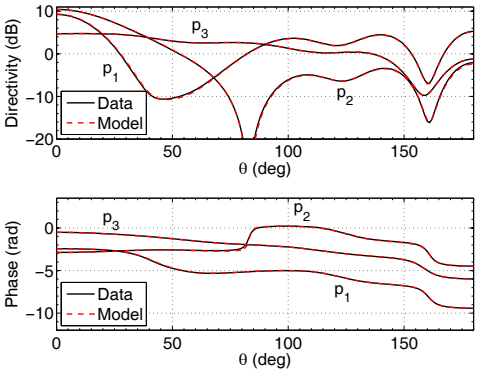

Figure 4.26: Horn: Directivity (top panel) and phase (bottom panel) plots of the pattern in the $\phi = 90°$ plane, for $p_1 = \{2.71, 1.10\}; p_2 = \{1.81, 1.16\}$ and $p_3 = \{4.29, 0.96\}$, which are indicated as □ in Fig. 4.25. The non-linear variation of the pattern is obvious.

The convergence rate of the MAS algorithm is shown in Fig. 4.27a, where it is apparent that the true error, (4.18) with no averaging, is unsuitable to be used for convergence purposes (i.e., it has many peaks). The averaged pattern error function is shown to be smooth and monotonically decreasing until the criterion of $\lambda_{\{1,2\}} < 10^{-3}$ is satisfied. The S-parameter error function follows a similar trend, as shown in Fig. 4.27b.

Fig. 4.28 illustrates the evolution of the algorithm from one iteration to another, highlighting the Voronoi diagram at each iteration with the associated candidate points on which exploration and exploitation metrics are calculated. Also shown in Fig. 4.28 are the points in the set $\mathcal{V}$ that are excluded from the set of candidate

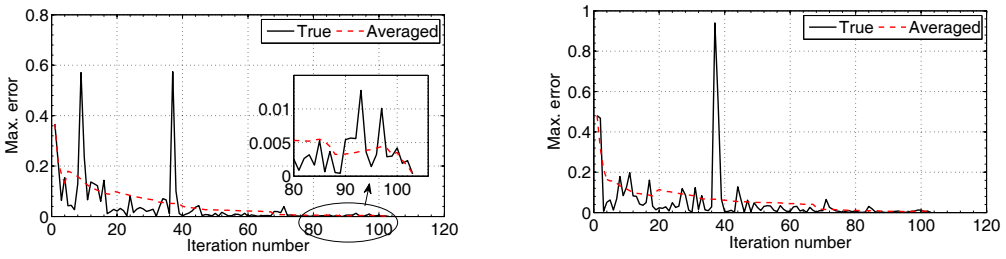

Figure 4.27: Horn: (a) Convergence of pattern error function of MAS algorithm. The true error is not smooth due to changing sets of candidate points between iterations. A smooth and decreasing averaged error can be clearly seen. (b) S-parameter error function.

points as discussed in Step 3 of the exploitation algorithm in Sec. 4.2.3. It can clearly be seen in Fig. 4.28 that the number and the location of the candidate points changes from one iteration to the next.

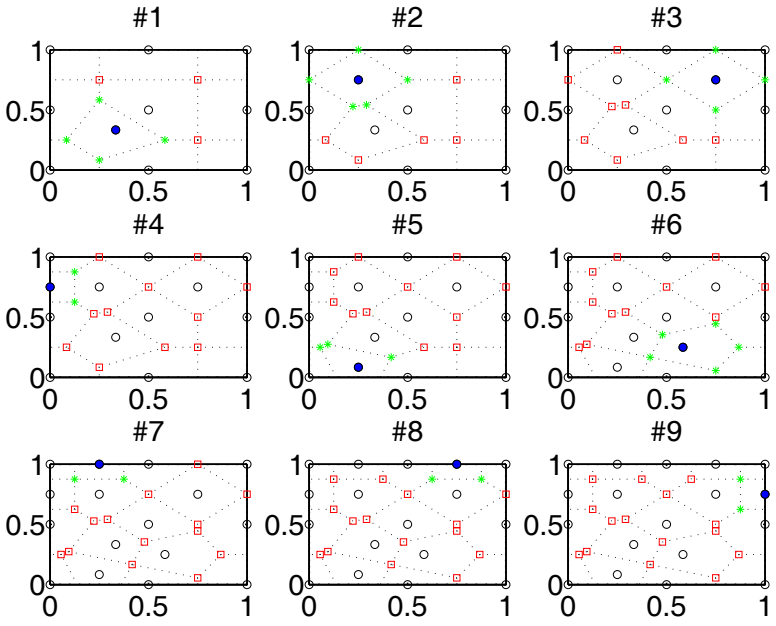

Figure 4.28: Horn: Evolution of the MAS algorithm through the first 9 iterations. They x- and y-axes are normalised flare angle and frequency respectively. The simulated samples are shown as ∘ and the latest sample is indicated by •. Points in the set $\mathcal{V}$ are shown as * , while the candidate points are shown as □. The dotted line indicates the boundaries of each cell of the Voronoi diagram.

The Voronoi diagram obtained upon convergence of the extended MAS algorithm is shown in Fig. 4.29 where region of fast and slow variations are clearly distinguishable by the size of the Voronoi cells.

To illustrate the effectiveness of our approach, a comparison is made between the model obtained with the extended MAS technique with a model obtained using 150 points generated by means of LHS. The maximum magnitude modelling errors are 0.089 and 0.126 for the MAS and LHS models respectively (the correspond-

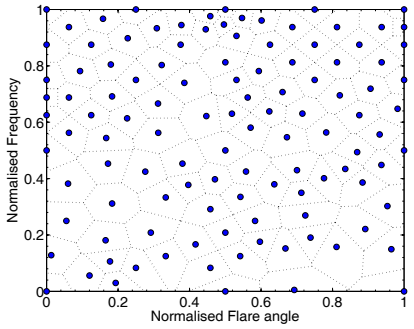

Figure 4.29: Horn: Voronoi diagram of the parameter space with all samples (•) selected.

ing maximum phase errors are 0.96 and 0.90). The magnitude modeling errors are shown in Fig. 4.30 which demonstrates that a better model is obtained with fewer points with our proposed approach than with common LHS based sampling schemes. Moreover, owing to the stochastic nature of LHS, no measure of error control can be guaranteed, i.e., an LHS-based distribution of a specified number of points may or may not yield a sufficiently accurate model (unless the data set is large). In contrast, the proposed MAS algorithm guarantees models of arbitrary accuracy as desired by a user.

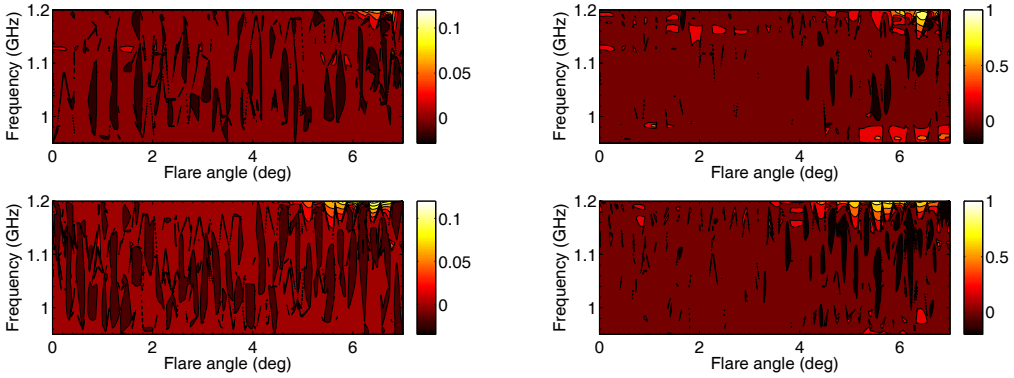

(a) Directivity errors (b) Phase errors

Figure 4.30: Maximum directivity and phase errors for 113 points selected with MAS (top panel) and 150 points selected with LHS (bottom panel). It is evident that a better model is obtained with the proposed MAS technique. The depicted errors can be further reduced by lowering the values of λ_1 and λ_2.

The accuracy of the S-parameter model is shown in Fig. 4.31, where low absolute difference errors can be observed over the parameter space. The maximum absolute error obtained with an LHS-based model (with 150 samples) is 0.184 compared to a maximum of 0.163 obtained with the extended MAS technique, further highlighting the superior performance of the proposed even fewer samples.

Thus far, the extended MAS has been illustrated for the case where the weighting factors in (4.20) are all equal to 1. In what follows we investigate the effects of different weighting factors on the performance of the extended MAS technique.

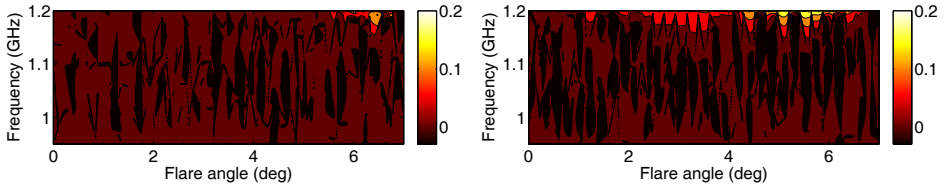

Figure 4.31: Absolute difference error between model and validation data: (a) MAS, (b) LHS. The maximum, mean and median errors are 0.164, 45×10^{-3} and 18×10^{-3} for MAS; and 0.1842, 76×10^{-3} and 18×10^{-3} for LHS respectively.

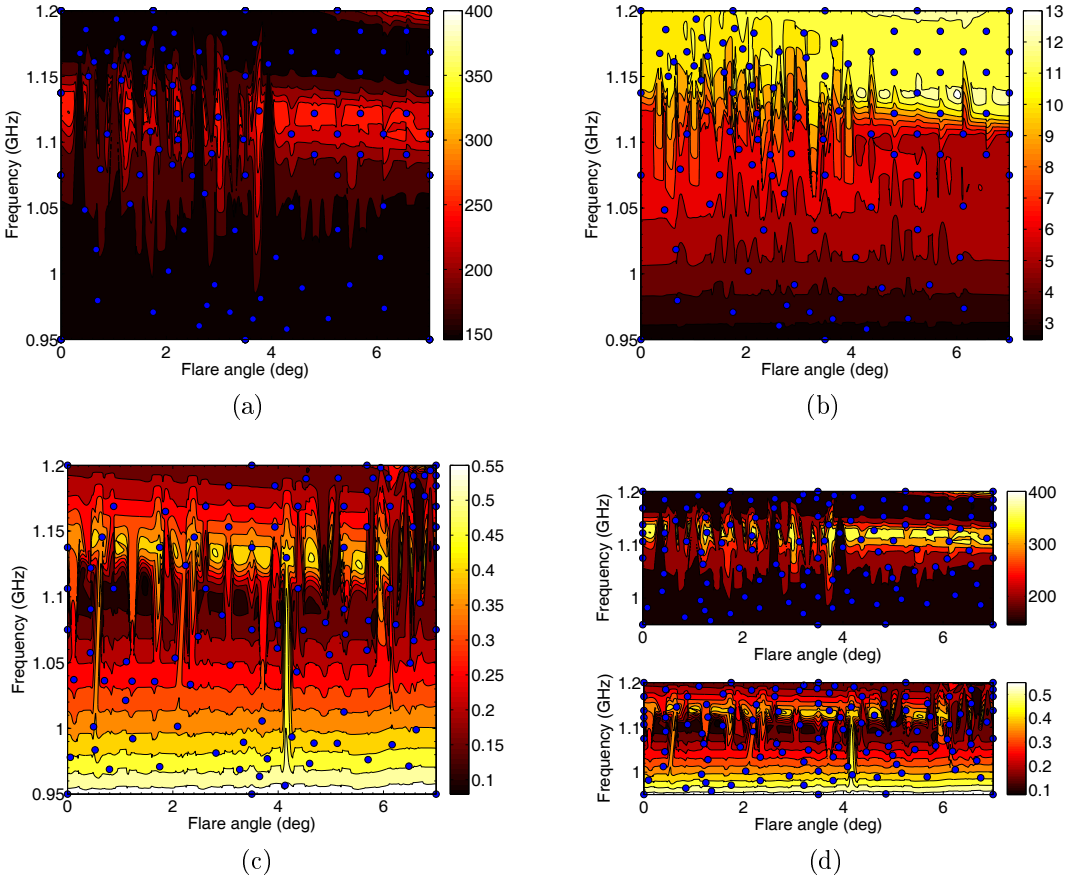

Figure 4.32: Horn: Sample distributions (shown as •) for different weighting factors. (a) Variation of e_2 and the selected samples with weighting factors $\beta_1 = 1, \beta_2 = 0, \beta_3 = 1$ – pattern modeling only. The corresponding directivity (not in dB) is shown in (b). (c) Variation of the magnitude of S-parameters and selected samples with weighting factors $\beta_1 = 0, \beta_2 = 1, \beta_3 = 1$ – S-parameter modeling only. (d) Variation of e_2 (top panel) and S-parameter variation (bottom panel) for balanced weighting factors $\beta_1 = 1, \beta_2 = 1, \beta_3 = 1$ – combined pattern and S-parameter modeling. Higher sample densities in regions of fast function variation can clearly be seen in all figures. We stress that only one (e_2) of the two coefficients (e_1, e_2) necessary to quantify pattern variations is shown. The underlying contour plots were generated using 1024 validation points plus 113 points estimation data from (d).

Note that only the extreme cases are investigated as there infinitely many combinations for $\beta_{1,2,3}$ in (4.20). Fig. 4.32 shows contour plots of the variation of S-parameters and e_2 (see Section 4.2.3) as well as the samples selected by the MAS

algorithm for different values of the weighting factors β_i in (4.20). A higher concentration of samples can be seen in regions of more dynamic variations of the pattern (represented by the self-expansion coefficients e_2 and directivity in Fig. 4.32a and 4.32b) or S-paramters, while simultaneously there aren't any large unsampled regions in the parameter space (due to the exploration property of the ranking selection).

All models in Fig. 4.32 are validated over the same dense set of 1024 samples. Validation error information is presented in Table 4.3, where it can be seen that the smallest numbers of EM simulations occur for the cases in which either S-parameters or radiation patterns are solely investigated. Moreover, the results in Table 4.3 suggest that convergence criteria stricter than 10^{-3} are required to model the pattern and S-parameter with a high degree of accuracy, for the top two modelling scenarios in Table 4.3. Simply put, too few points are required to reach $\lambda_{\{1,2\}} = 10^{-3}$ without resolving all function features – especially at the edges were maximum errors occur.

Table 4.3: Modeling details for different weighting factors. The reported errors are RRMSE and absolute difference for the pattern and S-parameters respectively.

Weights			Criteria		Max. Error		#
β_1	β_2	β_3	λ_1	λ_2	Pattern	S-param.	Points
1	0	1	10^{-3}	N/A	0.114	0.1755	100
0	1	1	N/A	10^{-3}	0.202	0.053	105
1	1	1	10^{-3}	10^{-3}	0.089	0.168	113
1	1	0	10^{-3}	10^{-3}	0.092	0.162	118

2. Aperture-coupled Patch Antenna

An aperture coupled patch antenna, shown in Fig. 4.33, is investigated in this example. The model consists of 6 variables that are described in Fig. 4.33.

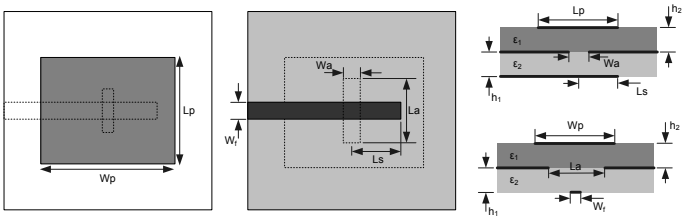

Figure 4.33: Detailed geometry of the aperture coupled antenna. The variables involved are: $W_a \in [1.2, 1.8]$ mm; $L_a \in [35, 46.5]$ mm; $L_s \in [6, 8]$ mm ; $L_p \in [50, 60]$ mm; $W_p \in [65, 80]$ mm and $f \in [1.6, 2.4]$ GHz. The remaining parameters are fixed at $h_1 = 1.5$ mm, $h_1 = 12$ mm, $\varepsilon_1 = 1$, $\varepsilon_2 = 4.3$ and $W_f = 3$ mm.

The adaptive sampling algorithm is executed by starting with 75 points (including corner points), and the convergence parameters are set as $\lambda_1 = \lambda_2 = 5 \times 10^{-2}$. The algorithm converges after the parameters λ_1 and λ_2 are reached a number of $n = 2$ times, and this requires a total of 625 samples. The evolution of the error metrics from iteration to iteration is shown in Fig. 4.34 for both the radiation patterns as well as S-parameters, where a generally decreasing trend can be observed.

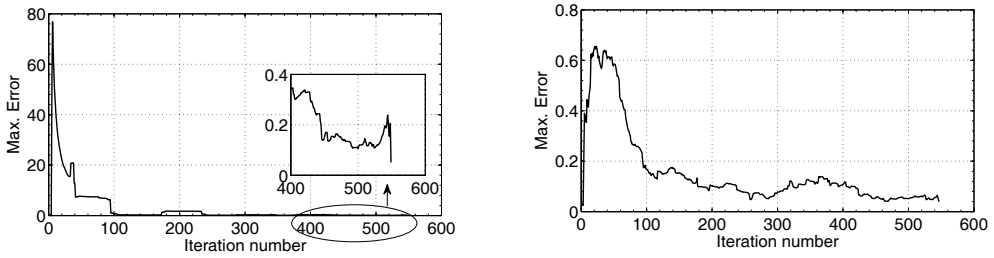

(a) (b)

Figure 4.34: Patch: Convergence of error functions – (a) Pattern; (b) S-parameters. Some values in (a) are larger than 1 due to the normalisation factor, $\mathcal{M}_h^{(j)}$ in (4.21) having a value smaller than one for some iterations.

The model is built as in the previous example and it is validated on a set of 300 points and the error distribution is shown in Fig. 4.35, where it can clearly be seen that models with large errors are outliers. A comparison between the pattern model and selected validation data is shown in Fig. 4.36, where a relatively good agreement can be observed.

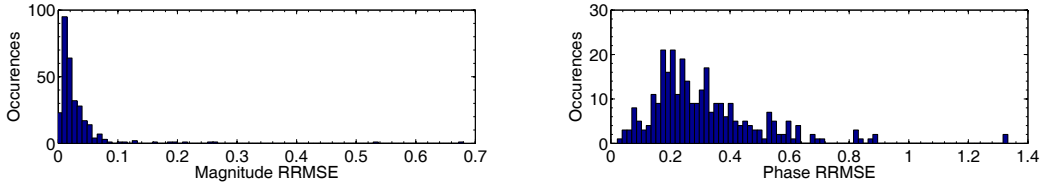

(a) (b)

Figure 4.35: (a) Magnitude and (b) phase error distribution over a validation set of 300 samples.

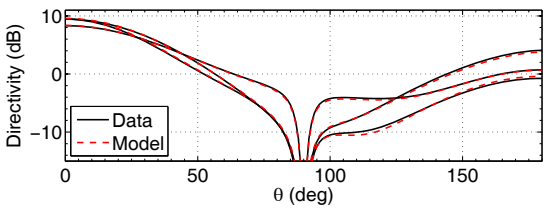

Figure 4.36: Accuracy of the radiation pattern model at selected points in the validation set, in the $\phi = 45°$ plane.

The maximum absolute difference error in the model of the associated S-parameters is 0.111 over the validation set, with mean and median absolute errors given by 0.0154 and 0.009 respectively. Fig. 4.37 shows a comparison between model and data at selected points in the validation set and a relatively good agreement can be observed between various curves.

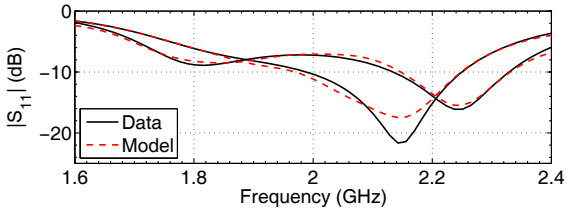

Figure 4.37: Data vs model at selected points in the validation set.

3. Pyramidal Sinuous Antenna

A pyramidal sinuous antenna is investigated in this example. The antenna is shown in Fig. 4.38 and the design parameters are described in Table 4.4 (See [61] for a description of α and β). The adaptive sampling algorithm is executed starting with 72 points generated by means of LHS (including corner points) and the convergence thresholds are set as $\lambda_1 = \lambda_2 = 5 \times 10^{-2}$ respectively, and $n = 2$.

Table 4.4: Design parameters of the 4-D pyramidal sinuous antenna problem.

Parameter	Min.	Max.	Description
θ	50°	55°	Pyramid flare angle
α	22°	25°	Angular width
β	14°	17°	Rotation angle
f	3 GHz	5 GHz	Frequency

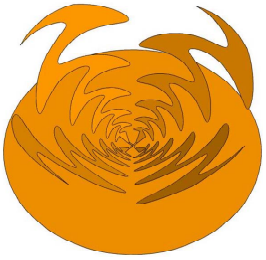

Figure 4.38: Simulation model of the pyramidal sinuous antenna.

A grand total of 588 points are required for the stopping criteria to be met. Fig. 4.39 shows the variation of $\lambda_{\{1,2\}}$ as the algorithm evolves. The pattern model is built as in previous cases and validated on a set of 300 samples.

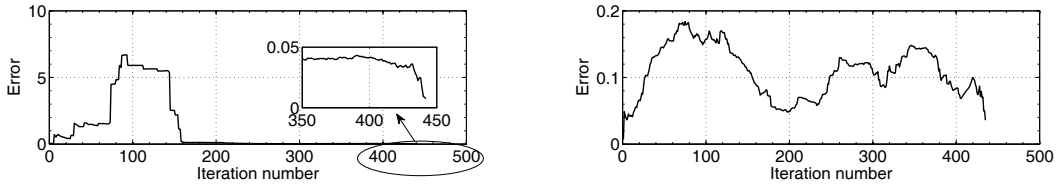

(a) (b)

Figure 4.39: Pyramidal sinuous antenna: Convergence of error functions – (a) Pattern; (b) S-parameters.

The error distributions are shown in Fig. 4.40 for magnitude and phase respectively, where it can clearly be seen that the vast majority of the evaluated models have low errors compared to the corresponding validation data.

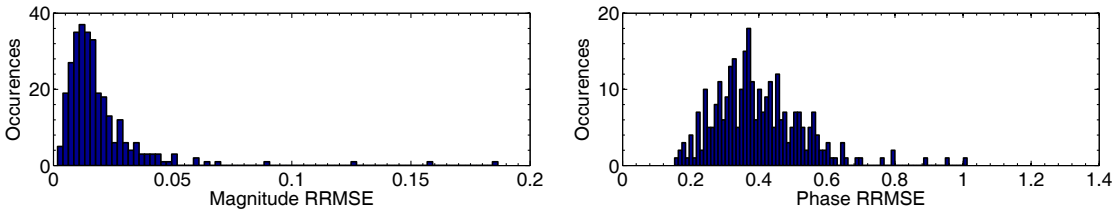

(a) Magnitude (b) Phase

Figure 4.40: Error distribution over validation set.

Fig. 4.41 shows a comparison between pattern models and data at selected points in the validation set, where a good agreement can be observed.

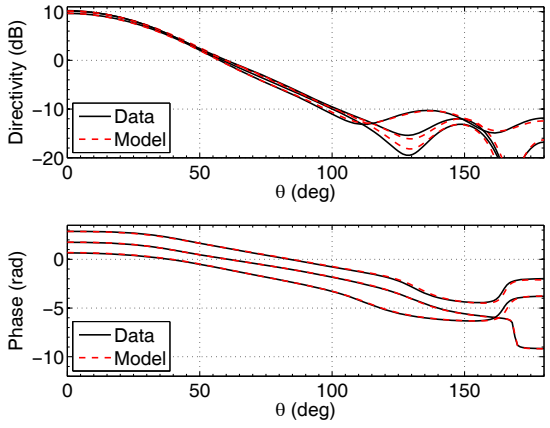

Figure 4.41: Comparison between data and model at selected points in the validation set, in the $\phi = 0°$ plane.

Concerning S-parameters, a comparison between the model and a randomly selected point in the validation set is shown in Fig 4.42, revealing a good agreement between data and model.

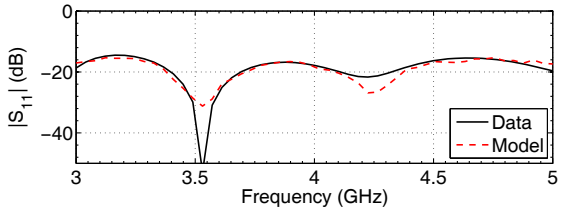

Figure 4.42: Comparison between S-parameter data and model at a random point in the validation set. The maximum absolute difference error in this example is 0.04.

A comparison between S-parameter models obtained using the extended MAS algorithm with different convergence criteria is shown in Table 4.5, where only a marginal decrease in the overall error can be observed even after adding $\sim$ 300 points (a similar trend is observed in the radiation pattern errors). This suggests that the model obtained with $\lambda_1 = \lambda_2 = 5 \times 10^{-2}$ is already near-optimal.

Table 4.5: Error comparison between two different models: Model A (presented in previous paragraphs) has 588 points and Model B has more stringent convergence criteria that required 867 points. Absolute difference errors in S-parameters are reported.

# points	$\lambda_{\{1,2\}}$	max	mean	median
588	5×10^{-2}	0.1047	0.0179	0.0132
867	2×10^{-2}	0.1010	0.0165	0.0125

4.3.2 Discussion

We remind the reader that traditional frequency domain EM simulations are repeatedly carried out at multiple frequency points for a fixed geometry. The proposed method treats frequency like an ordinary parameter and optimally places samples in the subspace of geometric parameters and frequency. As such, the computational cost of the proposed method in the horn example is equivalent to about 11 traditional EM simulations, even when advanced frequency sampling algorithms, such as [32], are used (the mean number of frequency points selected using [32], on 10 different geometries of the antenna, is about 10). For the example involving the patch antenna, the equivalent computational cost is only about 40 traditional simulation (also enhanced with adaptive frequency sampling),s a very small number for a 5-D problem. For the example involving the pyramidal sinuous antenna, the total computational cost is equivalent to about 33 traditional simulations (enhanced with [32] or the technique in Section 4.1.5).

Therefore the proposed method allows one to obtain more information about the variation of the antenna's output characteristics, as a function of design parameters, at a fraction of the computational cost when the same antenna is modelled using traditional techniques. Additionally, the proposed method adaptively constructs a

single model for the full radiation pattern, thereby avoiding the need for building separate models for each figure of merit (e.g., directivity, level of back lobe radiation, etc...). Indeed, the outcome of the proposed technique is a single model that fully characterizes an antenna. The obtained model is quick to evaluate (~ 0.3 s) and may be efficiently used for design activities like optimisation and sensitivity analysis.

We also note that far fewer samples are required in cases where frequency variation is not included or for narrow band models.

Furthermore, the distinguished feature of the proposed models is that they have a fully controllable approximation error that is determined by the values of λ_1 and λ_2. Note that λ_1 and λ_2 in (4.21) and (4.22) are normalised values and thus are independent of the particular antenna under consideration. We however suggest values of $\lambda_{\{1,2\}} \leqslant 5 \times 10^{-2}$ in order to obtained sufficiently accurate models, with lower values leading to better accuracy and, of course, an increased number of EM simulations.

4.4 Application Example

In this section, the developed pattern models are used in a design optimisation example to illustrate their effectiveness. The horn example in Sec. 4.2.6 is designed to be used as a feed for a prime-focus reflector with a subtended half-angle of 49°. The horn is optimised for aperture efficiency and relative cross-polarisation in the $1 - 1.7$ GHz band. Aperture efficiency is calculated by integrating the radiated electric field as described in [66] while the reduction of cross-polarisation only within the subtended angle is sought after. The parameter range of the horn in Sec. 4.2.6 is repeated here for the reader's convenience.

Table 4.6: Design parameters of the horn problem.

Parameter	Min.	Max.
a	0°	35°
ℓ	0.09 m	0.17 m
w	0.06 m	0.085 m
d	0.06 m	0.085 m

The optimisation goals are as follows: (i) an aperture efficiency better than 74% for a subtended half-angle of 49° and a relative cross-polarisation below -30 dB over the bandwidth of interest. The parametrised model is evaluated at 35 frequency points in 12.05 s. The model is optimised using MATLAB's `fmincon` function [42], requiring a total of 198 function evaluations in a total time of 37.5

minutes. The values of the design parameters at optimum are $a = 17.25°; \ell = 0.1675$ m; $w = 0.0850$ m and $d = 0.0759$ m.

The corresponding full-wave simulation time for 198 iterations is 1490.3 minutes. Therefore optimisation using the parametrised pattern model provides a speed-up of at least 39× compared to traditional methods. The results obtained at optimality are shown in Fig. 4.43 where a good agreement between the model's results and EM validation data can be observed.

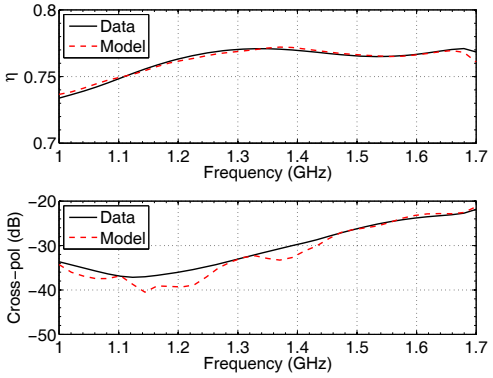

Figure 4.43: Comparison between model and validation data: aperture efficiency (top panel), relative cross-polarisation (bottom panel).

This example clearly demonstrates the efficiency and applicability of the developed models in a realistic design. The re-usability, accuracy and time savings afforded by the model make a strong case for its adoption as an enhancement of a conventional antenna design cycle.

4.5 Conclusion

This chapter presented a class of adaptive sampling algorithms to efficiently build parametrised models of radiation patterns (over a large angular region) and S-parameters of antennas. A novel approach to represent radiation patterns, namely using the first two expansion coefficients of CBFPs, was used in order to determine pattern variation in a compact manner. Using this idea, four adaptive sampling algorithms were proposed. The first algorithm, AFS, modelled pattern variation as a function of frequency by adaptively selecting a few frequency points at which EM simulations are carried out. The net result from AFS is a wideband model of the radiation pattern that is evaluated very rapidly and built using a minimum number of EM simulations. The second algorithm is an extension of AFS to include S-parameter dependence (also as a function of frequency). The third algorithm, MAS, extends AFS to a multivariate setting. Finally, the MAS algorithm is also extended to include S-parameter dependence. The class of proposed algorithms is

based on the principle of reflective exploration and has the useful feature of absolute error control.

The proposed models have been validated in a wide range of examples, including a design test case where an improvement of at least 39× in optimisation time may be obtained. The accuracy of the models' results confirm their reliability as surrogate models that may be used in a variety of ways to enhance a typical antenna design cycle.

The AFS algorithm was published in an international conference [32] and work concerning the extended MAS algorithm is to be submitted to an international journal, namely the IEEE Transactions on Antennas and Propagation [33].

Chapter 5

Conclusion

This dissertation presented efficient methods to characterise antenna responses in two different settings, namely, calibration of reflector antennas and the electrical design of antennas, in both cases improving upon the state of the art.

Concerning calibration, a method has been devised to recover the radiation pattern, resulting from some physical deformation of an offset Gregorian reflector antenna, over a wide frequency bandwidth by taking a few directional measurements at a single frequency. The method combines the basic CBFP technique [11, 12, 16] with the linear algebraic notion of subspace projection leading to improvements upon the state of the art.

On the antenna design front, we have proposed a technique to generate models of the full radiation pattern (up to a full sphere) parametrised with respect to multiple design variables. The proposed method extends the state of the art from a univariate to a multivariate setting. The proposed algorithm relies on subspace projection and is essentially independent of the interpolation kernel used as opposed to previous work in [15] that is strongly dependent on the regression function used. We stress that it is difficult to know the best regression function *a priori* as shown in the dipole example in Chapter 3. Furthermore, parametric macromodeling techniques are coupled to the proposed method in order to accurately model the associated S-parameters, thereby fully characterising the antenna.

In Chapter 4, a class of adaptive sampling algorithms are proposed to ease the model building process as well as to reduce the computational cost of frequency domain simulations of antennas in general. Indeed, we propose the first adaptive frequency sampling (AFS) algorithm that involves the full radiation pattern. The AFS algorithm allows one to accurately obtain the full radiation pattern over a wide frequency bandwidth while simulating the antenna at a few judiciously chosen frequency points. Furthermore, a multivariate adaptive sampling (MAS) algorithm is proposed to model an antenna's full radiation response as a function of multiple design parameters (including frequency). Both the MAS and AFS algorithms are

based on the principle of reflective exploration and are equipped with measures of absolute error control. Both the AFS and MAS techniques are the first adaptive sampling methods that involve the full radiation pattern. Pattern variation is modelled indirectly through the expansion coefficients of the CBFPs. For completeness' sake, we couple the MAS and AFS algorithms with well established S-parameter modelling techniques to result in a full characterisation of an antenna as a function of multiple parameters.

Possible expansions may include:

- The current error estimation procedure is based the leave-one-out approach. A better error estimation procedure would improve the convergence properties of the MAS technique. A possible metric to try would be the k-fold cross-validation or an error metric that is loosely based on expected improvement [67].
- Another interesting aspect would be to use functions other than Kriging as reflective functions in MAS and possibly a hybridisation of reflective functions for the CBPF expansion coefficients.

Bibliography

[1] J. Jonas, "MeerKAT-the South African array with composite dishes and wide-band single pixel feeds," *Proc. IEEE*, vol. 97, no. 8, pp. 1522 –1530, aug. 2009.

[2] SKA Telescope . [Online]. Available: http://www.skatelescope.org

[3] V. Galindo-Israel and R. Mittra, "A new series representation for the radiation integral with application to reflector antennas," *IEEE Trans. Antennas Propag.*, vol. 25, no. 5, pp. 631–641, September 1977.

[4] E. K. Miller, "Model-based parameter estimation in electromagnetics. I. background and theoretical development," *IEEE Antennas Propag. Mag.*, vol. 40, no. 1, pp. 42–52, Feb 1998.

[5] ——, "Model-based parameter estimation in electromagnetics. II. applications to EM observables," *IEEE Antennas Propag. Mag.*, vol. 40, no. 2, pp. 51–65, Apr 1998.

[6] ——, "Using adaptive estimation to minimize the number of samples needed to develop a radiation or scattering pattern to a specified uncertainty," *ACES J.*, vol. 17, no. 3, pp. 176–186, Nov 2002.

[7] ——, "Adaptive sparse sampling to estimate radiation and scattering patterns to a specified uncertainty with model-based parameter estimation: Compute patterns using as few as two to four samples per lobe." *IEEE Antennas Propag. Mag.*, vol. 57, no. 4, pp. 103–113, Aug 2015.

[8] D. H. Werner and R. J. Allard, "The simultaneous interpolation of antenna radiation patterns in both the spatial and frequency domains using model-based parameter estimation," *IEEE Trans. Antennas Propag.*, vol. 48, no. 3, pp. 383–392, Mar 2000.

[9] R. J. Allard and D. H. Werner, "The model-based parameter estimation of antenna radiation patterns using windowed interpolation and spherical harmonics," *IEEE Trans. Antennas Propag.*, vol. 51, no. 8, pp. 1891–1906, Aug 2003.

[10] W. Dullaert and H. Rogier, "Novel compact model for the radiation pattern of UWB antennas using vector spherical and Slepian decomposition," *IEEE Trans. Antennas Propag.*, vol. 58, no. 2, pp. 287–299, Feb 2010.

[11] A. Young, "Improving the direction-dependent gain calibration of reflector antenna radio telescopes," Ph.D. dissertation, University of Stellenbosch, Stellenbosch, South Africa, 2013.

[12] A. Young, R. Maaskant, M. V. Ivashina, D. I. L. de Villiers, and D. B. Davidson, "Accurate beam prediction through characteristic basis function patterns for the MeerKAT/SKA radio telescope antenna," *IEEE Trans. Antennas Propag.*, vol. 61, no. 5, pp. 2466–2473, May 2013.

[13] R. Maaskant and M. V. Ivashina, "Characteristic basis function patterns – a novel expansion method for the fast and accurate prediction of antenna array beams," in *Int. Conf. Electromagn. Adv. Appl. (ICEAA)*, Sept 2012, pp. 796–799.

[14] R. Maaskant, M. V. Ivashina, S. J. Wijnholds, and K. F. Warnick, "Efficient prediction of array element patterns using physics-based expansions and a single far-field measurement," *IEEE Trans. Antennas Propag.*, vol. 60, no. 8, pp. 3614–3621, Aug 2012.

[15] M. A. Francavilla, G. Giordanengo, M. Righero, G. Vecchi, and F. Vipiana, "Physics-based parametric interpolation," in *9th Eur. Conf. Antennas Propag. (EuCAP)*, Lisbon, Portugal, Apr. 2015.

[16] G. Giordanengo, M. Righero, F. Vipiana, G. Vecchi, and M. Sabbadini, "Fast antenna testing with reduced near field sampling," *IEEE Trans. Antennas Propag.*, vol. 62, no. 5, pp. 2501–2513, May 2014.

[17] O. M. Bucci and F. G., "On the spatial bandwidth of scattered fields," *IEEE Trans. Antennas Propag.*, vol. AP-35, no. 12, pp. 1445–1455, Dec. 1987.

[18] O. M. Bucci and C. Gennarelli, "Use of sampling expansions in near-field - far-field transformations: the cylindrical case," *IEEE Trans. Antennas Propag.*, vol. 36, no. 6, pp. 830–835, June 1988.

[19] O. M. Bucci and G. Di Massa, "The truncation error in the application of sampling series to eletromagnetic problems," *IEEE Trans. Antennas Propag.*, vol. 36, no. 7, pp. 941–949, July 1988.

[20] O. M. Bucci, C. Gennarelli, and S. C., "Optimal interpolation of radiated fields over a sphere," *IEEE Trans. Antennas Propag.*, vol. 39, no. 11, pp. 1633–1643, Nov. 1991.

[21] D. Deschrijver, K. Crombecq, H. Nguyen, and T. Dhaene, "Adaptive sampling algorithm for macromodeling of parameterized S-parameter responses," *IEEE Trans. Microw. Theory Tech.*, vol. 59, no. 1, pp. 39–45, Jan 2011.

[22] D. Deschrijver, T. Dhaene, and D. De Zutter, "Robust parametric macromodeling using multivariate orthonormal vector fitting," *IEEE Trans. Microw. Theory Tech.*, vol. 56, no. 7, pp. 1661–1667, July 2008.

[23] F. Ferranti, "Parameterized macromodeling and model order reduction of high-speed interconnects," Ph.D. dissertation, Ghent University, Gent, Belgium, 2011.

[24] E. R. Samuel, "Parameterized modeling and model order reduction for large electrical systems," Ph.D. dissertation, Ghent University, Ghent, Belgium, 2015.

[25] P. Triverio, "Self consistent, efficient and parametric macromodels for high-speed interconnects design," Ph.D. dissertation, Politecnico di Torino, Turin, Italy, 2009.

[26] G. Antonini, D. Deschrijver, and T. Dhaene, "Broadband rational macromodeling based on the adaptive frequency sampling algorithm and the partial element equivalent circuit method," *IEEE Trans. Electromagn. Compat.*, vol. 50, no. 1, pp. 128–137, Feb 2008.

[27] T. Dhaene, J. Ureel, N. Fache, and D. De Zutter, "Adaptive frequency sampling algorithm for fast and accurate S-parameter modeling of general planar structures," in *IEEE MTT-S Int. Microw. Symp. Dig.*, vol. 3, May 1995, pp. 1427–1430.

[28] R. Lehmensiek and P. Meyer, "An efficient adaptive frequency sampling algorithm for model-based parameter estimation as applied to aggressive space mapping," *Microw. Optical tech. lett.*, vol. 24, no. 1, pp. 71–78, 2000.

[29] ——, "Creating accurate multivariate rational interpolation models of microwave circuits by using efficient adaptive sampling to minimize the number of computational electromagnetic analyses," *IEEE Trans. Microw. Theory Tech.*, vol. 49, no. 8, pp. 1419–1430, Aug 2001.

[30] N. Mutonkole and D. I. L. de Villiers, "Characteristic basis function patterns method for reflector antenna calibration: An extension to multiple frequencies," in *9th Eur. Conf. Antennas Propag. (EuCAP)*, Lisbon, Portugal, Apr. 2015.

[31] N. Mutonkole, E. R. Samuel, D. I. L. de Villiers, and T. Dhaene, "Parametric modeling of radiation patterns and scattering parameters of antennas," *IEEE Trans. Antennas Propag.*, vol. 64, no. 3, pp. 1023–1031, Mar 2016.

[32] N. Mutonkole and D. I. L. de Villiers, "An adaptive sampling algorithm for the efficient prediction of antenna radiation patterns over a wide frequency bandwidth," in *10th Eur. Conf. Antennas Propag. (EuCAP)*, Davos, Switzerland, Apr. 2016.

[33] ——, "Multivariate adaptive sampling of parameterized antenna responses," *IEEE Trans. Antennas Propag.*, July 2016, submitted.

[34] O. M. Smirnov, "Revisiting the radio interferometer measurement equation. II. Calibration and direction-dependent effects," *Astron. Astrophys.*, vol. 527, p. A107, 2011.

[35] G. Harp *et al.*, "Primary beam and dish surface characterization at the allen telescope array by radio holography," *IEEE Trans. Antennas Propag.*, vol. 59, no. 6, pp. 2004–2021, June 2011.

[36] K. Crombecq, D. Gorissen, D. Deschrijver, and T. Dhaene, "A novel hybrid sequential design strategy for global surrogate modeling of computer experiments," *SIAM J. Sci. Comput.*, vol. 33, no. 4, pp. 1948–1974, 2011.

[37] L. L. Scharf, *The SVD and Reduced Rank Signal Processing*, ser. SVD and Signal Processing II: Algorithms, Analysis and Applications, R. J. Vaccaro, Ed. Elsevier science, 1991.

[38] N. Mutonkole and D. I. L. de Villiers, "A 3:1 bandwidth planar, lossless cavity backed sinuous antenna for reflector feed applications," in *IEEE AFRICON, Mauritius*, Sept 2013, pp. 222–226.

[39] I. Theron, R. Lehmensiek, and D. I. L. de Villiers, "Towards an optics design for the SKA," in *IEEE AFRICON, Mauritius*, 2013, pp. 1313–1317.

[40] A. Young, M. Terada, D. I. L. De Villiers, and D. Davidson, "Assessment of the sensitivity of the South African KAT-7 and MeerKAT/SKA radio telescope reflector antennas," in *Int. Conf. Electromagn. Adv. Appl. (ICEAA)*, Sept 2012, pp. 486–489.

[41] E. J. Candes and M. B. Wakin, "An introduction to compressive sampling," *IEEE Signal Process. Mag.*, vol. 25, no. 2, pp. 21–30, March 2008.

[42] MATLAB R2009A User's Guide. [Online]. Available: www.mathworks.com

[43] I. Couckuyt, F. Declercq, T. Dhaene, H. Rogier, and L. Knockaert, "Surrogate-based infill optimization applied to electromagnetic problems," *Int. J. RF Microw. Comput.-Aided Eng.*, vol. 20, no. 5, pp. 492–501, 2010. [Online]. Available: http://dx.doi.org/10.1002/mmce.20455

[44] S. Koziel, S. Ogurtsov, I. Couckuyt, and T. Dhaene, "Variable-fidelity electromagnetic simulations and co-Kriging for accurate modeling of antennas," *IEEE Trans. Antennas Propag.*, vol. 61, no. 3, pp. 1301–1308, March 2013.

[45] D. Gorissen, "Grid-enabled adaptive surrogate modeling for computer aided engineering," Ph.D. dissertation, Ghent University, Ghent, Belgium, 2010.

[46] F. Ferranti, T. Dhaene, L. Knockaert, G. Antonini, and A. Ciccomancini Scogna, "Scalable compact models for fast design optimization of complex electromagnetic systems," *Int. J. RF Microw. Comput.-Aided Eng., SPECIAL ISSUE on EM-CAD Models and their Integration into Industry-Standard CAD Tools*, vol. 22, no. 1, pp. 20–29, Jan. 2012.

[47] F. Ferranti, L. Knockaert, and T. Dhaene, "Passivity-preserving parametric macromodeling by means of scaled and shifted state-space systems," *IEEE Trans. Microw. Theory Tech.*, vol. 59, no. 10, pp. 2394–2403, Oct 2011.

[48] E. R. Samuel, L. Knockaert, F. Ferranti, and T. Dhaene, "Guaranteed passive parameterized macromodeling by using sylvester state-space realizations," *IEEE Trans. Microw. Theory Tech.*, vol. 61, no. 4, pp. 1444–1454, Apr. 2013.

[49] P. Triverio, S. Grivet-Talocia, and M. Nakhla, "A parameterized macromodeling strategy with uniform stability test," *IEEE Trans. Adv. Packag.*, vol. 32, no. 1, pp. 205–215, Feb 2009.

[50] B. Gustavsen and A. Semlyen, "Rational approximation of frequency domain responses by vector fitting," *IEEE Trans. Power Del.*, vol. 14, no. 3, pp. 1052–1061, Jul 1999.

[51] E. G. Gilbert, "Controllability and observability in multi-variable control systems," *SIAM J. Control*, vol. 1, no. 2, pp. 128 – 151, 1963.

[52] FEKO version 7.0. Altair HyperWorks. Stellenbosch, South Africa, 2015. [Online]. Available: www.feko.info

[53] CST Microwave Studio ver. 2016. Computer Simulation Technology. Darmstadt, Germany, 2016. [Online]. Available: www.cst.com

[54] GRASP version 10.4.0. TICRA. Copenhagen, Denmark, 2015. [Online]. Available: www.ticra.com

[55] J. De Geest, T. Dhaene, N. Fache, and D. De Zutter, "Adaptive CAD-model building algorithm for general planar microwave structures," *IEEE Trans. Microw. Theory Tech.*, vol. 47, no. 9, pp. 1801–1809, Sep 1999.

[56] J. P. C. Kleijnen, *Design and analysis of simulation experiments.* New York: Springer, 2008.

[57] DACE: A MATLAB Kriging Toolbox. [Online]. Available: http://www2.imm.dtu.dk/~hbni/dace/

[58] N. Mutonkole, "Study of a wideband sinuous feed for reflector antenna applications," Master's thesis, University of Stellenbosch, Stellenbosch, South Africa, 2013.

[59] P. Takook, "Fast analysis of gap waveguides using the characteristic basis function method and advanced green's function approaches," Master's thesis, Chalmers University of Technology, Gothenburg, Sweden, 2012.

[60] D. Deschrijver and T. Dhaene, "Univariate rational macromodeling of high-speed passive components: a comparative study," *ACES Newsletter*, vol. 20, no. 2, pp. 35–60, July 2005.

[61] R. H. DuHamel, "Dual polarized sinuous antennas," U.S. Patent 4 658 262, April, 1987.

[62] D. Deschrijver, F. Vanhee, D. Pissoort, and T. Dhaene, "Automated near-field scanning algorithm for the EMC analysis of electronic devices," *IEEE Trans. Electromagn. Compat.*, vol. 54, no. 3, pp. 502–510, June 2012.

[63] F. Aurenhammer, "Voronoi diagrams – a survey of a fundamental geometric data structure," *ACM Comput. Surveys*, vol. 23, no. 3, pp. 345–405, 1991.

[64] K. Crombecq, "Surrogate modelling of computer experiments with sequential experimental design," Ph.D. dissertation, University of Antwerp, Antwerp, Belgium, 2012.

[65] S. Ulaganathan, I. Couckuyt, F. Ferranti, T. Dhaene, and E. Laermans, "Variable-fidelity surrogate modelling with kriging," in *Proc. 17th Int. Conf. Chemistry and Chemical Eng.*, Amsterdam, The Netherlands, 2015, pp. 514–518.

[66] P.-S. Kildal, "Factorization of the feed efficiency of paraboloids and cassegrain antennas," *IEEE Antennas Propag. Mag.*, vol. AP-33, no. 8, pp. 903–908, August 1985.

[67] D. R. Jones, M. Schonlau, and W. Welch, "Efficient global optimisation of expensive black-box functions," *J. Global Optim.*, vol. 13, pp. 455–492, 1998.